Available online at www.sciencedirect.com
ScienceDirect
Comput. Methods Appl. Mech. Engrg. 412 (2023) 116102
Computer methods in applied mechanics and engineering
www.elsevier.com/locate/cma

Review

Past, current and future trends and challenges in non-deterministic fracture mechanics: A review

Yuan Feng[a,b], Di Wu[c], Mark G. Stewart[c], Wei Gao[a,*]

[a] *Centre for Infrastructure Engineering and Safety (CIES), School of Civil and Environmental Engineering, The University of New South Wales, Sydney, NSW 2052, Australia*

[b] *School of Architecture and Built Environment, University of Newcastle, Callaghan, NSW 2308, Australia*

[c] *Centre for Built Infrastructure Research (CBIR), School of Civil and Environmental Engineering, University of Technology Sydney, Ultimo, NSW 2007, Australia*

Received 19 February 2023; received in revised form 18 April 2023; accepted 28 April 2023
Available online 18 May 2023

Abstract

Structural systems are consistently encountering the variabilities in material properties, undesirable defects and loading environments, which may potentially shorten their designed service life. To ensure a reliable structural performance, it is vital to track and quantify the effects of different random/uncertainty factors upon the structural fracture performance. In this research, a critical review of the past, current and future computational modelling of the non-deterministic fracture mechanics is presented. By considering the variously numerical solutions tackling the fracture problems, they are mainly categorized into the discrete and continuous approaches. This study discusses the quantification performance of the extended finite element method, the crack band method and the phase-field approaches combined with different sources of uncertainties. These well-known computational techniques are typical representatives of the common fracture modelling philosophies including the embedded, smeared and regularized ones. The essence of this work is to compare the main differences of the uncertainty quantification models (i.e., probabilistic, non-probabilistic) at the fracture formulation levels and investigate the major progress and challenges existing in the real-life applications for the past and future decades. Some critical remarks, which are denoting the advantages and major issues of various non-deterministic fracture models, are provided and explained in the practical structural failure conditions. Different fracture simulation cases are implemented with comparative results amongst analytical, numerical and experimental methods, and the corresponding fracture quantification ability is evaluated through the standards of the random fracture capacity, load–deflection plots, crack propagation, crack mechanisms, and computational efficiency, etc.

Keywords: Comparative review; Stochastic fracture mechanics; Non-stochastic fracture mechanics; Uncertainty quantification; Machine learning; Non-deterministic crack growth

Contents

* Corresponding author.
E-mail address: w.gao@unsw.edu.au (W. Gao).

https://doi.org/10.1016/j.cma.2023.116102

1. Introduction

Fracture mechanisms have been a long-term physical challenge existing widely in aerospace, civil, mechanical, marine, and construction fields, for instance the large-scale concrete infrastructures, offshore platforms, and aviation engine turbines. These engineering components and systems are often vulnerable to visible and invisible crack growth due to the different working conditions and environmental factors, which results in a critical loss on the overall bearing capacity of the structural system. Consequently, it is very important to analyse the performance of engineering structures under fracture loading. Moreover, uncertainties in a structural system are common which are caused by the variability in external loading, material properties, undesirable defects, degradation in material property, as well as other uncontrolled issues existing within the complicated construction or manufacturing period. There is no doubt that the uncertainties involved in the fracture performance of engineering structures would be varied with the different remaining capacities. Thus, a critical review of the random input-sources in the fracture mechanism framework is provided in this research. In the initial structural design stage, the series of randomness are handled with the safety factors under different scenarios. However, due to the complex conditions involved

in the practical applications, the primary safety factor method is often found to be insufficient to manage the various types of uncertainties in material and geometric parameters, especially for structures prone to fracture failure modes. To deal with this issue, subsequent probabilistic and non-probabilistic theories are incorporated into fracture mechanics to obtain a detailed description of different types of input uncertainty parameters and provide referable simulated information for experimental observations, as a large number of repetitive experimental tests addressing the uncertainties are normally unaffordable even for a simple structural member.

In the past several decades, much research has been implemented within the context of the deterministic fracture mechanics. The prevailing numerical frameworks can be categorized as discrete and continuous ones. Meanwhile, the three crack simulation methods, namely the extended finite element method (XFEM), the crack band method and phase-field approaches, have been widely developed. These renown computational techniques represent three common fracture modelling philosophies: embedded, smeared and regularized. Whilst Belytschko et al. [1,2] proposed a minimal remeshing technique, namely the extended finite element method to simulate elastic crack growth, Miehe et al. [3,4] utilized the variational function framework and thermo-mechanical principle to conduct the phase field analysis for brittle and quasi-brittle fracture. Parts of some popular approaches for simulating crack growth include: the multi-scale fracture simulation [5–8], the generalized finite element method [9,10], the meshfree method [11,12] the extended meshless approach [13,14], the scaled boundary finite element method [15,16], the particle method [17,18], and the extended isogeometric analysis method [19,20]. For some popular discrete approaches, the cohesive element method [21,22] and the peridynamics method [23,24] are used. For the quasi-brittle structural failure, the above mentioned approaches can be combined with a cohesive zone model. Recently, Wu et al. [25,26] implemented the cohesive zone model into the phase field as a regularized cohesive zone method to simulate the nonlinear performance of the brittle or quasi-brittle fracture in various structures. A comprehensive review of the XFEM, mixed FEM and phase field methods towards brittle and quasi-brittle cracking can be found in [27]. Another critical mechanism which has drawn extensive attention is the fatigue induced crack growth problem [28,29]. The fatigue crack growth can be important to the fracture tolerance evaluation and the judgement of detection stage, which will make sure the fatigue cracks in the structural component would not develop to collapse within or prior to the designed working lifetime [30].

Despite the vast research developed on the deterministic fracture analysis of engineering structures, there are limited studies that can assess the influence of uncertainties within the system [31,32]. Considering the complicated manufacturing process, the accurate specification and the design of engineering products are not achievable. Moreover, the random effect of the external loading is inevitable which may cause significant fluctuation in the structural responses, such as the uncertain analysis for the fatigue crack growth in engineering components [33,34]. Some early research works have combined the conventional discrete and smeared crack models with different uncertainty quantification methods [33,35–37], however, the issues of large-mesh refinement and shear locking effect were noticed [38,39]. Although the XFEM can avoid the problem of mesh refinement, the random crack growth paths [40,41], especially for three-dimensional cracked structures, are still numerically infeasible to achieve without the prescribed cracking directions [42].

Probabilistic theory-based methods [37,43–50], and non-probabilistic theory-based methods [51–62], have been developed for physical crack simulation methods. These studies [27,33–52] described the uncertainties into probabilistic formulation level, and some tried to use fuzzy or interval boxes to represent the possible crack regions within the structure. However, some limitations are still present. The probabilistic methods can be performed when the probabilistic feature (e.g., probability density functions) or statistical information (e.g., means and standard deviations) of random parameters are available or inferred, sometimes from limited data [63,64]. The non-probabilistic methods can supplement the insufficient distributions of random parameters, but the deviation level must be rigorously selected. Furthermore, the issue of high computational cost of both approaches remains. In recent years, an alternative way to solve this problem is to construct a machine learning model based on the representation of the original FE high-fidelity model [65]. Among the popular machine learning algorithms, the Gaussian process or Kriging [66,67], the neural network [68,69], the support vector regression [70,71], the reinforcement learning [72], and the response surface [73,74], have been frequently used in various complicated mechanical fields, including the fracture mechanism [75–79]. As such, a comparative review of various uncertainty quantification approaches for fracture mechanisms modelling is desirable in the discipline of engineering failure analysis.

The objectives of this review are:

(1) To identify the major challenges of the numerical modelling of random cracking and how these issues can be solved effectively.

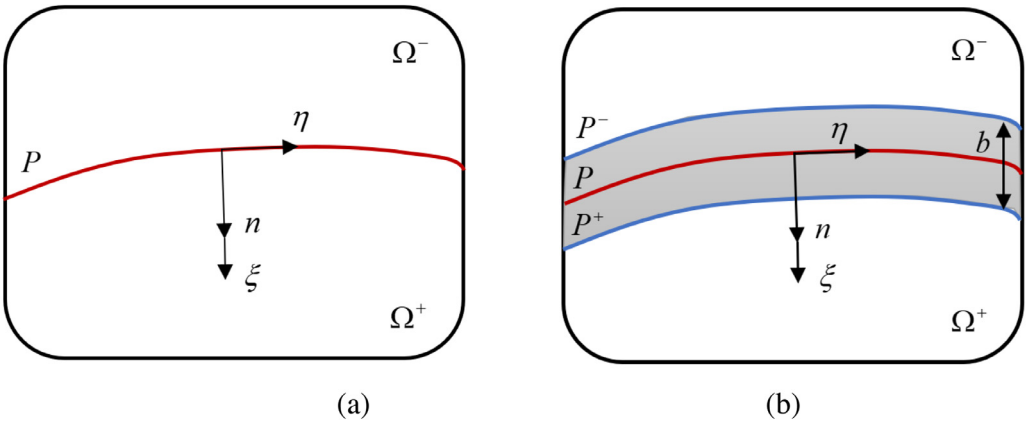

Fig. 1. Crack representations of (a) sharp and (b) continuous models.

(2) To compare the strength and weakness in the theoretical aspect and numerical approximation of the three major fracture modelling philosophies: embedded, smeared and regularized.

(3) To reveal the applicability and limitations of the probabilistic and non-probabilistic theories involved in random crack simulation methods.

(4) To demonstrate the future trends of machine learning aided non-deterministic fracture analysis that improves the random crack modelling efficiency in brittle and quasi-brittle fracture analysis.

(5) To compare the corresponding performance of some well-known uncertainty quantification methods for damaged structures.

This review is composed of seven sections. Section 2 summarizes the comparative review of the extended finite element method (XFEM), the crack band method and phase-field approach, which are known as the typical representatives of three common fracture modelling philosophies: embedded, smeared and regularized. Section 3 describes the two major categories of uncertainty quantification methods: probabilistic theory-based, and non-probabilistic theory-based methods. In Section 4, the current existing challenges of random crack modelling problems are introduced. Section 5 provides the recently developed non-deterministic fracture assessment with various machine learning algorithms used. The numerical investigation and discussion are presented in Section 6, including the deterministic, probabilistic, non-probabilistic and machine learning aided fracture analysis cases. Finally, in Section 7, both the conclusion and remarks are summarized.

2. Review of the embedded, smeared and regularized fracture modelling

Since the development of the finite element method (FEM), the modelling of cracks in different structures by using FEM have been very popular in several engineering disciplines. Many classical and valuable numerical techniques have been established. In this section, three typical crack models, i.e., embedded, smeared and regularized models, are introduced along with the FE implementations.

2.1. Embedded crack model

For a finite element discretized body Ω with discrete boundary P, the crack model can be represented as shown in Fig. 1. The crack within the body can be modelled as either the sharp or the continuous methods, and the corresponding deflection and strain fields are shown in Fig. 2, respectively.

Observed from Fig. 1, the embedded crack model represents a sharp crack field for the body. The crack through the finite elements is described through the embedded model that is generated with the deflection and strain curves as in Fig. 2(a). The deflection behaviour described is discontinuous along the strain field, from which a singularity is initiated at the crack line. These plots represent the basic philosophy of the embedded model or known as the Strong Discontinuity methods based on the classical computational fracture mechanics [80–86]. Among which, the extended finite element method (XFEM) is a representative of the embedded finite element model.

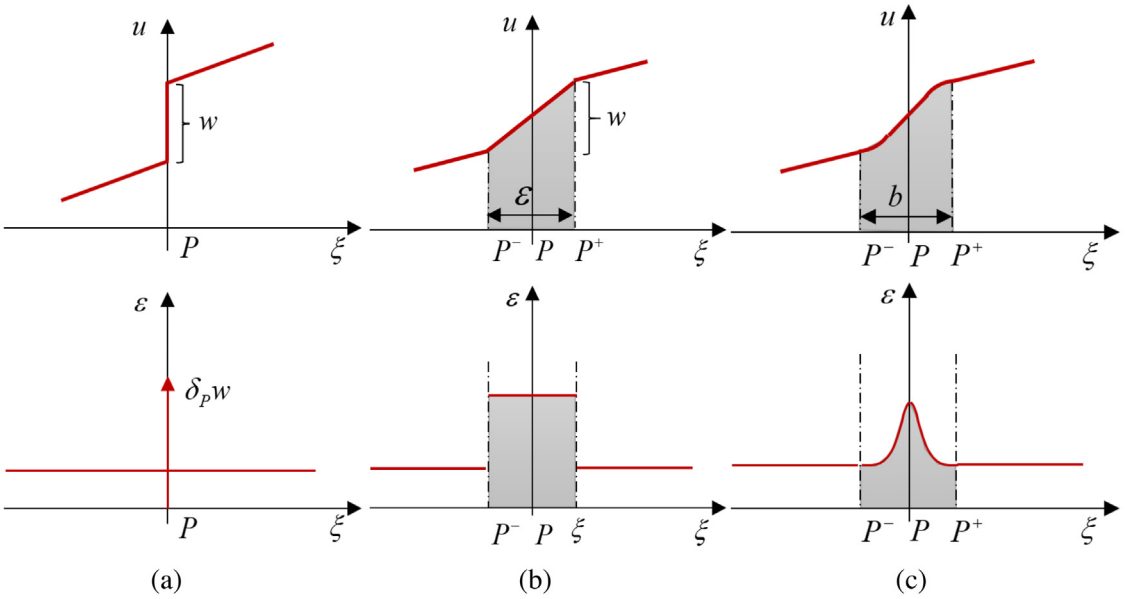

Fig. 2. Crack representations of (a) embedded, (b) smeared and (c) regularized models in the deflection and strain fields.

2.1.1. Extended finite element method (XFEM)

The extended finite element method (XFEM) is one of the classical fracture simulation techniques to simulate an embedded sharp crack within the solid body. An additional degree of freedom and the interpolation formulation are defined to describe the crack discontinuity. By using the XFEM, the complicated remeshing procedure can be omitted, which saves computational efforts.

The XFEM was proposed by Belytschko et al. [1,87] to solve the discontinuity fracture problems in the FE displacement field and it was originated from the generalized finite element method introduced by Babuska et al. [88,89]. Before the development of XFEM, fracture propagation was simulated mainly relying on the remeshing techniques and cohesive elements inclusion [90–95]. However, the mesh dependency issues generated from these approaches were affecting the crack simulation results. The embedded finite element method (EFEM) was developed to overcome these issues and an extra discontinuous displacement field was added to approximate the crack [96–98], which also constructed the basic philosophy of XFEM. For a comprehensive comparison between the two approaches, interested readers can find more details in [99].

As an example of the implementation of the embedded model, the XFEM requires a crack tracking technique to certify the crack orientation within the elemental level [100–102]. It should be noticed that an appropriate crack tracking technique is essential, otherwise non-stable results might be generated, which is considered as one of the major limitations for XFEM. Thus, an extended XFEM technique was developed by Wu et al. [103] through the adoption of strong discontinuity formulation tools [104].

2.1.2. Finite element equilibrium equations

For the finite elements discretized structural body, both coarse and fine meshed regions are adopted for normal and crack fields. Such that the displacement $\mathbf{u}$ of the domain point can be represented as

$$\mathbf{u} \cong \widetilde{\mathbf{u}} = \mathbf{N}_u \mathbf{U} + \widetilde{\mathbf{N}}_u \widetilde{\mathbf{U}} \tag{1}$$

where $\mathbf{U}$ and $\widetilde{\mathbf{U}}$ denotes the displacements of the coarse and fine mesh fields, respectively. $\mathbf{N}_u$ and $\widetilde{\mathbf{N}}_u$ are the interpolation or shape functions for the elemental matrix. Generally, the coarse mesh is throughout the body domain and the fine mesh is added into the discontinuous cracks. $\widetilde{\mathbf{U}}$ and $\widetilde{\mathbf{N}}_u$ are enriched displacements and functions to simulate the crack deflection jump, with the formulations of

$$\widetilde{\mathbf{N}}_{u,n}(\mathbf{x}) = \mathbf{N}_{u,n}(\mathbf{x})\theta_n(\mathbf{x}) \tag{2}$$

$$\theta_n(\mathbf{x}) = H_S(\mathbf{x}) - H_S(\mathbf{x}_n) \tag{3}$$

where $H_S(\mathbf{x})$ denotes the Heaviside function with settings of $H_S(\mathbf{x}) = 1$, when $(\mathbf{x} - \mathbf{x}_S) \cdot \mathbf{n}_s > 0$ or $H_S(\mathbf{x}) = 0$ otherwise [105]. The detailed construction process of the enriched functions to represent crack can be found in Fig. 3. For the modified is-XFEM, an extra term was added into the Heaviside function to provide stability as

$$\theta_n(\mathbf{x}) = H_S(\mathbf{x}) - c_s\varphi(\mathbf{x}) - (1 - c_s)H_S(\mathbf{x}_n) \tag{4}$$

where

$$\varphi(\mathbf{x}) = \sum_{n\in A^*} \mathbf{N}_n(\mathbf{x})H_S(\mathbf{x}_n) \tag{5}$$

Based on the displacement function, the strain of the crack body is derived as

$$\boldsymbol{\varepsilon} \cong \widetilde{\boldsymbol{\varepsilon}} = \mathbf{B}_u\mathbf{U} + \widetilde{\mathbf{B}}_u\widetilde{\mathbf{U}} \tag{6}$$

where $\mathbf{B}_u$ and $\widetilde{\mathbf{B}}_u$ are the displacement-strain matrix for the normal and enriched fields, respectively. Subsequently, the weak form for finite element equilibrium functions are summarized for the structural system as

$$\int_{\Omega\setminus S} \mathbf{B}_u^T\boldsymbol{\sigma}\, d\Omega = \int_{\Omega} \mathbf{N}_u^T\mathbf{f} d\Omega + \int_{\Gamma_t} \mathbf{N}_u^T\bar{\mathbf{t}} d\Gamma \tag{7}$$

$$\int_{\Omega\setminus S} \widetilde{\mathbf{B}}_u^T\boldsymbol{\sigma}\, d\Omega + \int_{S} \mathbf{N}_u^T\mathbf{t} dS = \int_{\Omega} \widetilde{\mathbf{N}}_u^T\mathbf{f} d\Omega + \int_{\Gamma_t} \widetilde{\mathbf{N}}_u^T\bar{\mathbf{t}} d\Gamma \tag{8}$$

which can be further transformed as

$$\int_{\Omega\setminus S} \mathbf{B}_u^T\mathbf{D}\mathbf{B}_u\mathbf{U} d\Omega + \int_{\Omega\setminus S} \mathbf{B}_u^T\mathbf{D}\widetilde{\mathbf{B}}_u\widetilde{\mathbf{U}} d\Omega = \int_{\Omega} \mathbf{N}_u^T\mathbf{f} d\Omega + \int_{\Gamma_t} \mathbf{N}_u^T\bar{\mathbf{t}} d\Gamma \tag{9}$$

$$\int_{\Omega\setminus S} \widetilde{\mathbf{B}}_u^T\mathbf{D}\mathbf{B}_u\mathbf{U} d\Omega + \int_{\Omega\setminus S} \widetilde{\mathbf{B}}_u^T\mathbf{D}\widetilde{\mathbf{B}}_u^T\widetilde{\mathbf{U}} d\Omega + \int_{S} \mathbf{N}_u^T\mathbf{E}_S\mathbf{N}_u\widetilde{\mathbf{U}} dS = \int_{\Omega} \widetilde{\mathbf{N}}_u^T\mathbf{f} d\Omega + \int_{\Gamma_t} \widetilde{\mathbf{N}}_u^T\bar{\mathbf{t}} d\Gamma \tag{10}$$

A simplified version of the FE equilibrium can be expressed as

$$\begin{bmatrix} \mathbf{K}_{\mathbf{UU}} & \mathbf{K}_{\mathbf{U}\widetilde{\mathbf{U}}} \\ \mathbf{K}_{\widetilde{\mathbf{U}}\mathbf{U}} & \mathbf{K}_{\widetilde{\mathbf{U}}\widetilde{\mathbf{U}}} \end{bmatrix} \begin{bmatrix} \mathbf{U} \\ \widetilde{\mathbf{U}} \end{bmatrix} = \begin{bmatrix} \mathbf{F} \\ \widetilde{\mathbf{F}} \end{bmatrix} \tag{11}$$

where

$$\begin{cases} \mathbf{K}_{\mathbf{UU}} = \displaystyle\int_{\Omega\setminus S} \mathbf{B}_u^T\mathbf{D}\mathbf{B}_u d\Omega \\ \mathbf{K}_{\mathbf{U}\widetilde{\mathbf{U}}} = \displaystyle\int_{\Omega\setminus S} \mathbf{B}_u^T\mathbf{D}\widetilde{\mathbf{B}}_u d\Omega \\ \mathbf{K}_{\widetilde{\mathbf{U}}\mathbf{U}} = \displaystyle\int_{\Omega\setminus S} \widetilde{\mathbf{B}}_u^T\mathbf{D}\mathbf{B}_u d\Omega \\ \mathbf{K}_{\widetilde{\mathbf{U}}\widetilde{\mathbf{U}}} = \displaystyle\int_{\Omega\setminus S} \widetilde{\mathbf{B}}_u^T\mathbf{D}\widetilde{\mathbf{B}}_u^T d\Omega + \int_{S} \mathbf{N}_u^T\mathbf{E}_S\mathbf{N}_u dS \\ \mathbf{F} = \displaystyle\int_{\Omega} \mathbf{N}_u^T\mathbf{f} d\Omega + \int_{\Gamma_t} \mathbf{N}_u^T\bar{\mathbf{t}} d\Gamma \\ \widetilde{\mathbf{F}} = \displaystyle\int_{\Omega} \widetilde{\mathbf{N}}_u^T\mathbf{f} d\Omega + \int_{\Gamma_t} \widetilde{\mathbf{N}}_u^T\bar{\mathbf{t}} d\Gamma \end{cases} \tag{12}$$

It should be noticed that in the modified XFEM technique, an average of elemental stress distribution is used to judge the crack propagation instead of the local stress value

$$\overline{\boldsymbol{\sigma}}_e = \frac{1}{V_e}\int_{\Omega_e} \boldsymbol{\sigma}\, d\Omega \tag{13}$$

where V_e denotes the elemental volume of a domain Ω_e. By using the Rankine standard, XFEM considers a crack would continue to propagate if the maximum principal of $\overline{\boldsymbol{\sigma}}_e$ is larger than the material strength, and a nonlocal

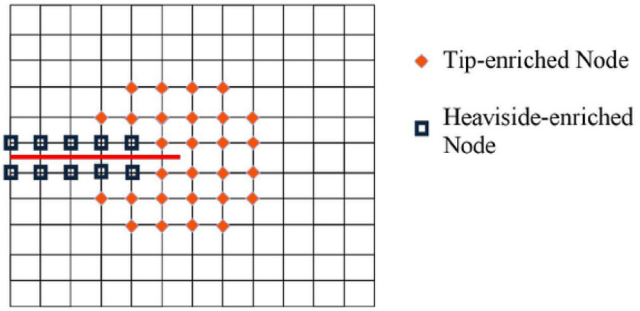

Fig. 3. Diagram of enriched elements and nodes.

stress state is implemented to further calculate the direction of the crack propagation through

$$\widetilde{\boldsymbol{\sigma}}_e = \int_{\Omega_e} \varphi_0(r)\boldsymbol{\sigma}\, d\Omega \approx \sum_{e=1}^{n_{Ve}} \varphi_0(r_e) V_e \overline{\boldsymbol{\sigma}}_e, \;\; \varphi_0(r_e) = \exp(-\frac{r_e^2}{r_0^2}) \tag{14}$$

where φ_0 denotes a weighting function; r_e denotes the elemental distance, normally with $r_e \leq 2.5r_0$. Besides, other types of criteria can be adopted to analyse the state and the direction of the crack propagation for the XFEM technique [106–108]. However, the actual performance of the crack tracking methods needs to be tested for practical fracture simulations.

2.1.3. Remarks

The XFEM embedded crack model exhibits strong advantages in fracture simulation ever since its generation, however with more complicated physical reality issues required, the method has rarely been extended due to its intrinsic limitations. In this section, several remarks about the advantages and disadvantages of the XFEM technique are discussed.

Remark 1. The most important ability of the XFEM technique compared with the classical fracture mechanics is that it could explicitly model the sharp crack with no implementation of remeshing process. Due to the generality of the embedded crack model, different softening laws can be adopted to simulate both brittle and quasi-brittle behaviours of structures. Normally, the enriched nodes and elements are added only as the crack field, which will not lead to a significant increase of total degree of freedoms for FE approximation. Hence, a relatively small number of computational efforts are required for the XFEM technique.

Remark 2. The development of the XFEM has been restricted to several inherent issues in recent decades. First, the successful calculation of the XFEM crack growth requires a prior knowledge of the position and direction of the potential crack, which means a well-chosen criterion is needed for the proper simulation of the crack propagation. Since an enriched displacement field is added to construct the discontinuous crack field, an appropriate elemental interpolation scheme is required to provide accurate approximation of the fracture response within the FE region. Moreover, when it comes to the interpolation scheme with a three-dimensional problem, the implementation difficulty can be significantly magnified. Also, when considering the subsequent crack-tracking ability in a spatial field, the complexity to construct the continuous crack is not simple. In practical fracture terms, multiple and branching cracks are common to observe, however, the XFEM cannot always guarantee stable and promising results against such situations.

2.2. Smeared crack model

For a finite element discretized body Ω with discrete boundary P, the smeared crack model can be represented as shown in Fig. 2(b). Different from the embedded element, the fracture behaviour is smeared through the entire element with a bandwidth b, which should be determined based on the mesh size. Also, the displacement field is

continuous and strain field is related to the adopted bandwidth. The concept of the smeared method was initially proposed by Rashid et al. [109] to investigate the strength of prestressed concrete vessels. Soon after, it was widely used in different FE approximations. Later, a crack band model was developed by Bazant et al. [110] to incorporate the smeared approach into the classical Griffith's fracture mechanism, by using the bandwidth parameter along with the material fracture properties to decide the brittle behaviour of the finite elements. That is, the crack representation of the structure largely depends on the mesh size selected, and to some extent, the smeared crack model could converge to the embedded sharp crack [110–112].

To increase the precision and independence for the smeared crack band method, an extended crack band model was developed at FE level [113,114], from which the strain field was independent from the elemental size and obtained by using the interpolation function from the displacement field. This improvement increased the convergence rate and the fracture modelling accuracy in both displacement and strain fields, and. the mesh dependency issue has been greatly resolved. In the modified smeared crack band model, the crack bandwidth was adapted to two times of the elemental size for better description. A brief introduction of this model will be presented in the following section.

2.2.1. Crack band model

The crack band model follows the basic framework of continuum mechanics, and the criteria of crack initiation and propagation depends on the stress field at the crack tip. By using the regular FE formulation, the singularity of the stress field is not guaranteed due to the mesh dependence problem. Thus, the crack band theory increases the order of displacement and stress fields to satisfy the convergence of different responses. By using the additional interpolation functions in the FE space, the accuracy of the smeared crack approach can be stabilized, which has been adopted to solve various engineering problems [115,116].

The smeared crack or crack band model has been well developed in different strain-based and stress-based mechanisms, which considers the energy dissipation along with the mesh conditions during the crack growth process. By using the continuum damage mechanics, the crack band model smears the sharp crack through a band width of b. For instance, a one-dimensional tensile bar as shown in Fig. 4, the load–displacement relation of the bar is

$$\delta = \frac{F}{AE}L \tag{15}$$

where F, δ are the external force and deflection, A, E, L are the cross section, Young's modulus, and length of the bar, respectively. Assume σ_u is the tensile strength, when the external force reaches the strength limit, the bar would crack. For this condition, the total displacement of bar can be represented as

$$u = u_c + u_e \tag{16}$$

where u_c denotes the crack opening displacement, u_e denotes the elastic displacement. By using the fracture energy G_{IC}, the formulation can be further expressed as

$$u = 2G_{IC}/\sigma_u[1 - F/(\sigma_u A)] + F/(EA)L \tag{17}$$

The total strain is also composed of crack strain and elastic strain as

$$\varepsilon = \varepsilon_c + \varepsilon_e,\ \ \varepsilon_c = 2G_{IC}/(h\sigma_u^2)(\sigma_u - \sigma) \tag{18}$$

Based on the one-dimensional constitutive relation, a continuum two-dimensional strain can be denoted as

$$\begin{bmatrix}\varepsilon_1\\ \varepsilon_2\end{bmatrix} = \frac{1}{E}\begin{bmatrix}1 & -\nu\\ -\nu & 1\end{bmatrix}\begin{bmatrix}\sigma_1\\ \sigma_2\end{bmatrix} + \begin{bmatrix}\varepsilon_c\\ 0\end{bmatrix} \tag{19}$$

The above equation can be further written into

$$\begin{bmatrix}\varepsilon_1\\ \varepsilon_2\end{bmatrix} = \frac{1}{E}\begin{bmatrix}1/\mu & -\nu\\ -\nu & 1\end{bmatrix}\begin{bmatrix}\sigma_1\\ \sigma_2\end{bmatrix}, 1/\mu = E\varepsilon_1/[E_t(\varepsilon_f - \varepsilon_1)] \tag{20}$$

where

$$\begin{cases}1/E_t = 1/E - 2G_{IC}/(\sigma_u^2 h)\\ \varepsilon_f = 2G_{IC}/(\sigma_u h)\end{cases} \tag{21}$$

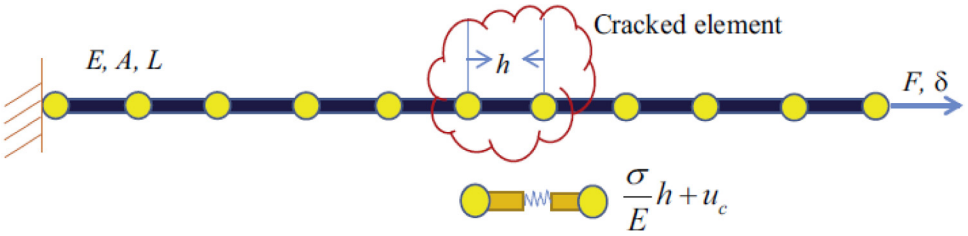

Fig. 4. The one-dimensional crack bar [117].

It should be noted that the above functions are available to mode I crack (stress orthogonal to the local plane of the crack surface) with small continuum strain. For practical mode I fracture with large strains, basing on the maximum principal stress failure criteria, the relation of the two-dimensional crack band model is expressed as

$$\begin{bmatrix} \varepsilon_{xx}-\varepsilon_f \\ \varepsilon_{yy} \\ \varepsilon_{xy} \end{bmatrix} = \begin{bmatrix} \frac{1}{E_{xx}}-\frac{2G_{IC}}{h\sigma_u^2} & \frac{-\nu_{xy}}{E_{xx}} & 0 \\ \frac{-\nu_{xy}}{E_{xx}} & \frac{1}{E_{yy}} & 0 \\ 0 & 0 & \frac{1}{G_{xy}} \end{bmatrix} \cdot \begin{bmatrix} \sigma_{xx} \\ \sigma_{yy} \\ \sigma_{xy} \end{bmatrix} \tag{22}$$

2.2.2. Remarks

The smeared approach or crack band model extends the classical Griffith's fracture theory to improve the accuracy and stability of the crack simulation against the mesh dependency and the singularity problems, and significant improvements were achieved in different conditions. However, the complexity of the constitutive formulations may be problematic, and inherent issues may be generated with FE approximation.

Remark 1. The smeared crack approach certainly contains large degree of generality by adopting the frameworks of both Griffith's and continuum fracture mechanics. This approach can be further extended to static and dynamic isotropic and orthotropic brittle or ductile crack propagation problems in two-dimensional and three-dimensional spaces [118,119]. Since the interpolation functions have been added to the displacement and strain fields, the convergence rate of the smeared approach is higher than the regular FE approximation, such that significant computational efforts can be saved during the stiffness formulation and crack calculation processes. Also, multiple and branching cracks conditions are reliable to achieve, and the judgement of the crack direction is embedded within the algorithm without any specific crack tracking techniques required. This advantage differs from the XFEM approach especially in the large-scale complicated engineering applications, such as long span concrete frame and full-scale aerospace equipment.

Remark 2. Although some advantages of the smeared approach have been reported in the literature, the practical implementation of this technique is challenging. As mentioned in the algorithm section, the interpolation and substitution of the displacement, stress and strain fields are frequently required at the elemental level, which largely increases the difficulty of incorporating the formulations into the standard finite element procedure. Thus, the effectiveness of the smeared approach is limited to certain scenarios.

2.3. Regularized crack model

The regularized crack model contains many popular sub-models, such as the phase field model, nonlocal damage model and gradient damage model by using a regular and localized bandwidth to define the sharp crack into a continuous field function [120,121], as shown in Fig. 2(c). Here, an introduction about the phase field model is illustrated.

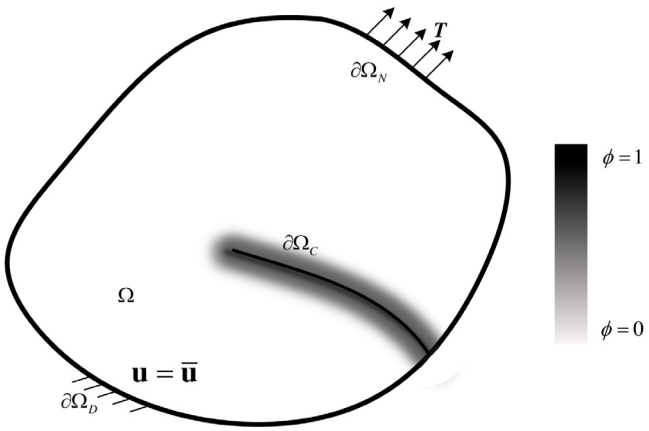

Fig. 5. Regularized crack representation for the phase field model.

2.3.1. Phase field model

Before the establishment of the phase field model, the nonlocal integral models were frequently used in the continuum fracture mechanics by involving an internal parameter to smooth the spatial domain of the FE strain field [122,123]. However, according to some Refs. [124,125], it was validated that these methods merely calculated the fracture initiation in the structural body but not at the crack tip, and a wrong crack path would be predicted with unstable performance. Also, it was found that the actual bandwidth setting within these models was not effective, so the purpose of the sharp crack regularization was not achieved [126].

To overcome these challenges, the phase field model (PFM), which is based on a diffused damage scalar field, has been developed [2,127]. The PFM continuously simulates the crack evolution of the structure from the original state to the fully cracked configuration by solving an energy-based partial differential equation (PDE). The PFM can be implemented in a wide range of applications. As the mechanics research demonstrated [128,129], the PFM is extended from the Griffith's theory [130] then later revised with the complete format [131]. Also, the thermodynamic problem has been investigated by Miehe [3,4] and relevant research works were adopted to solve the dynamic fracture and hydraulic problems [132–134]. For the multi-physics research [134,135], the multi-phase transformation technique was developed by Landau [136] to calculate the dynamic crack propagation issues as well. For the mathematics discipline, the Γ -convergence theorem was proposed [134,135] to characterize and converge the width of localization band by introducing a small length scale coefficient. Recently, a phase field regularized cohesive zone model (PF-CZM) [25,26] was proposed to simulate the both brittle and quasi-brittle fractures in an efficient Broyden–Fletcher–Goldfarb–Shanno (BFGS) solver. More explanations about the PFM can be referred for interested readers in [133].

In this section, the basic philosophy of the traditional Griffith's theory-based phase field model, which was proposed by Miehe [3,4], is briefly introduced. The linear static notched structure with discontinuity defect as $\Omega \subset \mathbb{R}^{\mathrm{d}}(\mathrm{d} = \{2, 3\})$ is shown in Fig. 5. The PFM is represented through a displacement $\mathbf{u}$, the phase field ϕ and the sharp crack is represented by a diffuse bandwidth as $\partial\Omega_C$. For a selected time stage, $\phi(x)$ at material point x ranges from 0 to 1 to define the internal damage state changes from perfect material to fully cracked.

For the damaged structure, the overall potential energy function is expressed as

$$E_{pot} = \int_{\Omega} \psi_{\varepsilon}(\varepsilon)\mathrm{d}\Omega + \int_{\partial\Omega_C} G_c(x)\mathrm{d}\partial\Omega_C - \int_{\partial\Omega_N} \mathbf{T}\cdot\mathbf{u}\mathrm{d}\partial\Omega \tag{23}$$

$\int_{\Omega} \psi_{\varepsilon}(\varepsilon)\mathrm{d}\Omega$ is the strain energy, $\int_{\partial\Omega_C} G_c(x)\mathrm{d}\partial\Omega_C$ is the fracture energy, $G_c(x)$ is the energy release rate, $\mathbf{T}$ is the external traction and $\psi_{\varepsilon}(\varepsilon)$ is the strain energy density with formulation of

$$\psi_{\varepsilon}(\varepsilon) = \frac{1}{2}\lambda(x)\langle tr\,(\varepsilon)\rangle^2 + \mu(x)tr\,(\varepsilon)^2 \tag{24}$$

where $\lambda(x)$, $\mu(x)$ denote the Lamé parameters, $\langle\cdot\rangle$ is the MaCaulay bracket, ε denotes the second-order strain tensor

$$\varepsilon = \varepsilon(\mathbf{u}) = \frac{1}{2}(\nabla\mathbf{u} + \nabla\mathbf{u}^T) \tag{25}$$

The strain energy density $\psi_\varepsilon(\varepsilon)$ is composed of the tensile strain energy density $\psi_\varepsilon(\varepsilon)^+$ and the compressive one $\psi_\varepsilon(\varepsilon)^-$. Thus, the strain energy is extended as

$$\int_\Omega \psi_\varepsilon(\varepsilon)\mathrm{d}\Omega = \int_\Omega \left[(1-\phi(x))^2 + k\right]\psi_\varepsilon(\varepsilon)^+ + \psi_\varepsilon(\varepsilon)^-\mathrm{d}\Omega \tag{26}$$

where

$$\psi_\varepsilon^\pm(\varepsilon) = \frac{1}{2}\lambda(x)\langle \mathrm{tr}(\varepsilon)\rangle_\pm^2 + \mu(x)\mathrm{tr}(\varepsilon_\pm^2) \tag{27}$$

$$\varepsilon_\pm = \sum_{i=1}^{d}\langle\varepsilon_i\rangle_\pm \mathbf{n}_i \otimes \mathbf{n}_i \tag{28}$$

where d is the dimension size, ε_i and $\mathbf{n}_i$ denote the primary strains and orientation. According to the principle of Γ-convergence [131], the fracture energy is formulated as

$$\int_{\partial\Omega_C} G_c(x)\mathrm{d}\partial\Omega_C \approx \int_\Omega G_c(x)\cdot\Gamma_{l_0}(l_0,\phi(x))\mathrm{d}\Omega \tag{29}$$

$$\Gamma_{l_0}(l_0,\phi(x)) = \frac{l_0}{2}|\nabla\phi(x)|^2 + \frac{1}{2l_0}\phi(x)^2 \tag{30}$$

where, l_0 is the length scale parameter. Thus, the total potential energy function is reformulated as

$$\begin{aligned} &E_{pot} = \delta E_{pot}^{\mathrm{int}} - \delta E_{pot}^{\mathrm{ext}} \\ &\int_\Omega \left\{\left[(1-\phi(x))^2 + k\right]\psi_\varepsilon(\varepsilon)^+ + \psi_\varepsilon(\varepsilon)^-\right\}\mathrm{d}\Omega + \int_\Omega G_c(x)\left[\frac{l_0}{2}|\nabla\phi(x)|^2 + \frac{1}{2l_0}\phi(x)^2\right]\mathrm{d}\Omega - \int_{\partial\Omega_N}\mathbf{T}\cdot\mathbf{u}\mathrm{d}\partial\Omega \end{aligned} \tag{31}$$

where $\delta E_{pot}^{\mathrm{int}}$ and $\delta E_{pot}^{\mathrm{ext}}$ are the internal and external potential energy. Since the constraint $\delta E_{pot}^{\mathrm{int}} - \delta E_{pot}^{\mathrm{ext}} = 0$ holds for both displacement and phase fields, the governing equation must yield the coupled field as

$$\begin{cases} \nabla\cdot\boldsymbol{\sigma} = 0 & \text{in } \Omega \\ -2(1-\phi(x))H(x) + \dfrac{G_c(x)\phi(x)}{l_0} + G_c(x)l_0\nabla^2\phi = 0 & \text{in } \Omega \end{cases} \tag{32}$$

which must satisfy the following

$$\begin{aligned} &\boldsymbol{\sigma}\cdot\mathbf{n} - \boldsymbol{T} = 0 \quad && \text{on } \partial\Omega_{\mathrm{N}} \\ &\nabla\phi\cdot\mathbf{n} = 0 && \text{on } \partial\Omega_{\mathrm{C}} \\ &\mathbf{u} = \overline{\mathbf{u}} && \text{on } \partial\Omega_{\mathrm{D}} \end{aligned} \tag{33}$$

where $H(x) = \max\psi_\varepsilon^+(\boldsymbol{\varepsilon}(x))$ is a strain-history field which is introduced to prevent the healing of the crack.

Subsequently, the weak form of the governing equations of the coupled field is derived by using the Bubnov–Galerkin method, from which the displacement and phase fields can be further calculated by a staggered approach

$$\begin{cases} \displaystyle\int_\Omega \left[\boldsymbol{\sigma}(\mathbf{u}(x)) : \boldsymbol{\varepsilon}(\delta\mathbf{u}(x)) - \mathbf{T}\delta\mathbf{u}(x)\right]\mathrm{d}\Omega = 0 \\ \displaystyle\int_\Omega \left[\left(\frac{G_c(x)}{l_0} + 2H(x)\right)\phi(x)\delta\phi(x) + G_c(x)l_0\nabla\phi(x)\nabla(\delta\phi(x)) - 2H(x)\delta\phi(x)\right]\mathrm{d}\Omega = 0 \end{cases} \tag{34}$$

2.3.2. Finite element equilibrium equations

In the FE approximation, the $\mathbf{u}(x)$ and $\phi(x)$ of the ith nodal point of the PFM model and their gradients are expressed by

$$\mathbf{u}(x) = \mathbf{N}_i^u(x)\mathbf{u}_i, \quad \nabla\mathbf{u}(x) = \mathbf{B}_i^u(x)\mathbf{u}_i \tag{35}$$

$$\phi(x) = \mathbf{N}_i^\phi(x)\phi_i, \quad \nabla\phi(x) = \mathbf{B}_i^\phi(x)\phi_i \tag{36}$$

where $\mathbf{N}^u, \mathbf{N}^\phi$ and $\mathbf{B}^u, \mathbf{B}^\phi$ are the shape functions and derivatives of the $\mathbf{u}(x)$ and $\phi(x)$.

By incorporating the FE equations into Eq. (34), the discretized weak form equation is transformed as

$$\begin{cases} \displaystyle\int_\Omega \left[(\mathbf{B}^u)^T\mathbf{D}\mathbf{B}^u\mathbf{u}(x) - (\mathbf{N}^u)^T\mathbf{T}\right]\mathrm{d}\Omega = 0 \\ \displaystyle\int_\Omega \left[(\mathbf{N}^\phi)^T\left(\frac{G_c(x)}{l_0} + 2H(x)\right)\mathbf{N}^\phi + (\mathbf{B}^\phi)^T G_c(x) l_0 \mathbf{B}^\phi\right]\mathrm{d}\Omega \cdot \phi(x) - \int_\Omega 2H(x)(\mathbf{N}^\phi)^T\mathrm{d}\Omega = 0 \end{cases} \tag{37}$$

where $\mathbf{D}$ is linear stiffness matrix. Furthermore, the above function is reformulated as

$$\begin{cases} \mathbf{K}^u\mathbf{u}(x) - \mathbf{F}_{ext}^u = 0 \\ \mathbf{K}^\phi\phi(x) - \mathbf{F}_{ext}^\phi = 0 \end{cases} \tag{38}$$

with

$$\begin{cases} \mathbf{K}^u = \displaystyle\int_\Omega (\mathbf{B}^u)^T\mathbf{D}\mathbf{B}^u\mathrm{d}\Omega \\ \mathbf{K}^\phi = \displaystyle\int_\Omega \left\{(\mathbf{N}^\phi)^T\left[\frac{G_c(x)}{l_0} + 2H(x)\right]\mathbf{N}^\phi + (\mathbf{B}^\phi)^T G_c(x) l_0 \mathbf{B}^\phi\right\}\mathrm{d}\Omega \\ \mathbf{F}_{ext}^u = \displaystyle\int_\Omega (\mathbf{N}^u)^T\mathbf{T}\mathrm{d}\Omega \\ \mathbf{F}_{ext}^\phi = \displaystyle\int_\Omega 2H(x)(\mathbf{N}^\phi)^T\mathrm{d}\Omega \end{cases} \tag{39}$$

where $\mathbf{K}^u$ and $\mathbf{K}^\phi$ denote the global stiffness matrix of the displacement and phase fields; $\mathbf{F}_{ext}^u$ and $\mathbf{F}_{ext}^\phi$ are the external loadings.

2.3.3. Remarks

The phase field method has shown great adaptivity in various applications and the effectiveness of the method has been evidently illustrated in many different scenarios. However, the meshing requirement is quite high, which results in significant increase of computational costs for many cases.

Remark 1. The phase field method is developed from the principle of energy equilibrium and the Griffith's fracture theory. It has shown strong adaptations to model brittle and quasi-brittle static and dynamic fracture problems in both two and three-dimensional spaces. The implementation of the PFM to FE formulations is straightforward to access and the technique has currently been involved in many commercial FE software. Without the requirement of crack tracking algorithms, the PFM can simulate dynamic branching and multiple cracks by using the embedded energy-based crack initiation and propagation strategy.

Remark 2. The generality of the phase field model for different constitutive relations still needs to be investigated [137–139], and most of the current literature focused on the brittle or quasi-brittle behaviour of damaged bodies. Physical mechanism like irreversible plasticity, fracture closure and reopening have not been widely considered for the PFM. As mentioned, another typical problem of the PFM should be the running time. As mesh refinement requirement in regularization bandwidth is extremely high for structures to acquire reliable crack prediction paths, the entire elements for the FE discretization would be exceptionally huge for practical applications. Thus, the corresponding computational efforts would increase dramatically, especially for the three-dimensional damage models.

3. Review of the multiple uncertainty quantification techniques

In realistic applications, the fluctuations or the uncertainties existing in the structural system can significantly influence the modelling precision and structural reliability [140–146]. The uncertainties are including various factors such as the manufacturing deviation, measure or dimensional deviations, material properties, and external outliers. The uncertainties can be classified into two kinds: aleatory and epistemic [147]. In general, the various uncertainties can be effectively quantified through two major methods: (1) probabilistic analysis theory, such as the MCS approach, the perturbation theory and the spectral stochastic theory; (2) non-probabilistic theory, represented by the interval theory, the fuzzy theory and convex models. For the next parts, the state of the literature for two uncertainty approaches has been illustrated.

3.1. Probabilistic analysis theory

The probabilistic analysis theory is one of the most popular uncertainty quantification methods, and the theory can be implemented under the scenarios with full profiles of uncertainty information [148–150]. For the modelling of uncertainty information, both spatially dependent (value of the field at any point in space depends on the values at neighbouring points) and independent fields (values of different points do not have correlations) are considered to describe the system structural properties and external loadings [42]. For the simulation regimes of the uncertainty, the solutions of probabilistic theory could be divided into two types: (1) the direct simulative approach and (2) the non-simulative approach. For the direct simulative approach, the Monte-Carlo simulation method is the most representative one which calculates each possible realization of structural response by using a direct sampling technique [151–154]. For the non-simulative approach, the desired uncertain structural outputs need to be acquired through established mathematical or numerical approaches [155–158]. Several typical probabilistic analysis methods including both direct simulative and non-simulative techniques are listed and introduced as follows.

3.1.1. Monte Carlo simulation method

The Monte Carlo Simulation (MCS) method is a traditional technique for implementing what-if analysis, by using which the reliability of multiple-criteria decision-making results can be tested [159,160]. Also, some conclusive remarks can be summarized to analyse the relation between the varied information and the decision outcomes. The MCS method [161–163], is a powerful computational tool of quantifying different uncertainty environments and drawing in-depth probabilistic profiles against each scenario.

In contemporary engineering applications, the MCS is used to simulate the event involving repetitive generation of uncertain input variables and calculating the performance of statistical results through population samples. Subsequently, the acquired information based on the uncertainty variables can be implemented to analyse the distribution details and computational features under various scenarios. In this research, the MCS is represented as shown in Fig. 6, with horizontal axis denotes the varied cases of system properties (e.g., the Young's modulus, the Poisson's ratio, the density) and vertical axis denotes the probabilistic density of fracture response (e.g., crack energy release rate, crack length, peak force). Normally, the simulation number of samples is large (e.g., 1000∼1000000) to provide a continuous fitting curve of the possible distribution. From the plot, the mean and variance of the distribution can be estimated to quantify the specific random scenario.

3.1.2. Spectral stochastic finite element method

To simulate and ascertain the reliability of the structure with the presence of random fields, the spectral stochastic finite element method (SSFEM) has been considered a robust computational tool over several decades [164–166]. In the SSFEM, the system properties are described through the Karhunen–Loève (K–L) expansion with mean and covariance equation to represent the constitutive relation among various structural locations [167,168]. A Polynomial Chaos expansion (PCE) function has been subsequently adopted to describe possible structural responses with a series of basis equations in nodal points. Such that the stochastic problem can be inverted into a set of deterministic functions in the form of the Galerkin approach. If the unknown responses have been calculated, the PCE can estimate the statistical and reliability profiles of the response to complete the SSFEM framework.

In detail, the spatial position is denoted as $\mathbf{x}$, the physical body is represented as V. For a random field with a random variability ω denoted as $f(\mathbf{x}, \omega)$, the expectation is shown as $\langle f(\mathbf{x}, \omega)\rangle$. When there is a random

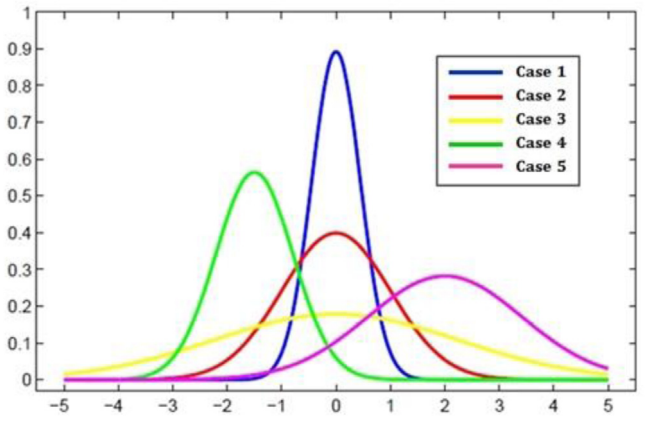

Fig. 6. Five possible realization cases of the Monte Carlo simulation-based sensitivity analysis of individual material property.

variability for the material property, the constitutive coefficients matrix is defined as $\mathbf{D}(\mathbf{x}, \omega)$ with a given mean $\overline{\mathbf{D}}(\mathbf{x}) = \langle \mathbf{D}(\mathbf{x}, \omega) \rangle$. And the autocovariance function is defined as follows

$$\mathbf{C}_{DD}(\mathbf{x}, \mathbf{x}') = \left\langle (\mathbf{D}(\mathbf{x}, \omega) - \overline{\mathbf{D}}(\mathbf{x})) \otimes (\mathbf{D}(\mathbf{x}', \omega) - \overline{\mathbf{D}}(\mathbf{x}')) \right\rangle \tag{40}$$

where $\otimes$ is the outer (tensor) product. To simplify the description, $\mathbf{D}(\mathbf{x}, \omega)$ is assumed as a form of $\mathbf{D}(\mathbf{x}, \omega) = \overline{\mathbf{D}}(\mathbf{x}) + f(\mathbf{x}, \omega)\hat{\mathbf{D}}$, for which $f(\mathbf{x}, \omega)$ is random field and $\hat{\mathbf{D}}$ is the normal matrix. Here the autocovariance equation can be described as

$$\mathbf{C}_{DD}(\mathbf{x}, \mathbf{x}') = \hat{\mathbf{D}} \otimes \hat{\mathbf{D}} R_{DD}(\mathbf{x}, \hat{\mathbf{x}}) \tag{41}$$

In which $R_{DD}(\mathbf{x}, \hat{\mathbf{x}})$ is considered as the scalar autocovariance function. The random field $\mathbf{D}(\mathbf{x}, \omega)$ can be denoted as a Karhunen–Loève Expansion (KLE) as

$$\mathbf{D}(\mathbf{x}, \omega) = \overline{\mathbf{D}}(\mathbf{x}) + \hat{\mathbf{D}} \sum_{m=1}^{\infty} \xi_m(\omega) \sqrt{\lambda_m} \Lambda_m(\mathbf{x}) \tag{42}$$

The set of λ_m and $\Lambda_m(\mathbf{x})$ are acquired from the autocovariance equation as

$$R_{DD}(\mathbf{x}, \mathbf{x}') = \sum_{m=1}^{\infty} \lambda_m \Lambda_m(\mathbf{x}) \Lambda_m(\mathbf{x}') \tag{43}$$

Through the integral eigenproblem solution of

$$\begin{aligned} &\int_V R_{DD}(\mathbf{x}, \mathbf{x}') \Lambda_m(\mathbf{x}) \mathrm{d}V(\mathbf{x}) = \lambda_m \Lambda_m(\mathbf{x}') \\ &\int_V \Lambda_m(\mathbf{x}) \Lambda_n(\mathbf{x}) \mathrm{d}V(\mathbf{x}) = \delta_{mn} \end{aligned} \tag{44}$$

The stochastic variability of $\mathbf{D}(\mathbf{x}, \omega)$ is denoted as $\hat{\mathbf{D}}$ which contains the variability degree for each component of $\mathbf{D}(\mathbf{x}, \omega)$. The infinite series can be truncated after the NKL terms to provide a manageable approximation to the random field $\mathbf{D}(\mathbf{x}, \omega)$ due to the decreasing magnitude order of the eigenvalues of λ_m and $\Lambda_m(\mathbf{x})$. The following equations can be obtained with the truncated Karhunen–Loève expansion for the system property:

$$\sum_{m=0}^{N_{KL}} \xi_m [K_m] \{u\} = \{f\} - \sum_{m=0}^{N_{KL}} \xi_m [K_m] \{\widetilde{u}\} = \sum_{m=0}^{N_{KL}} \xi_m \{f_m\} \tag{45}$$

In which $\xi_0 = 1$ is a parameter for notational convenience. $\{u\}$ and the boundary conditions of $\{f_m\} m = 0, 1, 2, \ldots, N_{KL}$ contains the unknowns, which are made up with the external loading vector $\{f\}$ and the specific structural results $\{\widetilde{u}\}$. The corresponding mathematical formulations can be summarized as

$$\begin{aligned}[K_0] &= \int_V \left\{\mathbf{g}'(\mathbf{x})\right\} \cdot \overline{\mathbf{D}}(\mathbf{x}) \cdot \left\{\mathbf{g}'(\mathbf{x})\right\}^T dV(\mathbf{x}) \\ [K_m] &= \int_V \left\{\mathbf{g}'(\mathbf{x})\right\} \cdot \hat{\mathbf{D}}(\mathbf{x}) \cdot \left\{\mathbf{g}'(\mathbf{x})\right\}^T \sqrt{\lambda_m} \Lambda_m(\mathbf{x}) dV(\mathbf{x}), m = 0, 1, 2, \ldots, N_{KL}\end{aligned} \tag{46}$$

where $\left\{\mathbf{g}'(\mathbf{x})\right\}$ is related to the shape function deriving with strain at $\mathbf{x}$ and expressed with nodal locations response. The matrix $[K_0]$ is the global stiffness matrix for material property $\overline{\mathbf{D}}(\mathbf{x})$, and matrix $[K_m] m = 1, 2, \ldots, N_{KL}$ are implemented by replacing $\sqrt{\lambda_m}\Lambda_m(\mathbf{x})$ with $\overline{\mathbf{D}}(\mathbf{x})$.

The Gaussian variable $\xi_m, m = 1, 2, \ldots, N_{KL}$ and the FE system could realize the stochastic response $\mathbf{u}(\mathbf{x}, \omega)$ computation to accumulate the statistical moments. The random field $\mathbf{u}(\mathbf{x}, \omega)$ can be considered as a Polynomial Chaos Expansion (PCE) up to polynomial order p

$$\mathbf{u}(\mathbf{x}, \omega) = \sum_{j=0}^{N_p} \Psi_j(\xi) \mathbf{v}_j(\mathbf{x}) \tag{47}$$

In Eq. (47), $\Psi_j(\xi)$, $j = 0, 1, 2, \ldots, N_p$ denotes the chaos expansions of $\boldsymbol{\xi} = \left\{\xi_1, \xi_2, \ldots \xi_{N_{KL}}\right\}$, $\mathbf{v}_j(\mathbf{x})$ denotes the dimensional equations need to be chosen. The selected terms in PCE with p in N_{KL} is

$$N_p + 1 = \frac{(p + N_{KL})!}{(p)!(N_{KL})!} \tag{48}$$

The Chaos polynomials can be defined as orthogonal with respect to the expectation as

$$\left\langle \Psi_j(\xi) \Psi_k(\xi) \right\rangle = 0 \ \text{ if } j \neq k \tag{49}$$

The first $N_{KL} + 1$ polynomials are the order 0 term $\Psi_0(\xi) = 1$ and $\Psi_j(\xi) = \xi_j (j = 1, 2, \ldots, N_{KL})$. And the nodal response vector in a finite element is:

$$\{u(\omega)\} = \sum_{j=0}^{N_p} \Psi_j(\xi) \left\{\upsilon_j\right\} \tag{50}$$

In which $\mathbf{v}_j(\mathbf{x}) = \{\mathbf{g}(\mathbf{x})\}^T \left\{\upsilon_j\right\}$ has been used by the response $\left\{\upsilon_j\right\}$ and shape functions $\mathbf{g}(\mathbf{x})$. Subsequently, the function can be expressed as:

$$\sum_{j=0}^{N_p} \sum_{m=0}^{N_{KL}} \xi_m \Psi_j(\xi) [K_m] \left\{\upsilon_j\right\} = \sum_{m=0}^{N_{KL}} \xi_m \{f_m\} \tag{51}$$

$$\sum_{j=0}^{N_p} \sum_{m=0}^{N_{KL}} c_{mjk} [K_m] \left\{\upsilon_j\right\} = \sum_{m=0}^{N_{KL}} \delta_{km} \{f_m\}, \quad k = 0, 1, 2, \ldots, N_p \tag{52}$$

where the coefficients $c_{mjk} = \left\langle \xi_m \Psi_j(\xi) \Psi_k(\xi) \right\rangle$ are integers. Due to the orthogonality properties of Eq. (49), the coefficients c_{mjk} are mostly zero. The set of Eq. (52) can be regarded as a single system where the solution vector is composed of a concatenation of the nodal vectors $\left\{\upsilon_j\right\}, j = 0, 1, 2, \ldots, N_p$, and the corresponding coefficient matrix is block-sparse. The Eq. (52) is often solved by using the Choleski decomposition of $[K_0]$. After $\left\{\upsilon_j\right\}$ is determined, the mean and autocovariance of the response can be obtained as

$$\overline{\mathbf{u}}(\mathbf{x}) = \sum_{j=0}^{N_p} \left\langle \Psi_j(\xi) \right\rangle \mathbf{v}_j(\mathbf{x}) = \mathbf{v}_0(\mathbf{x}) \tag{53}$$

$$\mathbf{C}_{\mathbf{uu}}(\mathbf{x}, \mathbf{x}') = \sum_{j=0}^{N_p} \left\langle (\Psi_j(\xi))^2 \right\rangle \mathbf{v}_j(\mathbf{x}) \otimes \mathbf{v}_j(\mathbf{x}') \tag{54}$$

where $\mathbf{v}_j(\mathbf{x}) = \{\mathbf{g}(\mathbf{x})\}^T \{\upsilon_j\}$ is the response at location $\mathbf{x}$ from the jth nodal solution vector and $\left\langle \left(\Psi_j(\xi) \right)^2 \right\rangle$. Then the strain and stress at location $\mathbf{x}$ are

$$\varepsilon(\mathbf{x}, \omega) = \sum_{j=0}^{N_p} \Psi_j(\xi) \varepsilon_j(\mathbf{x}) \tag{55}$$

$$\sigma(\mathbf{x}, \omega) = \mathbf{D}(\mathbf{x}, \omega) \cdot \varepsilon(\mathbf{x}, \omega) = \sum_{m=0}^{N_{KL}} \sum_{j=0}^{N_p} \xi_m \Psi_j(\xi) \mathbf{D}_m(\mathbf{x}) \cdot \varepsilon_j(\mathbf{x}) \tag{56}$$

where $\varepsilon_j(\mathbf{x}) = \left\{\mathbf{g}'(\mathbf{x})\right\}^T \{\upsilon_j\}$ are the strain results. The effective material coefficients can be given by $\mathbf{D}_0(\mathbf{x}) = \overline{\mathbf{D}}(\mathbf{x})$ and $\mathbf{D}_m(\mathbf{x}) = \hat{\mathbf{D}}\sqrt{\lambda_m} \Lambda_m(\mathbf{x})$ of $m = 1, 2, \ldots, N_{KL}$. To define $\sigma_{mj}(\mathbf{x}) = \mathbf{D}_m(\mathbf{x}) \cdot \varepsilon_j(\mathbf{x})$, the mean and autocovariance of the strain and stress can be obtained by

$$\overline{\varepsilon}(\mathbf{x}) = \sum_{j=0}^{N_p} \left\langle \Psi_j(\xi) \right\rangle \varepsilon_j(\mathbf{x}) = \varepsilon_0(\mathbf{x}) \tag{57}$$

$$\mathbf{C}_{\varepsilon\varepsilon}(\mathbf{x}, \mathbf{x}') = \sum_{j=0}^{N_p} \left\langle (\Psi_j(\xi))^2 \right\rangle \varepsilon_j(\mathbf{x}) \otimes \varepsilon_j(\mathbf{x}') \tag{58}$$

$$\overline{\sigma}(\mathbf{x}) = \sum_{m=0}^{N_{KL}} \sum_{j=0}^{N_p} \left\langle \xi_m \Psi_j(\xi) \right\rangle \sigma_{mj}(\mathbf{x}) = \sum_{m=0}^{N_{KL}} \sigma_{mm}(\mathbf{x}) \tag{59}$$

$$\mathbf{C}_{\sigma\sigma}(\mathbf{x}, \mathbf{x}') = \sum_{k=0}^{N_p} \sum_{j=0}^{N_p} \sum_{n=0}^{N_{KL}} \sum_{m=0}^{N_{KL}} (X_{mnjk} \sigma_{mj}(\mathbf{x})) \otimes \sigma_{nk}(\mathbf{x}') - \overline{\sigma}(\mathbf{x}) \otimes \overline{\sigma}(\mathbf{x}') \tag{60}$$

Therefore, the cumulative distribution function (CDF) and the probability density function (PDF) of the structural results, can be obtained from Eqs. (57)–(60), respectively. It needs to be noted that the SSFEM may sacrifice the accuracy of the unknown distribution types of the random responses due to the limitations in choosing the correspondingly proper polynomials.

3.1.3. Remarks

The probabilistic analysis theory has been widely adopted among various practical applications during the past decades, the pros and cons of the approach are both evident against different uncertainty scenarios. Readers should select the appropriate uncertainty quantification method according to their specific requirements.

Remark 1. The probabilistic analysis theory has a wide range of variations, e.g., perturbation method, surrogate model and eigenfunction expansion method [167,169–174]. The implementation of the probabilistic philosophy is rather direct to the general finite element procedure and now has been adopted to some commercial FE software (e.g., Comsol Multiphysics). By adopting this technique, the statistical descriptions (e.g., mean and deviation) of possible structural responses can be provided, then based on which, the potential safety and reliability assessment of structure can be estimated under varied environmental conditions.

Remark 2. Despite the probabilistic analysis theory has been prevalently adopted among different engineering disciplines, the applicability of the method has been greatly affected by the completeness of system uncertain profiles (i.e., distribution, mean and error). That is, the probabilistic approach requires statistically based or inferred random parameters to fulfil the entire quantification, Moreover, techniques exist to elicit probabilistic information from sparse or limited data, supported by Bayesian and other updating methods to more accurately characterize random parameters [175].

3.2. Non-probabilistic analysis theory

For some practical engineering cases, the variability of the system properties is not fully known. As an alternative, the non-probabilistic analysis theory uses limited uncertainty information as fuzzy, convex and interval variables to describe the events, and relevant structural responses could be estimated.

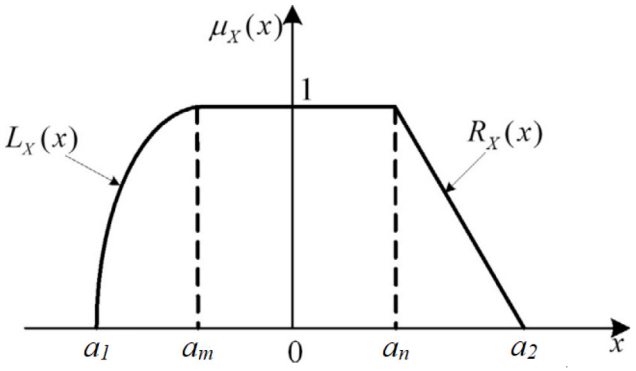

Fig. 7. The membership function.

3.2.1. Fuzzy set method

The fuzzy variable X should be expressed through the normalized membership function $\mu_X(x)$ as

$$0 \le \mu_X(x) \le 1, \ \forall x \in \mathbb{R} \tag{61}$$

$$\exists x^l, x^u \text{ with } \mu_X(x) = 1 \ \forall x \in \left[x^l, x^u\right] \tag{62}$$

Take a fuzzy parameter X into consideration, the membership function has been illustrated in Fig. 7 with an increasing left branch monotonic function $L_X(x)$ and decreasing right branch monotonic function $R_X(x)$ with X, and the corresponding equation is

$$\mu_X(x) = \begin{cases} L_X(x) & a_1 \le x \le a_m \\ 1 & a_m \le x \le a_n \\ R_X(x) & a_n \le x \le a_2 \end{cases} \tag{63}$$

Based on the λ level sets of the fuzzy variables, it is easy to denote the convex fuzzy variable X by a group of λ level sets $X(\lambda)$.

$$X(\lambda) = \left\{\left[x^l(\lambda), x^u(\lambda)\right], \lambda \in [0, 1]\right\} \tag{64}$$

For each λ level, the set of $X(\lambda)$ is at a connected interval $\left[x^l(\lambda), x^u(\lambda)\right]$, the bounds $x^l(\lambda)$ and $x^u(\lambda)$ for $\lambda \neq 0$ are given as

$$\begin{cases} x^l(\lambda) = \min\left[x \in \mathbb{R} \,|\mu_X(x) \ge \lambda\right] = (L_X)^{-1}(\lambda) \\ x^u(\lambda) = \min\left[x \in \mathbb{R} \,|\mu_X(x) \ge \lambda\right] = (R_X)^{-1}(\lambda) \end{cases} \tag{65}$$

The $S_X = \{x \in \mathbb{R} \,|\mu_X(x) \ge 0\}$ is the support set, which is the λ level set $X(\lambda)$ of $\lambda = 0$ against Eq. (65). The boundaries of $X(\lambda = 0)$ are

$$\begin{cases} x^l(\lambda = 0) = \lim\limits_{\lambda' = +0} \left\{\min\left[x \in \mathbb{R} \,\middle|\, \mu_X(x) \ge \lambda'\right]\right\} \\ x^u(\lambda = 0) = \lim\limits_{\lambda' = +0} \left\{\min\left[x \in \mathbb{R} \,\middle|\, \mu_X(x) \ge \lambda'\right]\right\} \end{cases} \tag{66}$$

Considering $x^c(\lambda)$ and $x^r(\lambda)$ as the centre value and radius of the connected interval $X(\lambda)$, respectively, the formulation can be

$$\begin{cases} x^c(x) = \dfrac{x^l(\lambda) + x^u(\lambda)}{2} \\ x^r(x) = \dfrac{x^u(\lambda) - x^l(\lambda)}{2} \end{cases} \tag{67}$$

The interval $X(\lambda)$ can be characterized as follows if transforming it into the normalized interval

$$X(\lambda) = x(\lambda, \delta) = x^c(\lambda) + x^r(\lambda)\delta \tag{68}$$

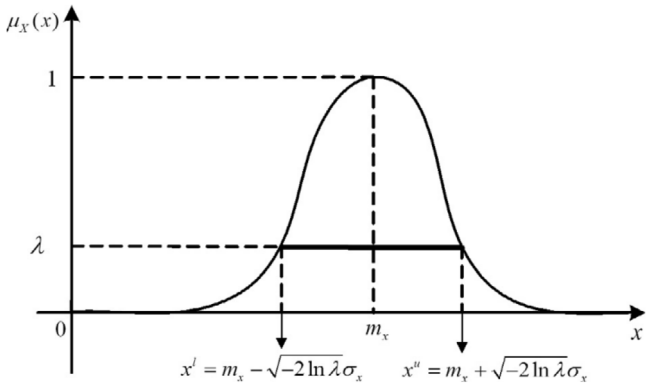

Fig. 8. The membership function of the Gaussian fuzzy variable X and its bounds at the membership level λ.

In which $\lambda \in [0, 1]$ and $\delta \in [-1, 1]$ representing the normal and normalized interval parameters. Subsequently, X should be expressed as a series format in the dimension $x\ (\lambda, \delta)$.

For the membership equation with respect to X is denoted a Gaussian kind as shown in Fig. 8 and Eq. (69).

$$\mu_X(x) = \exp\left\{-\frac{(x - m_x)^2}{2\sigma_x^2}\right\} \tag{69}$$

In which m_x and σ_x represent the middle result and point of X. In this case, the fuzzy parameter X can be named as Gaussian fuzzy parameter.

Based on Eq. (68), the fuzzy parameter is:

$$X = x(\lambda, \delta) = m_x + \sqrt{-2\ln\lambda}\sigma_x\delta \tag{70}$$

The boundaries and membership level λ of fuzzy parameter is found in Fig. 8.

3.2.2. Interval analysis method

As an extension of the traditional interval analysis method, the interval field was proposed by considering the spatially related uncertainty into the lower and upper bounds of the interval box [176–178]. Based on the available uncertainty information, the lower bound function ($\underline{I}(\xi)$) and upper bound function ($\overline{I}(\xi)$) of random coefficients are generated to represent the extreme values of the collected samples at structural locations as shown in Fig. 9. Unlike the traditional interval analysis with constant lower and upper bounds, the interval field considers the spatially varied dependency at different locations with changing boundary conditions.

Like the Karhunen–Loève (K–L) expansion in SSFEM, the interval field also requires effective discretization technique to discretize the datapoints. Assume a discretization technique $\hat{I}(\xi)$ with a series of interval parameters $\{I_p,\ p = 1, \ldots, n\}$, the interval field is represented through

$$I(\xi) \approx \hat{I}(\xi) = \Gamma(\xi, \mathbf{I}) \tag{71}$$

$$\hat{I}(\xi) := \frac{\int_{\Psi_i} I(\xi) d\,\Psi_i}{|\,\Psi_i\,|} = \hat{I}_i,\ \xi \in \Psi_i \tag{72}$$

where Ψ_i is the region of ith element. Subsequently, the lower and upper bound functions of the interval field can be discretized as

$$\mathbf{I} \in \widetilde{\Omega} := \left\{\mathbf{I} \in \Re^n \left| \widehat{\underline{I}}_i \le \hat{I}_i \le \overline{\hat{I}}_i,\ i = 1, \ldots, n \right.\right\} \tag{73}$$

where $\widehat{\underline{I}}_i$ and $\overline{\hat{I}}_i$ are the lower and upper bounds of $\hat{I}_i$. In the meantime, the midpoint of interval field can be expressed as

$$\mathbf{I}^c \in \widetilde{\Omega} := \left\{\mathbf{I}^c \in \Re^n \left| \hat{I}_i^c = \frac{\widehat{\underline{I}}_i + \overline{\hat{I}}_i}{2},\ i = 1, \ldots, n \right.\right\} \tag{74}$$

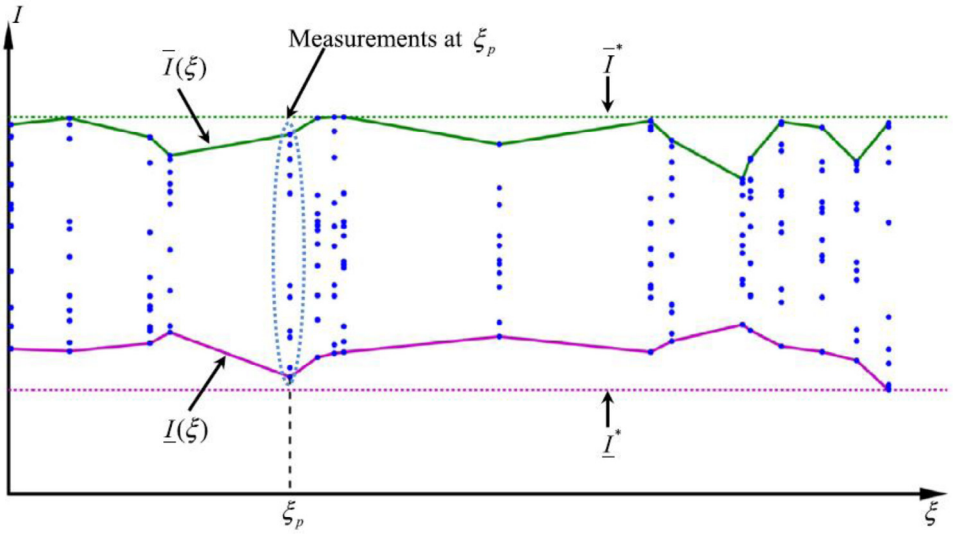

Fig. 9. Illustration of one-dimensional interval field [179].

Based on the transformation, the interval field can be discretized into normal interval vectors with known lower and upper bound functions, which makes the implementation of interval field accessible to standard FE approximation.

3.2.3. Remarks

The non-probabilistic analysis theory has been an alternative for probabilistic approaches for several decades. It focuses on uncertainty analysis with limited knowledge of the information of the uncertain system inputs, which has been combined with various theoretical and mathematical formulations to generate different uncertainty quantification techniques. However, some limitations also exist for the non-probabilistic theory and should be selected as needed.

Remark 1. The advantage of the non-probabilistic analysis theory is its adaptivity of different uncertainty environments with sufficient and insufficient information. Within the framework, various convex, fuzzy and interval techniques are established then implemented into the FE approximation of static, dynamic, nonlinear and fracture mechanism for practical applications against varied environment. Unlike the probabilistic approach of generating completed profiles, the non-probabilistic approach such as the interval method, only requires the extreme bounds of the system random parameters to construct the inputs. Due to the conceptual simplicity, many computational tools have been developed.

Remark 2. A disadvantage of the non-probabilistic approaches, for instance, is that the number of involved fuzzy variables must be relatively small to maintain good performance. Also, for the convex model, explicit functions that representing the relationship between uncertainties and the complex physical behaviour cannot be provided, which prevents the practical implementation in structural uncertainty analysis. Another issue for the interval analysis method is that the dependency between different material properties cannot be fully tracked. Moreover, the computational efficiency of interval analysis for certain random simulation cases may be low.

4. Challenges of the numerical modelling of random cracking

As illustrated in the established literature, the numerical modelling of random cracking in different media presents numerous challenges. In this paper, two major issues are summarized: (1) random crack approximation, (2) random crack propagation and cost-efficiency. The following sections discuss the two points among different random crack quantification techniques.

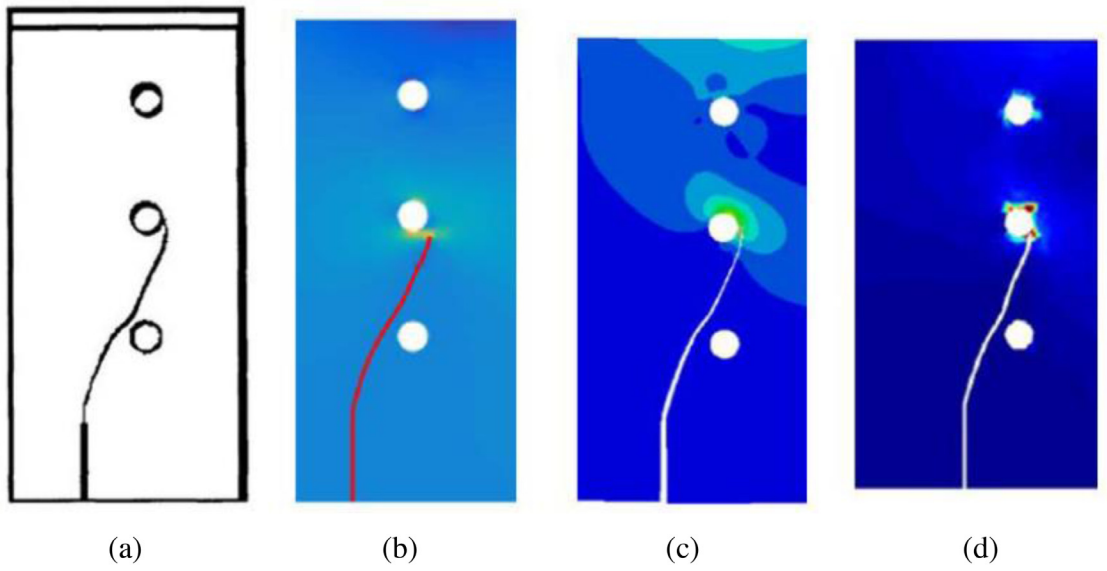

Fig. 10. Crack propagation paths for (a) experimental, (b) meshfree, (c) XFEM, and (d) LEFM crack models [180–184].

4.1. Random crack approximation

As the first challenge for the numerical modelling of random cracks, the capability of accurate approximation of the crack is critical. This includes the reliability of the discrete model and the handling of the randomness involved in the physical mechanism.

Different crack and stress behaviours may be predicted by adopting different models, like the three-point bending beam test shown in Fig. 10 through multiple crack models [180–184]. Thus, a proper physical crack model needs to be selected for the concerned structure towards an appropriate geometrical approximation for the cracking.

Among vast range of research works, most of the random fracture analysis of structures adopted the statistical theory of probability, based on which the random system properties (i.e., loading, material properties and fracture parameters) are considered as random fields or variables with certified distributions. As a simple and direct computational tool of the random crack problem, the MCS method is widely used for simulating the structural fracture performance with important randomness of input coefficients [185–188]. For instance, in [189], the crack size, Young's modulus, load stress, and fracture toughness are modelled as random variables, and the crack intensity factors are collected as random outputs to justify the failure conditions of structures under different failure modes. The input examples can be simulated as Gaussian and non-Gaussian types through:

$$f(x) = \frac{1}{\sqrt{2\pi S^2}} e^{-\frac{(x-\mu)^2}{2S^2}}, \quad f(x) = \frac{1}{\sqrt{2\pi S^2}} e^{-\frac{(\ln x-\mu)^2}{2S^2}} \tag{75}$$

where $f(x)$ denotes the probability density function, S and μ are the statistical parameters representing the standard deviation and mean values. Among the large numbers of MCS simulation cycles N, the failure cases within the samples are collected and recorded as N_f, then the estimation of probability of failure can be defined by

$$P_f = \frac{N_f}{N} \tag{76}$$

As noted from the expression of probability of failure, the number of MCS simulations must be large enough to satisfy the convergence of reliability. Moreover, the integral type of calculation can be analytically used to calculate the probability of failure as

$$\begin{aligned} P_f &= \Phi(-\beta), \\ \beta &= \frac{\mu_{K_{IC}} - \mu_K}{\sqrt{S^2_{K_{IC}} - S^2_K}} \end{aligned} \tag{77}$$

where β denotes the reliability index for fracture failure, $\Phi(x)$ denotes the cumulative probability distribution function as

$$\Phi(\mathbf{x}) = \frac{1}{\sqrt{2\pi}} \int_{-\infty}^{\mathbf{x}} e^{\frac{-t^2}{2}} dt \tag{78}$$

It should be noticed that although the required number of simulations to probabilistically characterize the critical stress intensity factor (KIC) is not large as the crude MCS method, Eq. (77) is restricted to input variables only with Gaussian distribution and this may be insufficient for most practical engineering applications. However, more advanced structural reliability techniques exist that can consider non-Gaussian random variables, non-linear limit states, correlated variables, etc, such as the widely used First Order Reliability Method (FORM) and highly efficient importance sampling simulation methods [175,190,191].

In fact, for actual fracture analysis, the precise distributions of material properties or external loadings are not difficult to monitor, but for some geometrical random parameters (i.e., crack size and crack angles), it would be difficult to acquire the detailed distribution information. Thus, the non-probabilistic theory is used to solve the random fracture analysis [192–195]. For instance, in [196], the crack length, height and angle parameters are modelled as interval variables, and the corresponding probability of failure for the cracked body can be defined by

$$P_f = \Pr\{g(\mathbf{X}, \mathbf{Y}) \leq 0\},\ g(\mathbf{X}, \mathbf{Y}) = K_{IC} - K(\mathbf{X}, \mathbf{Y}) \tag{79}$$

where K denotes the mode-I stress intensity factor or the effective intensity factor under mix-mode fracture, $Y_i, i = 1, 2, \ldots, m$ are the interval variables defined by

$$\begin{aligned} &Y_i \in \left[Y_i^L, Y_i^R\right],\ i = 1, 2, \ldots, m \\ &Y_i^c = \frac{Y_i^L + Y_i^R}{2},\ Y_i^r = \frac{Y_i^R - Y_i^L}{2},\ \gamma_i = \frac{Y_i^r}{Y_i^c} \end{aligned} \tag{80}$$

where Y_i^L, Y_i^R, Y_i^c, Y_i^r and γ_i denotes the lower, upper bounds, central location, radius and degree of uncertain interval parameters.

As shown in Fig. 11, the interval limit state function has a bandwidth representing the maximum and minimum limit state values through the interval parameter $\mathbf{Y}$. Thus, the probability of failure domain for the cracked structure can be expressed as

$$P_f^L = \Pr\left\{\max_{\mathbf{Y}} g(\mathbf{X}, \mathbf{Y}) < 0\right\},\ P_f^R = \Pr\left\{\min_{\mathbf{Y}} g(\mathbf{X}, \mathbf{Y}) < 0\right\} \tag{81}$$

where P_f^L and P_f^R are the lower and upper bound of probabilities of failure.

For the crude MCS method, the uncertainty quantification of random crack initiation and propagation are straightforward and simple to implement, but the input parameters require probabilistic distribution information, and the computational samples are typically large. However, importance sampling, response surface methods and other standard simulation techniques are significantly more efficient than crude MCS, and representing the state-of-the-art in structural reliability methods [175].

For the interval-based methods, some ambiguous parameters can be defined with probability box without the need of precise distribution. This certainly provides convenience for practical engineering applications. However, the interval box still needs to be limited to a small range and large variance parameters may not be acceptable. Moreover, not all material or fracture properties can be defined by interval variables due to the dependency of formulation derivations. For stochastic crack analysis, the generality of non-probabilistic theory still needs to be extended for more practical engineering applications.

4.2. Random crack propagation and cost-efficiency

For the subsequent challenge of random crack initiation, the random crack directions of propagation matter for most practical engineering applications. The appropriate judgement of crack direction remains difficult in both discrete and continuous crack models, and the overall complexity of cracked system can be magnified especially after the consideration of random system properties.

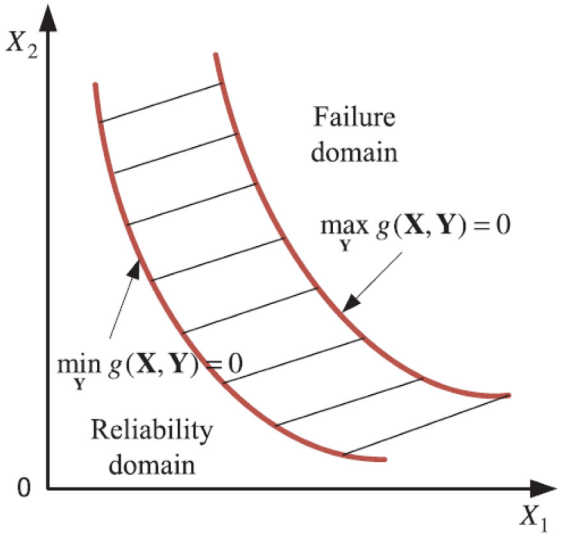

Fig. 11. The interval limit-state band of the fracture failure state [196].

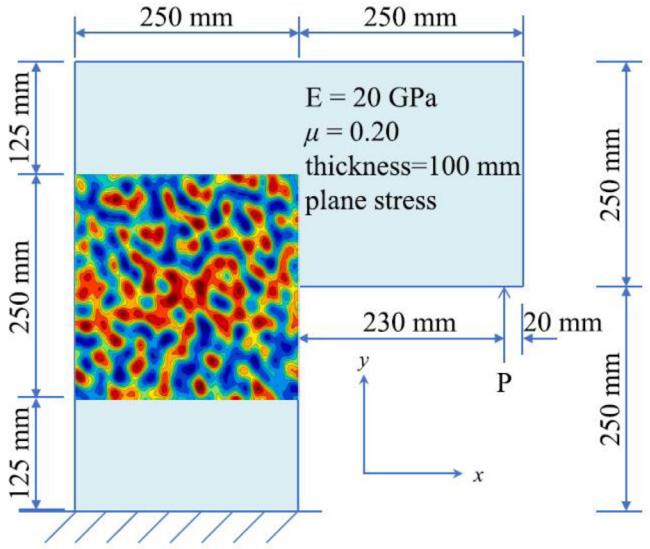

Fig. 12. Geometrical information and random field model of L-shape concrete [199].

The random crack propagation problem is significant for practical engineering applications since the fluctuations of system properties could result in completely different predictions of the structural remaining capacity and critical load [197,198]. It should be noted that for the deterministic crack propagation, the discrete and continuous crack models could generate only one but inconsistent crack growth path for the same structure. However, the involvement of random parameters may provide a failure zone that contains various possible crack paths for the whole structure to implement vulnerability assessment under different random scenarios. For instance, in [199], the Young's modulus, Poisson's ratio, density, fracture energy and tensile strength of aggregate and mortar can be modelled as random fields (RFs) for the concrete as shown in Fig. 12, and a regularized crack model of phase-field method is adopted to analyse the crack behaviour. Different crack growth paths are observed under different random field conditions as shown in Fig. 13.

To calculate all the possible crack growth paths, crude MCS with 100 simulation runs was used to construct a crack zone for the concrete as shown in Fig. 14(a). From the plots, the crack paths were tracked 100 times and the

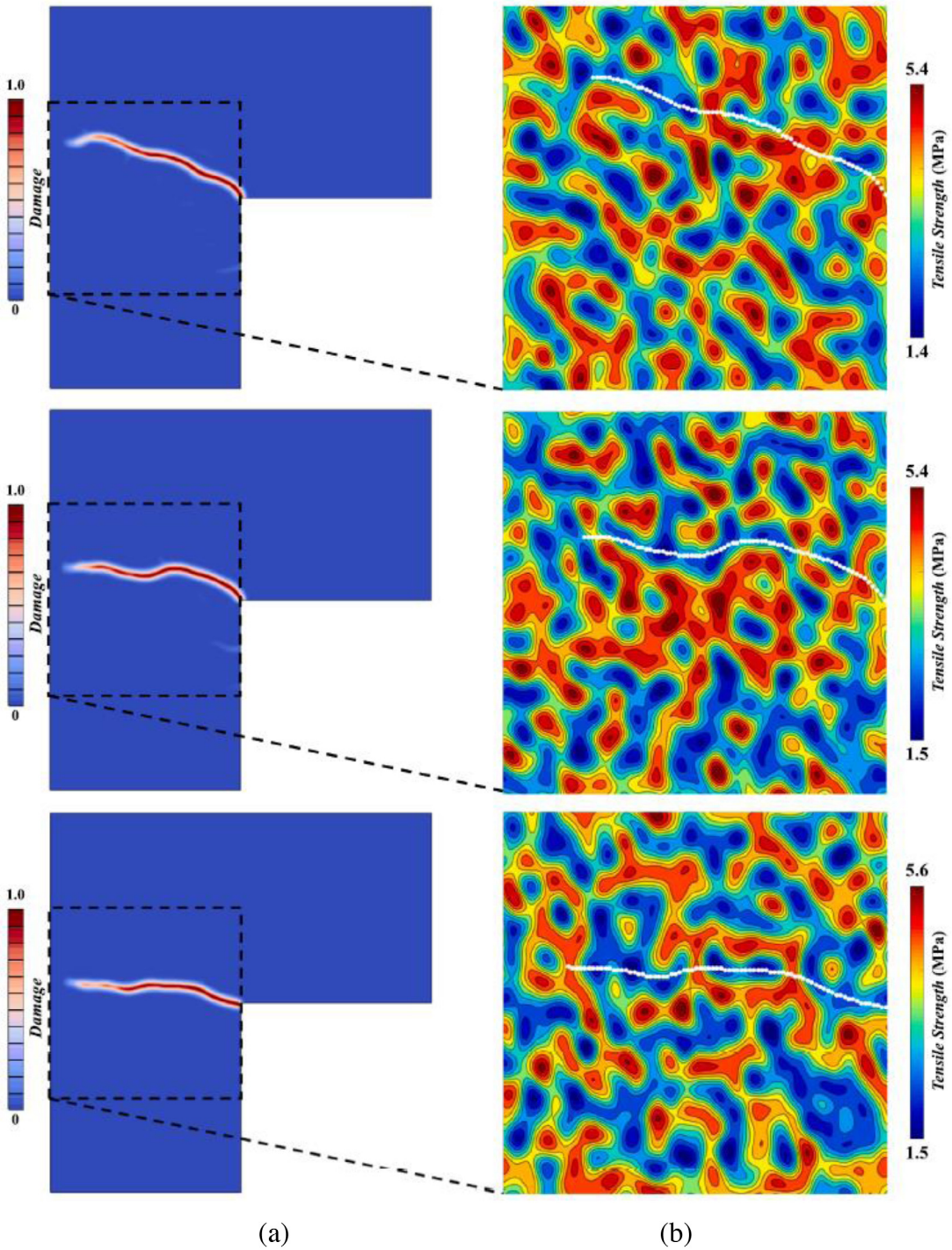

Fig. 13. Examples of (a) different damage shapes of L-shape concrete and (b) magnified crack growth paths under different random fields [199].

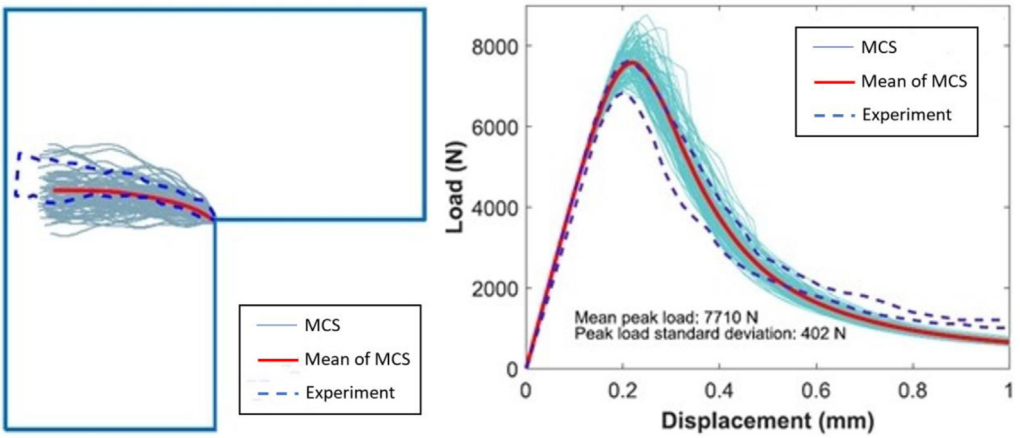

Fig. 14. Comparisons of numerical simulated and experimental: (a) crack growth paths and (b) load–displacement curves under 100 random fields of L-shape concrete [199].

mean path matched well with the experimental crack result. Also, the experimental envelop has been completely covered by the predicted crack zone, which illustrates the MCS-based random crack propagation analysis could match the inadequate fracture information provided by the limited number of costly experimental tests. Moreover, from Fig. 14(b), the predicted mean critical load during the crack propagation process simulates well with the experimental results. Thus, the reliability analysis of structure due to the fluctuations in system properties could be obtained from the distribution of critical loads under different environmental scenarios.

Moreover, the correlation length parameter within the correlation function of the random field has influences upon the nondeterministic fracture behaviours [200,201]. For instance, in [201], the authors consider different length parameters (i.e., 0 mm, 12.5 mm, 25 mm, 100 mm, 200 mm, and infinite value) to simulate various spatial fluctuations and correlations of the field. By collecting responses from the notched beam, the authors found that the average responses for the fracture specimen are almost identical, but the standard deviation of the response depends on the correlation length parameter. With the increasement of the length parameter, the standard deviation of fracture responses rises. And the fracture specimen with 0 mm length parameter is almost identical to the deterministic model. Moreover, the size and shape of the Fracture Process Zone (FPZ) is independent of the correlation length or variance of the random field, but will be sensitive around the material's characteristic length value.

Although the random crack propagation analysis has been widely investigated among many applications, the cost-efficiency of the developed FE techniques remains a major challenge. Most of the techniques are mesh-dependent and the accuracy of the simulated results relies a large extent on the total degree of freedom of the cracked structure, especially in the crack growth zone. For instance, the popular smeared crack models of nonlocal damage and phase-field analysis, the mesh-dependency problem would directly affect the crack trajectory [202,203].

Besides, for one deterministic crack propagation analysis, the normal computational cost for a single FE simulation could be hours or days. To construct the training dataset to quantify all possible crack paths for structures, the samples of input parameters could be at least 1000. By using the crude MCS method, the repetitive full-scale FE simulations should be executed to calculate the dataset of the outputs by using all the realizations of the uncertain inputs. This may make the overall computations experimentally or numerically infeasible to achieve. Even with the non-probabilistic theories, the computational effort issues cannot be ignored with the need of constructing a reliable response surface plane. Thus, the cost-efficiency of random crack propagation analysis through the typical probabilistic or non-probabilistic theories is a major burden and needs to be further modified.

5. Future trend: machine learning aided non-deterministic fracture mechanics

As mentioned earlier, the random crack modelling is computationally expensive by using the traditional uncertainty quantification techniques and hence, the aim of quantitatively assessing the effects of uncertainties

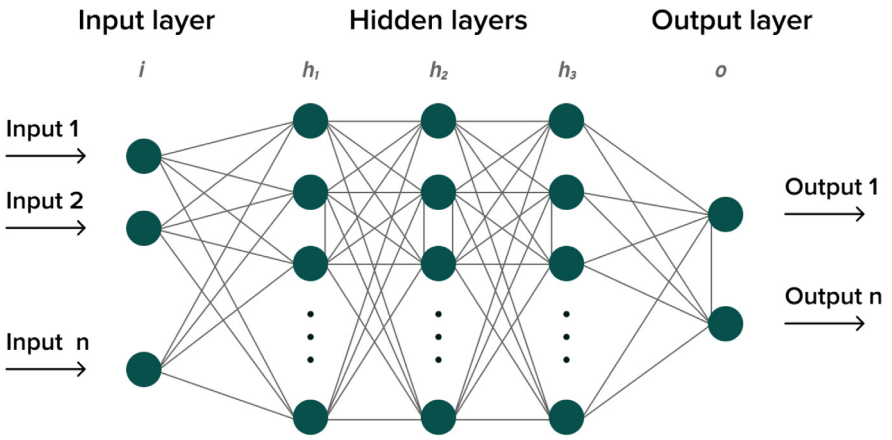

Fig. 15. The basic structure of neural network.

against the crack growth process remains a critical issue. As a robust alternative to avoid the large number of repetitive full-scale FE calculations, the machine learning techniques or data-driven algorithms in recent years have been implemented within the traditional methods to construct a surrogate model which is capable of representing the correlation between the various system input and output results only through a small group of training dataset. In this section, several typical methods of machine learning and the implementation with non-deterministic fracture mechanics are briefly introduced.

5.1. Neural networks

In recent years, the data-driven and artificial intelligent techniques are widely adopted in practical engineering applications to resolved complicated problems. Among which, the neural networks (NN) method has been used as "smart" systems for different complex scenarios of control systems, image processing and fracture mechanism identification. The advantage of the NN is the excellent regression capability of analysing the correlation between the system inputs and the responses. In this fracture mechanics, the NN can be combined with the damage identification to detect any crack initiation or propagation status. Normally, the NN framework consists of three parts which consists of hidden, input and output layers as shown in Fig. 15.

The NN has a series of cells that are related with each other and the major aim of the input layer is to use the information as sources from both numerical model and experimental tests. Subsequently, each cell calculates the relation functions and the predict output responses. The summation equation has been considered through the sum of weighted output responses as follows

$$NET_i = \sum_{j=1}^{n} w_{ij} x_j + w_{bi} \tag{82}$$

where i, j denote processing elements, w_{bi} denotes the bias of each layer, w_{ij} denotes the weight of connections, x_j denotes the output response.

Then, the output response of the NN can be analysed from hidden layers as

$$f(NET_i) = \frac{1}{1 + e^{-NET_i}} \tag{83}$$

The MSE of NN is defined by

$$MSE = \frac{1}{N} \sum_{1}^{N} (y_i - \hat{y}_i)^2 \tag{84}$$

where N denotes the size of data, y_i and $\hat{y}_i$ are the actual and predicted output responses, respectively.

5.2. Kriging

As another popular machine learning technique, the Kriging or known as the Gaussian process method has been frequently adopted in different cases. Given x as the input variable, y as the output response, the Kriging technique is expressed as

$$y\left|x;\mathbf{B},\sigma,\boldsymbol{\theta}\sim GP(\mu(x;\mathbf{B}),\sigma^2R(x_1,x_1;\boldsymbol{\theta})\right. \tag{85}$$

where $\mu(\cdot;\mathbf{B})$ denotes the mean equation, $R(\cdot,\cdot;\boldsymbol{\theta})$ denotes the kernel function, $\mathbf{B}$, σ, $\boldsymbol{\theta}$ are the Bayesian optimization hyperparameters involved in the Gaussian process. It should be noticed that the ultimate performance of the Gaussian process depends on a large extent of the selections of the hyperparameters [204,205].

As an extension of the Kriging model, a modified universal Kriging method was developed with higher prediction accuracy [206,207]. The major improvement of the universal Kriging is the implementation of the multivariate polynomial mean function as follows

$$\mu(\cdot;\mathbf{B})=\sum_{i=1}^{P}a_ib_i(x) \tag{86}$$

where a_i denotes the coefficients for the basis function $b_i(x)$. Then, a large variance of input data can be handled within the Kriging model by using a design matrix and a correlation matrix as:

$$F=\begin{pmatrix}b_1(x^1) & \dots & b_p(x^1)\\ \vdots & \ddots & \vdots\\ b_1(x^n) & \dots & b_p(x^n)\end{pmatrix} \tag{87}$$

$$\psi=\begin{pmatrix}\psi(x^1,x^1) & \dots & \psi(x^1,x^n)\\ \vdots & \ddots & \vdots\\ \psi(x^n,x^1) & \dots & \psi(x^n,x^n)\end{pmatrix} \tag{88}$$

where $F(\cdot)$ and $\psi(\cdot,\cdot)$ are the design and correlation matrix defined within the stochastic process.

For the Gaussian process, the correlation matrix $\psi(x,x')=\prod_j\psi_j(\theta,x_i-x_i')$ plays a very important role for the regression performance of the surrogate model, and some typical types of correlation matrix as introduced as follows

$$\begin{cases}\psi_j(\theta;d_j)=\exp(-\theta_j\left|d_j\right|), & \text{Exponential correlation}\\ \psi_j(\theta;d_j)=\exp(-\theta_jd_j^2), & \text{Gaussian correlation}\\ \psi_j(\theta;d_j)=\max\left\{0,1-\theta_j\left|d_j\right|\right\}, & \text{Linear correlation}\end{cases} \tag{89}$$

5.3. Extended support vector regression

The Support Vector Machine (SVM) has been developed for determining a certain boundary plane which holds the largest gap with the nearest random variables located on both sides of the hyperplane [208–211]. For a given input set of random variables being trained, which is denoted as $\mathbf{x}_{train}=[\mathbf{x}_{train,1},\mathbf{x}_{train,2},\dots,\mathbf{x}_{train,m}]^T\in\Re^{m\times n}$, the corresponding output set of variables $\mathbf{y}_{train}\in\Re^m$ illustrates the classifications that each group data stands. The decisions equation of determining the hyperplanes is:

$$\hat{f}(\mathbf{x})=\mathbf{w}^T\mathbf{x}-\zeta \tag{90}$$

where $\mathbf{w}=[w_1,w_2,\dots,w_i,\dots,w_n]^T\in\Re^n$ is the perpendicular plane with respect to the hyperplane; $\zeta\in\Re$ is the bias during the classification. As an extension of the traditional SVM, the extended support vector regression (X-SVR) was developed in [212] to improve the regression performance and the decision function. The X-SVR is modified as:

$$\hat{f}(\mathbf{x})=\mathbf{x}(\mathbf{p}-\mathbf{q})^T-\zeta \tag{91}$$

where $\mathbf{p}, \mathbf{q} \in \Re^n$ are the two positive hyperplane coefficients. The above equation is suitable for linear regression with patternable inputs. However, for the irregular ones, the method uses an implicit mapping function $\Theta(\mathbf{x})$ to transform the variables into the high-dimensional Euclidian space with regularized distributions:

$$\mathbf{x} = [x_1, x_2, \ldots, x_m]^T \Rightarrow \hat{\mathbf{k}}(\mathbf{x}) = \begin{bmatrix} \boldsymbol{\Theta}(\mathbf{x}_1)^T \boldsymbol{\Theta}(\mathbf{x}_1) \\ \boldsymbol{\Theta}(\mathbf{x}_2)^T \boldsymbol{\Theta}(\mathbf{x}_2) \\ \vdots \\ \boldsymbol{\Theta}(\mathbf{x}_m)^T \boldsymbol{\Theta}(\mathbf{x}_m) \end{bmatrix} = \begin{bmatrix} k(\mathbf{x}_1, \mathbf{x}_1) & k(\mathbf{x}_1, \mathbf{x}_2) & \cdots & k(\mathbf{x}_1, \mathbf{x}_m) \\ k(\mathbf{x}_2, \mathbf{x}_1) & k(\mathbf{x}_2, \mathbf{x}_2) & \cdots & k(\mathbf{x}_2, \mathbf{x}_m) \\ \vdots & \vdots & \cdots & \vdots \\ k(\mathbf{x}_m, \mathbf{x}_1) & k(\mathbf{x}_m, \mathbf{x}_2) & \cdots & k(\mathbf{x}_m, \mathbf{x}_m) \end{bmatrix} \tag{92}$$

where $\hat{\mathbf{k}}(\mathbf{x})$ is the empirical kernelized vector, and the kernelized format of X-SVR is shown as

$$\min_{\mathbf{p}_k, \mathbf{q}_k, \delta, \vartheta, \hat{\vartheta}} : \frac{\gamma_1}{2} \left(\|\mathbf{p}_k\|_2^2 + \|\mathbf{q}_k\|_2^2 \right) + \gamma_2 \mathbf{e}_m^T (\mathbf{p}_k + \mathbf{q}_k) + \frac{\theta}{2} \left(\vartheta^T \vartheta + \hat{\vartheta}^T \hat{\vartheta} \right) \tag{93}$$

$$s.t. \quad \begin{cases} \hat{\mathbf{k}}(\mathbf{x})(\mathbf{p}_k - \mathbf{q}_k) - \delta \mathbf{e}_m - \mathbf{y} \leq \lambda \mathbf{e} + \vartheta \\ \mathbf{y} - \hat{\mathbf{k}}(\mathbf{x})(\mathbf{p}_k - \mathbf{q}_k) + \delta \mathbf{e}_m \leq \lambda \mathbf{e}_m + \hat{\vartheta} \\ \mathbf{p}_k, \mathbf{q}_k \geq \mathbf{0}^n; \vartheta, \hat{\vartheta} \geq \mathbf{0}^m \end{cases} \tag{94}$$

where $\vartheta, \hat{\vartheta}$ are the redundant constrain coefficients; γ_1, γ_2 are the tuning parameters; θ is the penalty; λ is the tolerable deviation; k denotes the kernelized process. Based on the optimization theory adopted in the DrSVM model [212], the regression function can be simplified as a quadratic programming process by introducing a non-negative Lagrange multiplier $\boldsymbol{\beta}_k \in \Re^{4m}$ as:

$$\min_{\boldsymbol{\beta}_k} : \frac{1}{2} \boldsymbol{\beta}_k^T \mathbf{P}_k \boldsymbol{\beta}_k - \mathbf{L}_k^T \boldsymbol{\beta}_k, \ \ \boldsymbol{\beta}_k \geq \mathbf{0}_{4m} \tag{95}$$

where $\mathbf{P}_k$ and $\mathbf{L}_k$ are optimization vectors and matrix defined in Appendix. Considering $\boldsymbol{\beta}_k^* \in \Re^{4m}$ as the obtained global optimum solution for the optimization problem, the overall governing equation of the kernelized X-SVR model can be reformulated as

$$\begin{cases} \hat{f}_N(\mathbf{x}) = (\mathbf{p}_k - \mathbf{q}_k)^T \hat{\mathbf{k}}(\mathbf{x}) - \hat{\mathbf{e}}_k^T \hat{\mathbf{H}}_k \boldsymbol{\beta}_k^* \\ \mathbf{p}_k - \mathbf{q}_k = \mathbf{v}_k(1:m) - \mathbf{v}_k(m+1:2\ m), \ \ \mathbf{v}_k = \hat{\mathbf{T}}_k^{-1}((\hat{\mathbf{R}}_k + \mathbf{I}_{4m \times 4m})^T \boldsymbol{\beta}_k^* - \gamma_2 \mathbf{u}_k) \end{cases} \tag{96}$$

Like the Gaussian process, the ultimate performance of the regression depends on the selected kernel function. Hence, a new type of feature mapping kernel, namely the Dirichlet feature mapping has been proposed, which is defined recursively by

$$\varphi_d^{\alpha}(\mathbf{x}) = \begin{cases} x_d, & x_d \in \mathbf{x}, \ d = 1, 2, \ldots, n \\ \dfrac{\Gamma(\sum_{k=1}^n \alpha_k)}{\prod_{k=1}^n (\Gamma(\alpha_k))} \prod_{k=1}^n x_k^{\alpha_k - 1} \times (1 - \sum_{k=1}^{n-1} x_k)^{\alpha_n - 1}, & d = n+1. \end{cases} \tag{97}$$

where $d \in \mathbf{Z}^+$ is the polynomial order. More details can be read in [75,213].

5.4. Machine learning based non-deterministic fracture analysis

The aim of machine learning based non-deterministic fracture analysis is to accelerate the handling of the random responses of the cracked structures through the probabilistic and non-probabilistic frameworks. For the probabilistic framework, the stochastic descriptions of the uncertainty information are vital and various machine learning algorithms as mentioned above could be coupled with the FE codes for the fracture analysis. To obtain all the possible output responses, the training samples are collected first based on the design of experiment (DoE) principle. Normally, the Latin cube and Sobol's consequence sampling schemes are adopted [214,215]. Then, the training samples will be calculated through the FE solver and the structural responses will be collected.

Subsequently, the machine learning algorithms are used to train the surrogate model which can be validated with the MCS results. In the end, the potential failure behaviours of the cracked structures can be predicted directly

Table 1
Material properties of the wedge splitting test.

Material property	Deterministic value
Young's modulus (MPa)	28300
Poisson's ratio	0.18
Tensile strength (MPa)	2.12
Tensile fracture energy (J/m^2)	373

from the machine learning models and the relevant probability density and cumulative distribution functions are estimated in an efficient manner. A flowchart representing the procedures of machine learning based probabilistic fracture analysis is provided in Fig. 16.

For the non-probabilistic framework, the fuzzy based non-probabilistic fracture analysis is implemented for the fracture analysis of the cracked structures. For this scheme, the deterministic fracture solution is solved at $\alpha = 1$ level then towards the lower $\alpha-$ cut levels by adopting the interval analysis. Due to the non-monotonic nature of the practical engineering applications, an additional maximization and minimization method against multiple outputs is used. Then, the machine learning algorithms are used to train the surrogate model by replacing the repetitive MCS simulations. And the established surrogate model can directly predict the maximum and minimum results of structural response at arbitrary $\alpha-$ cut level [216]. In the end, the fuzzy based output membership function is formulated under real-life random environments. A flowchart representing the procedures of machine learning based fuzzy fracture analysis is provided in Fig. 17.

6. Examples and discussion

In this section, some numerical investigations using different crack models and uncertainty quantification methods to solve the non-deterministic fracture problems are presented. Some popular benchmark examples, which have been frequently validated and extended in the fracture mechanics, are selected herein. The aims of this section are to (1) assess the actual simulation abilities of the embedded, smeared and regularized techniques against different applications, (2) compare different uncertainty quantification performance of the probabilistic and non-probabilistic approaches when varied system uncertainties are considered into the crack models.

6.1. Deterministic fracture analysis

The deterministic numerical analysis of the fracture problem is discussed in this subsection. Based on Refs. [217, 218], a series of geometrically varied wedge splitting specimens are tested and numerically simulated using the XFEM, crack band, and phase field methods. For this mode I fracture test, the potential crack propagation is a vertical path along the notch. Thus, different crack models should converge to the same failure pattern, but with discrepant computational cost.

The geometrical and boundary information of the wedge splitting test is presented in Fig. 18, and the basic dimension of the specimen is 80 cm × 80 cm × 40 cm with a central notch. Two opposite directed horizontal forces are applied at the notch to generate crack. The material properties of the specimen are listed in Table 1 and implemented into different crack models.

The two-dimensional numerical test is carried out under plane strain condition and the quadrilateral finite element with minimum size of 1 cm is adopted to mesh the geometry as shown in Fig. 19. It should be noticed that the different FE size levels may be used by different crack models based on the specific simulation performance, and the minimum FE size of the phase field method is approximately as 0.1 cm.

In Fig. 20, the load–CMOD curves during the crack growth process were plotted for the three different methods [217–219]. The three generated curves were almost identical and very little differences were observed. That is, with the same material properties, the constitutive relations and nonlinear behaviour descriptions among the three techniques are consistent. However, it should be noticed that although the simulation results are almost same for the three methods, the corresponding computational costs are varied. Since the phase field method requires a much finer mesh to achieve functional convergence, the computational time is accordingly much larger than the other two methods. Similar conclusions can be obtained for the extended three-dimensional wedge splitting test [220].

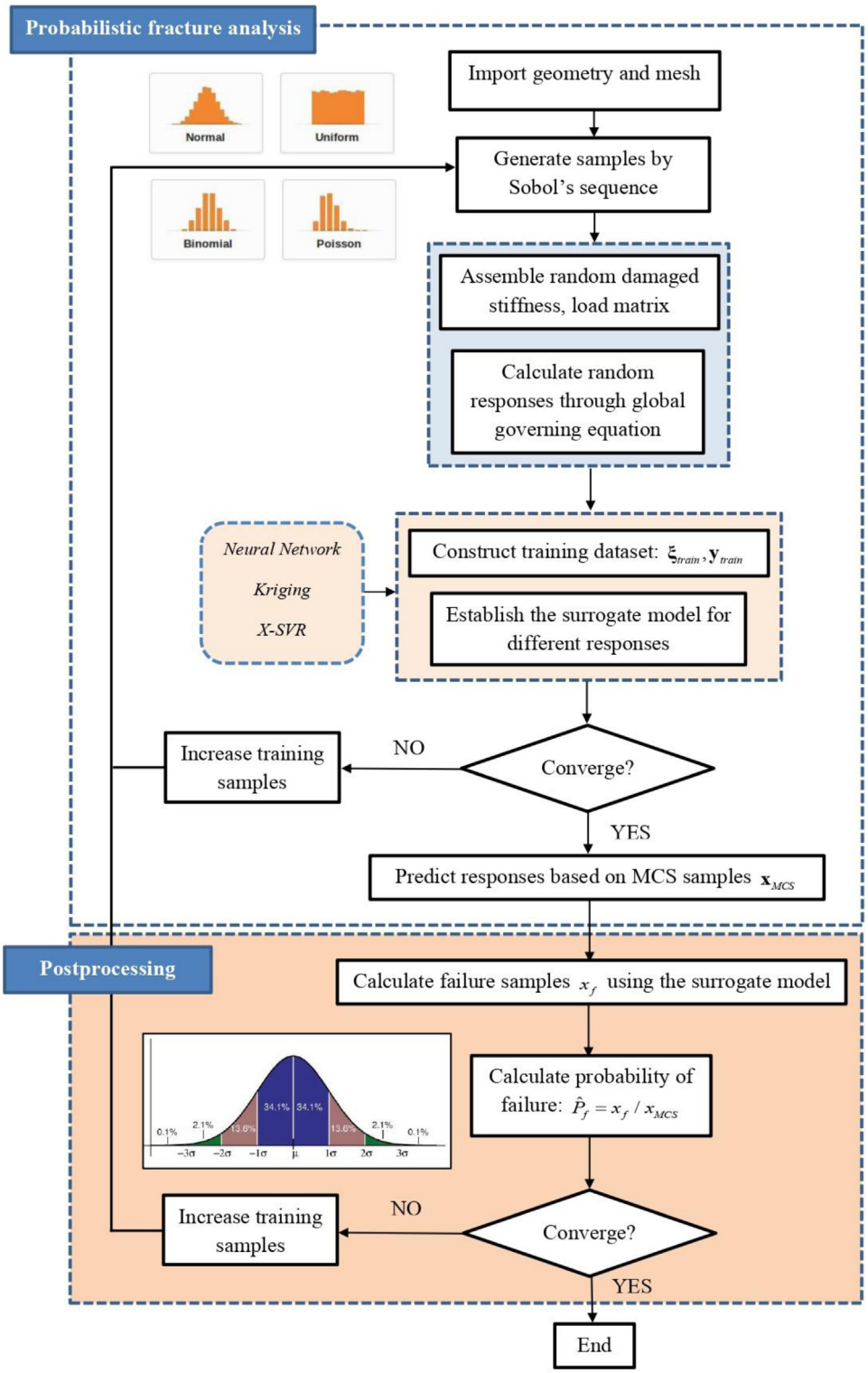

Fig. 16. A flowchart of machine learning aided probabilistic fracture analysis framework.

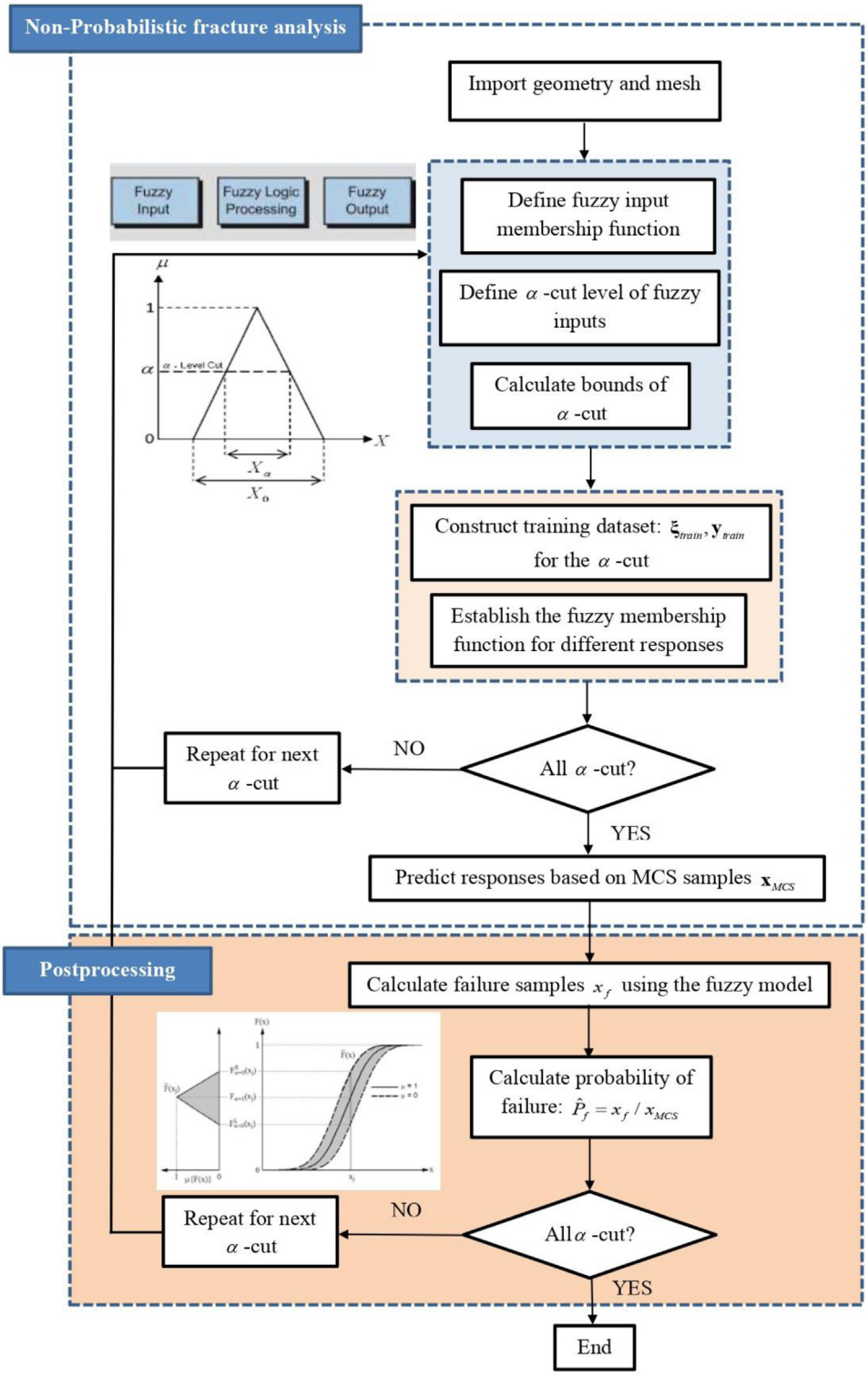

Fig. 17. A flowchart of fuzzy based non-probabilistic fracture analysis framework.

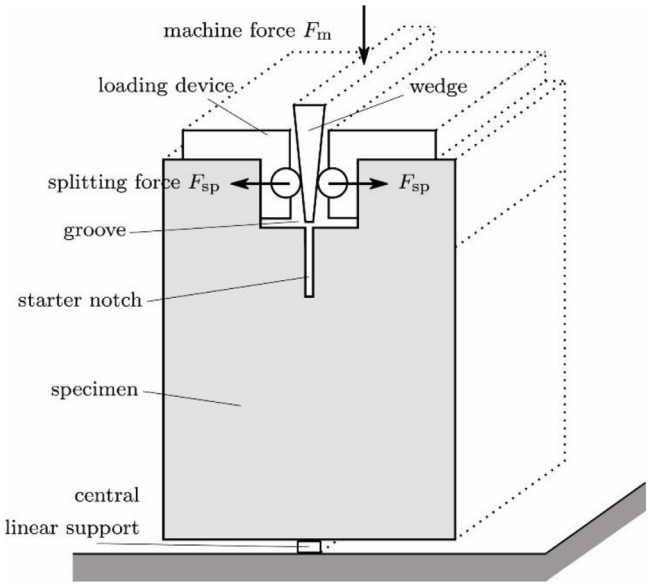

Fig. 18. Experimental setup of the classical wedge splitting test [217].

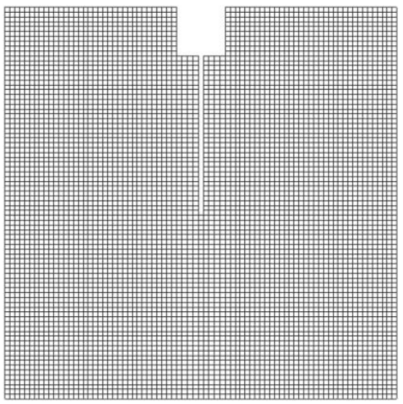

Fig. 19. FEM mesh for the wedge splitting test.

6.2. Non-deterministic fracture analysis

In this section, the non-deterministic fracture analysis by utilizing the probabilistic and non-probabilistic solutions are presented. In detail, the probabilistic fracture analysis, non-probabilistic fracture analysis and machine learning aided fracture analysis against different scenarios are carried out in the following subsections.

6.2.1. Probabilistic fracture analysis

In this sub-section, a numerical case corresponding to the probabilistic theory-based fracture analysis is presented. The descriptions of the probability distribution of various input parameters are adopted herein. In the first numerical example, the stochastic brittle fracture analysis of a fibre reinforced gear teeth is investigated, and the geometry is shown in Fig. 21. Plane stress has been used for the structure with an initial edge notch exists at the slot of the composite gear teeth. The matrix and reinforcement components of the gear teeth are made of aluminium and ceramic (SiC), respectively. For the boundary conditions of the composite gear teeth, the nodes on the boundary of the inner diameter circle and the two sides adjacent to the inner diameter circle are fixed at both x and y axes. The displacement P in positive x-axis is uniformly applied on the left side of the middle teeth as shown in Fig. 21. To

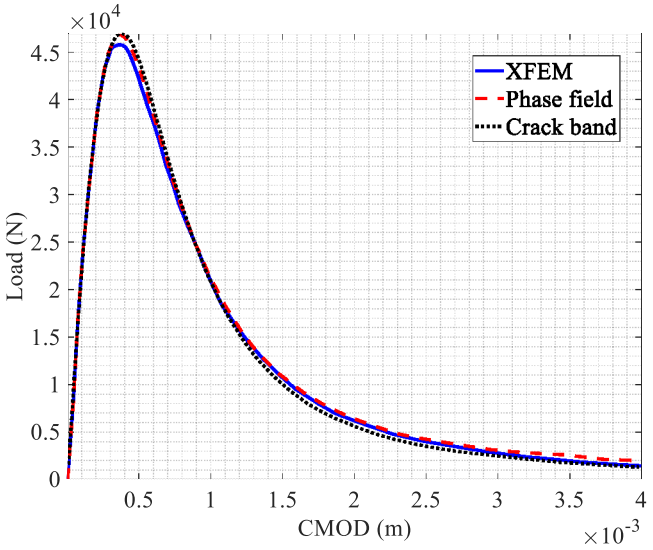

Fig. 20. The load–CMOD curves for the wedge splitting test from three methods [217–219].

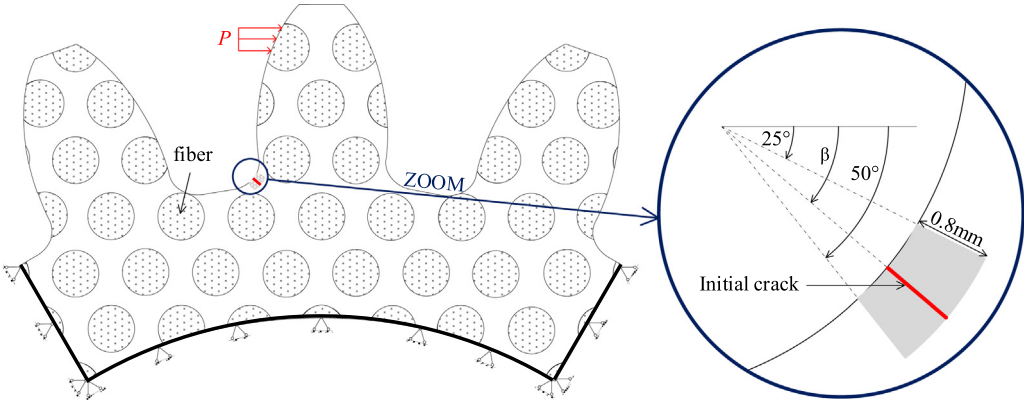

Fig. 21. Numerical example 1: gear tooth geometry.

precisely capture the crack propagation path, the area where the initial crack may propagate through the stochastic loading process has been refined as shown in Fig. 22. In addition, the displacement-control loading scheme is designed with each step of 0.005 mm.

For the information of the uncertainty parameters, various random variables with different distribution types are considered for the matrix component, the reinforcement component and the location of initial edge notch. The statistical information of the random variables is listed in Table 2. In this example, the horizontal critical load P_{cr} shown in Fig. 23(a) is the maximum tolerable applied load in the horizontal direction during the whole displacement loading process, and the corresponding applied displacement U_{cr} were observed and recorded.

In this case, the crude MCS method is adopted to quantify all the probability distributions of input variables. The random load–displacement curves of composite gear teeth calculated by the 1000 full-scale MCS simulations are presented in Fig. 23(a) and the deterministic solution is also provided. Additionally, the probabilistic damage region of the tooth is drawn in Fig. 23(b) and the random distributed crack paths are captured. The phenomenon is observed in Fig. 23(b): although the propagation path of the crack varies, the crack always propagates along the interface between the fibre circle and the matrix material rather than penetrating into the fibre component, which is necessary to further reinforce the interface region.

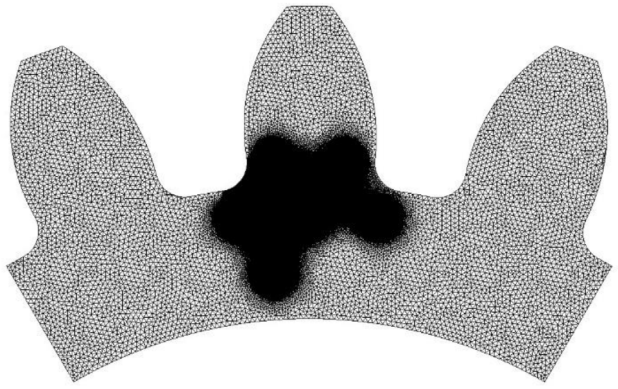

Fig. 22. Adopted FEM mesh for the composite gear tooth.

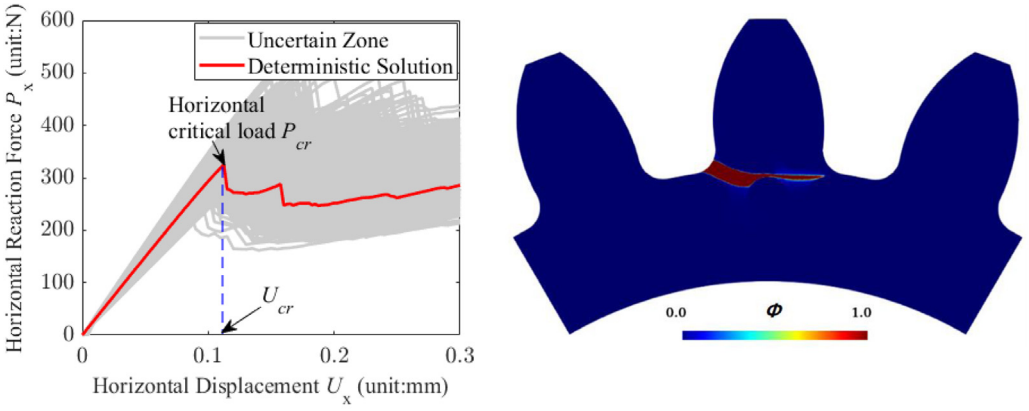

Fig. 23. (a) Schematic of horizontal critical load P_{cr} and U_{cr} within the load–displacement curves; (b) Probability-damage-interval of initial crack.

Table 2
Variational input data of composite gear teeth.

Random variables		Distribution type	Mean	Standard deviation
Matrixmaterial	E (GPa)	Lognormal	70	7
	ν	Beta	0.33	0.0066
	K_{Ic} (MPa m$^{1/2}$)	Lognormal	20	2
Reinforcement material	E (GPa)	Lognormal	120	12
	ν	Beta	0.36	0.0072
	K_{Ic} (MPa m$^{1/2}$)	Lognormal	110	11
Slope of initial crack (β)		Uniform	[25°,50°]	
l_0 (mm)		Normal	0.012	0.0006

In Table 3, the statistical characteristics of the horizontal critical load P_{cr} and the corresponding displacement U_{cr} calculated through the MCS approach are listed. From this table, the mean values of P_{cr} and U_{cr} are 387.7645 N and 0.1368 mm, respectively. The standard deviations of the two parameters are 43.2339 and 0.0166.

Additionally, the PDFs, CDFs of P_{cr} and U_{cr} calculated from the MCS approach were presented in Figs. 24 and 25. From these figures, the probability information of the structural fracture strength and deflection capacities are

Table 3
The calculated information of P_{cr} and U_{cr} of composite gear teeth.

Moments	Methods	P_{cr} N	U_{cr} mm
Mean	MCS	387.7645	0.1368
Stand deviation	MCS	43.2339	0.0166
Skewness	MCS	0.0580	0.1732
Kurtosis	MCS	2.8417	2.8542

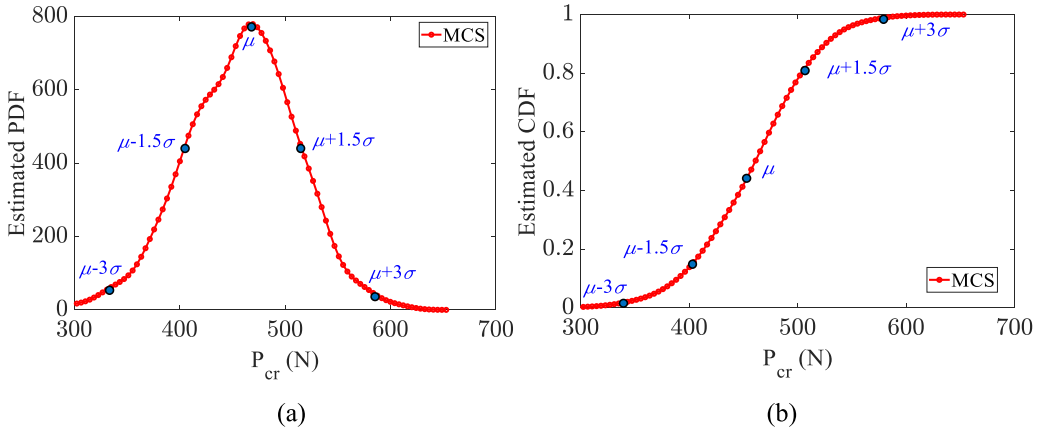

Fig. 24. (a) The estimated PDF; (b) CDF of P_{cr} in composite gear teeth.

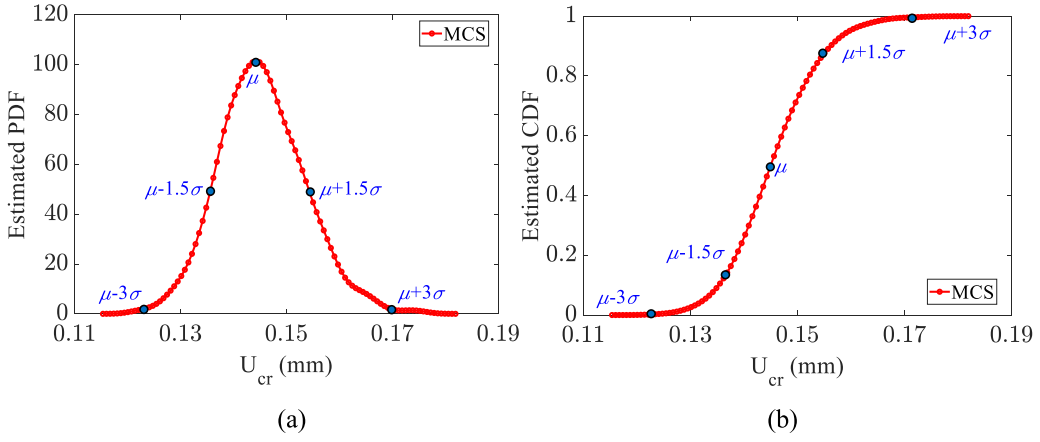

Fig. 25. (a)The estimated PDF; (b) CDF of U_{cr} in composite gear teeth.

presented. That is, under arbitrary response level, the corresponding confidence level or the safety evaluation of the structure can be directly approximated. Consequently, the crude MCS approach provides the probabilistic brittle fracture analysis for the composite gear teeth within a unified computational framework.

For quantifying the performance of the probabilistic model, the predicted reliability of P_{cr} located at 5 positions (e.g., $\mu_{P_{cr}}^{MCS} - 3\sigma_{P_{cr}}^{MCS}$, $\mu_{P_{cr}}^{MCS} - 1.5\sigma_{P_{cr}}^{MCS}$, $\mu_{P_{cr}}^{MCS}$, $\mu_{P_{cr}}^{MCS} + 1.5\sigma_{P_{cr}}^{MCS}$, $\mu_{P_{cr}}^{MCS} + 3\sigma_{P_{cr}}^{MCS}$ where $\mu_{P_{cr}}^{MCS}$ and $\sigma_{P_{cr}}^{MCS}$ are the mean and standard deviation of P_{cr} obtained from the MCS results) were investigated and the details are listed in Table 4. From this table, the different confidence levels of the structure are estimated at different locations. Additionally, the propagation paths of the crack at five different loading locations listed in Table 4 are also depicted

Table 4
Estimated probability of P_{cr} at different locations in composite gear teeth.

Methods	Probability at different locations				
	$\mu_{P_{cr}}^{MCS} - 3\sigma_{P_{cr}}^{MCS}$	$\mu_{P_{cr}}^{MCS} - 1.5\sigma_{P_{cr}}^{MCS}$	$\mu_{P_{cr}}^{MCS}$	$\mu_{P_{cr}}^{MCS} + 1.5\sigma_{P_{cr}}^{MCS}$	$\mu_{P_{cr}}^{MCS} + 3\sigma_{P_{cr}}^{MCS}$
MCS	0.001782	0.07121	0.5028	0.9275	0.9980

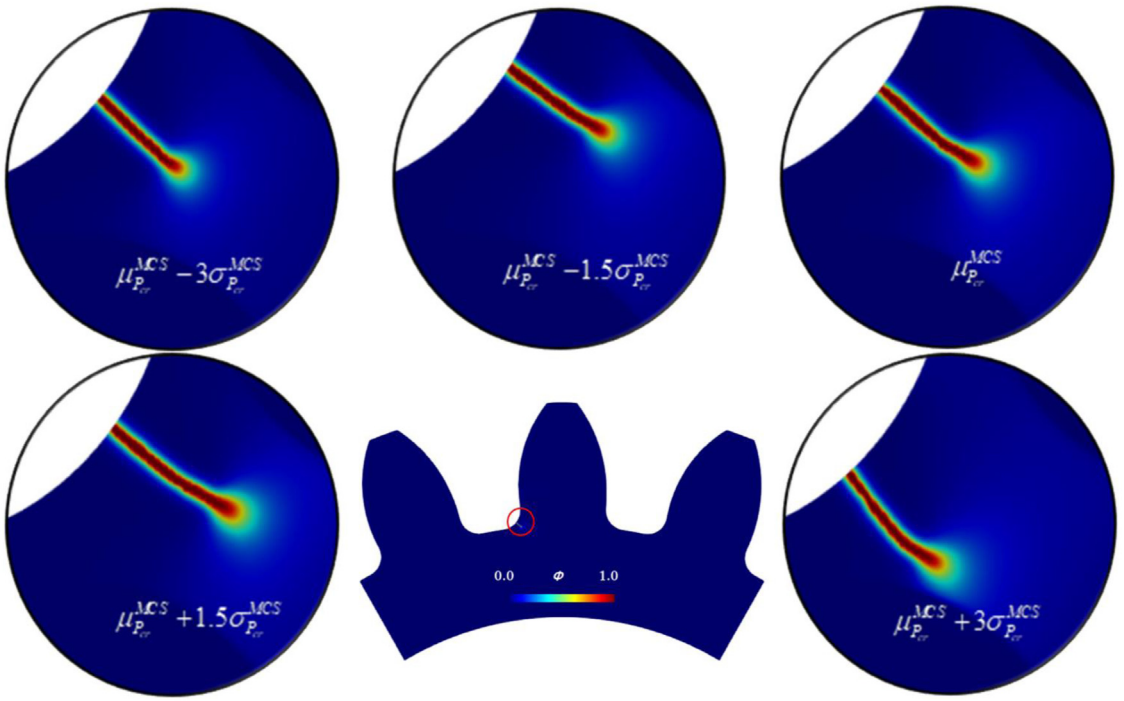

Fig. 26. Schematics of fracture propagation for the composite gear teeth at different loading locations.

in Fig. 26. These figures clearly present the variations of the crack propagation paths with the uncertain input parameters during the critical loading stage of the composite gear teeth.

6.2.2. Non-probabilistic interval fracture analysis

In this sub-section, a numerical case corresponding to the non-probabilistic theory-based interval crack band analysis for fatigue fracture prediction is introduced from Ref. [221]. In Ref. [221], a 3D mechanical gear model was considered with fatigue fracture growth to determine the tolerance evaluation and inspection period for maintaining the safety condition of gear in various significant equipment.

The gear model is shown in Fig. 27, with a radius of 72 mm and thickness of 26 mm. One tooth of the gear is subject to a cyclic line loading p and there is an initial round crack with radius of a_0 near the tooth. The FE model is constructed by 93994 C3D10 elements in Abaqus software and the material type of gear is made of 16MnCr5 steel. Considering in real-life applications, precise distribution functions of system parameters are difficult to acquire, in this research, the authors propose an interval analysis technique to estimate the upper and lower bound of fatigue fracture growth with uncertainties. For the gear model, the line loading p, initial crack length a_0, fracture propagation rate constants C and m with correlation variable of 0.8, fracture toughness K_{IC} are handled as interval parameters for different modes of crack band theory. The detailed upper and lower bounds information of the uncertain parameters is listed in Table 5.

For the deterministic fracture analysis, the crack growth path and the stress intensity factor (SIF) under different crack length is presented in Fig. 28. Based on the crack path, the fracture mode of the gear is mode I. After considering all the randomness into the deterministic model, an interval prediction model can be constructed for

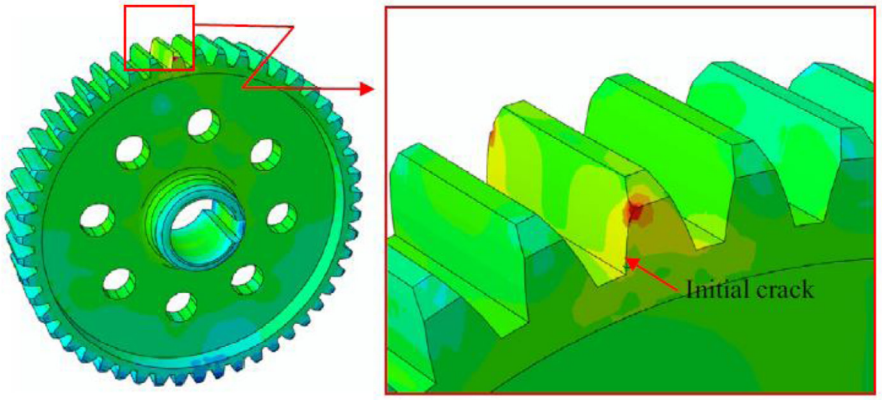

Fig. 27. Numerical example 2: gear tooth geometry and initial crack [221].

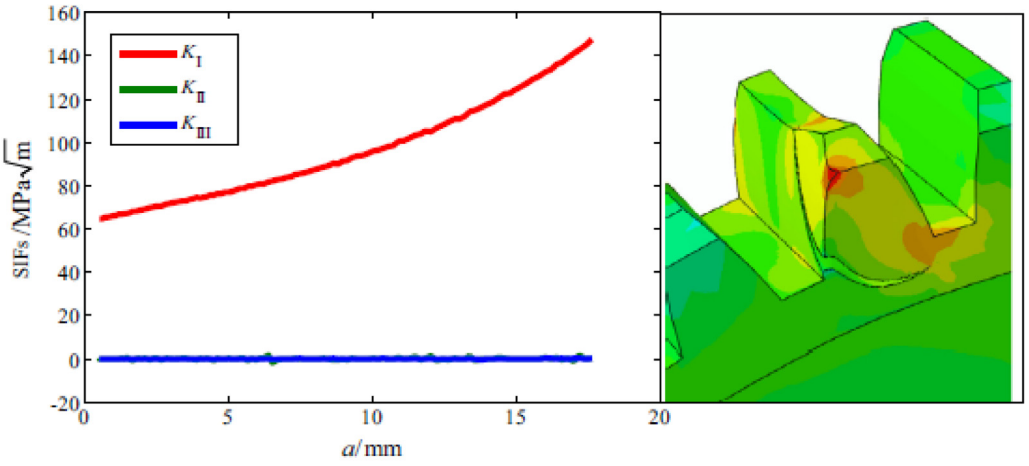

Fig. 28. (a) The SIFs along the crack length and (b) the crack growth path [221].

Table 5
Variational input data of gear structure [221].

Variational inputs	Interval	Random level
p (kN)	$[3-3\alpha, 3+3\alpha]$	$\alpha = 1\%, \ldots, 20\%$
a_0 (mm)	[0.4, 0.6]	20.0%
C	[2.65e−9, 8.75e−9]	53.5%
m	[2.6, 3.4]	13.3%
K_{IC} (MPa$\sqrt{\text{m}}$)	[135, 165]	10.0%

estimating the potential fatigue crack growth life. In Fig. 29, the upper and lower bounds of the fatigue crack growth life with interval level of the line loading p from 1% to 20% are presented and well compared with the MCS results to illustrate the accuracy. The two results are very close under different interval levels. From the results, the overall upper bound of fatigue crack growth life is 1.60e6 cycles, lower bound is 1.29e5 cycles under interval level of 20%. Therefore, to make sure the safety of the gear structure, the corresponding inspection period of gear should be set no more than lower bound of 1.29e5 cycles in prior to the fracture failure happens to the gear. A potential disadvantage of this approach, however, is that the bounds of fatigue crack growth life may be too broad for effective decision, and basing a decision on the lower bound may be overly conservative.

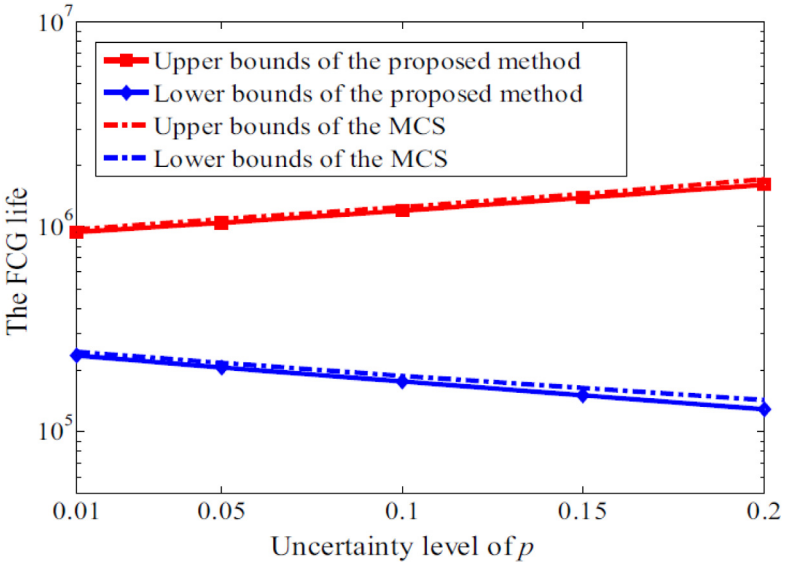

Fig. 29. The interval of fatigue crack growth life of gear under different random levels of load p [221].

6.2.3. Machine learning aided non-deterministic fracture analysis

In this sub-section, the numerical framework corresponding to the machine learning aided non-deterministic fracture analysis is introduced. The construction of different surrogate models based on the machine learning algorithms are presented then compared with each other with the same numerical case. Subsequently, a fuzzy-based stochastic fracture analyses by using the Ada-X-SVR method are provided in the subsequent case.

6.2.3.1. Design of experiments. Before the construction of the different surrogate models, one significant step is to determine the appropriate data sample size for training, which is also known as the design of experiments (DoE) process [222]. For generating random samples, normally the Sobol's sequence sampling method or Latin Hypercube sampling method is adopted [214,215], for instance, determine n system random variables and generate m realizations for each random variable through the sampling method with $\mathbf{x}_{train} := \{\mathbf{x}_i \in \Re^n,\ for\ i = 1, \ldots, m\}$, where m is the size of the training dataset, $\mathbf{x}_i$ is the ith realization, and $\mathbf{x}_{train} \in \Re^{m \times n}$ is the generated training dataset including all realizations.

The training sample size of the surrogate model is determined through a convergence study with relevant mathematical quantification measures (i.e., R-square, root mean square error (RMSE), relative error (RE)), normally with the increasement of 100 to 500 training samples could improve the mathematical figures significantly. Furthermore, for constructing a reference database to verify the accuracy of surrogate model, the total sample size by using the classical MCS method is expected to be large (i.e., $10^3 \sim 10^6$, depending on individual case), such that the prediction results can be thoroughly validated.

6.2.3.2. Concrete plate with holes. In this example, the random crack propagation of a typical concrete plate with holes is predicted and validated with experimental results in [139]. The geometry and boundary conditions of the concrete plate are shown in Fig. 30(a), and a plane stress condition is considered for the structure. An initial crack is observed at left hand of plate and the lower hole is fixed, and a continuous displacement is applied at the upper hole. The FE model is constructed in Abaqus software with 24 701 nodes as shown in Fig. 30(b).

For the deterministic fracture response, in this case, both the phase field method and the XFEM method are adopted. The corresponding numerical simulation results are compared with the experimental record in Fig. 31. It can be seen that the crack path differs significantly for the two methods and phase field method simulates well with the experimental observations. In detail, phase field model predicts a significant secondary developed crack on the other side of the hole. However, the XFEM method does not possess an intrinsic functionality to nucleate cracks without predefinition. Once the crack tip has propagated near the hole, the algorithm of the XFEM method terminates. This drawback may result in the omission of many potential defects by using the traditional models,

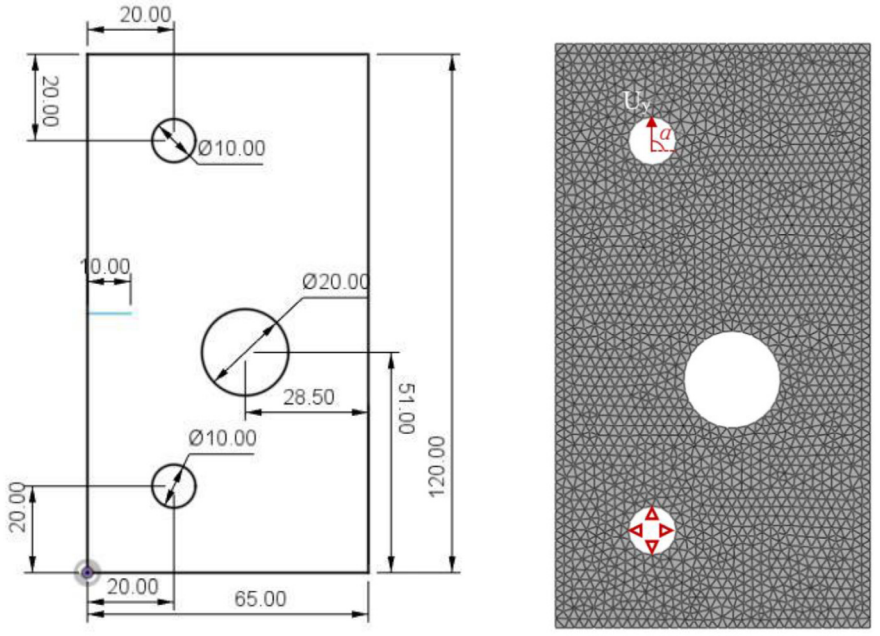

Fig. 30. (a) Experimental example 3: Notched plate geometry; (b) Adopted FEM mesh for the notched plate.

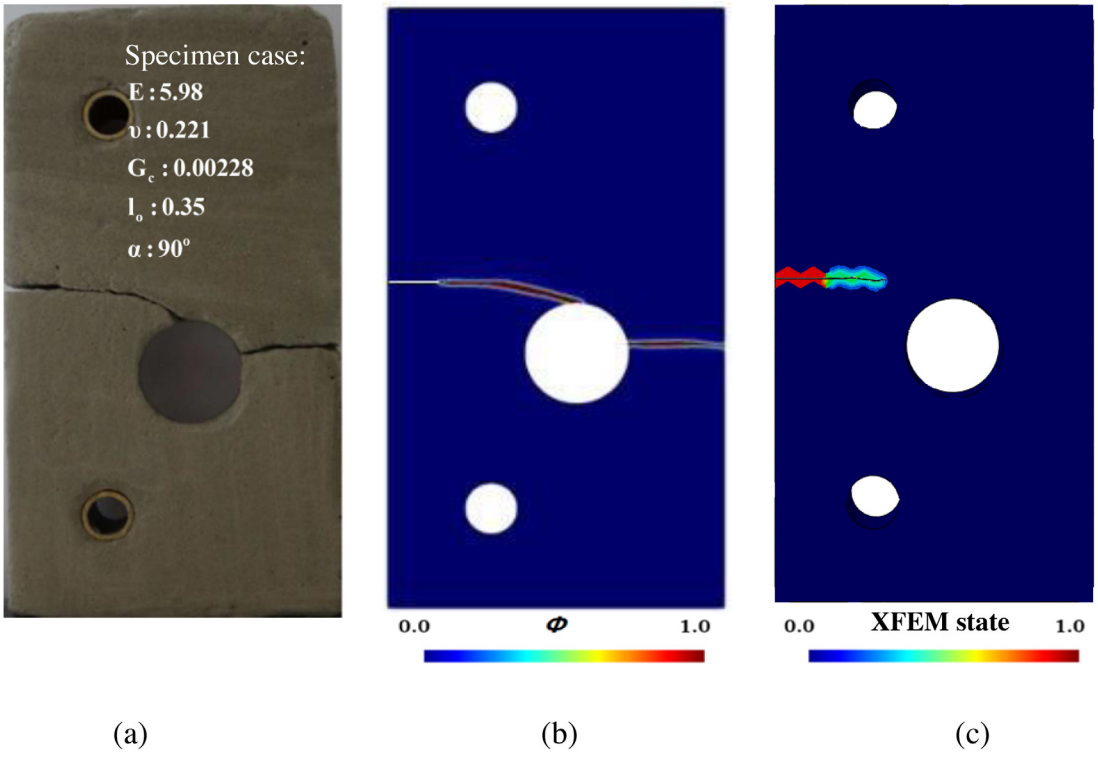

Fig. 31. (a) Experimental observation of fractured specimen; (b) Predicted crack path by the phase field method; (c) The crack path by the XFEM method.

Table 6
Variational input data of notched plate with hole.

Random variables	Distribution type	Mean	Standard deviation
E (GPa)	Lognormal	5.98	0.299
υ	Uniform	[0.21, 0.23]	
G_c (kN/mm)	Beta	0.00228	0.000114
l_0 (mm)	Normal	0.35	0.0175
α (°)	Uniform	[87.5°, 92.5°]	

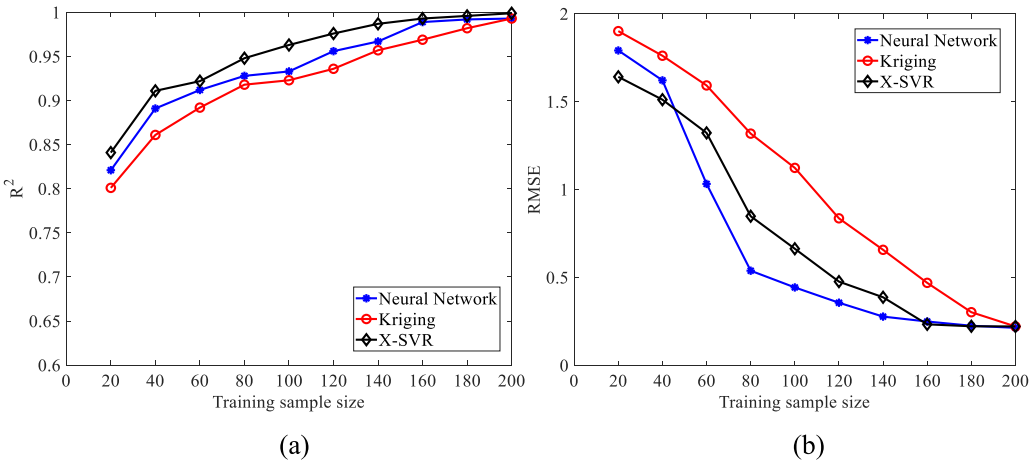

Fig. 32. Estimation results of (a) R^2, and (b) RMSE of P_{cr} from the neural network, Kriging, and X-SVR approaches.

which might bring failures to the engineering applications. Therefore, this case just uses the phase field method to simulate crack propagation path.

Subsequently, for constructing the surrogate models with different machine learning algorithms (i.e., neural network, Kriging, X-SVR), a variational input dataset including the Young's modulus E, Poisson's ratio υ, fracture toughness G_c, length scale parameter l_0 and loading angle α is listed in Table 6. In the same time, the crude MCS result with 1000 simulation cycles is implemented as reference results.

Again, by collecting P_{cr} in the load–displacement curves, the convergence study of the R^2 and the *RMSE* through the neural network (NN), Kriging and X-SVR models with different training sample sizes are performed in Fig. 32. From Fig. 32, different convergence behaviours are seen for three techniques with the accumulation of training sample size. For unified purposes, the final training sample size is determined as 200 for three models.

To illustrate the different performances of three surrogate models, the critical loads P_{cr} during the crack propagation process are predicted by three models for the concrete plate. By using a data training size of 200, the predicted statistical moments (i.e., mean, standard deviation, skewness, kurtosis) of P_{cr} by three approaches have been presented in Table 7. Also, predictions of the statistical moments of the concerned structural responses through MCS method with 1000 simulations are reported in Table 7.

From Table 7, the detailed statistical results of the critical capacity load from all approaches are demonstrated. The maximum absolute relative errors are 3.7%, 7.4%, and 3.7% for three different surrogate models, respectively. The corresponding computational costs of each method are also listed, and it should be noticed that compared with the crude MCS method, the required computational time of the surrogate models are significantly lower. Such that, a great deal of computational cost can be saved by using machine learning aided techniques.

Moreover, the subsequent PDFs, CDFs and the REs of the PDFs, CDFs of P_{cr} by using three surrogate models are shown in Fig. 33(a)–(d). From the figures, the reliability profiles of PDF and CDF by three surrogate models simulate well with the MCS results and the relative errors are all acceptable at different locations. Consequently, the accuracy, efficiency and applicability of the machine learning aided non-deterministic fracture analysis are demonstrated for the concrete plate example presented herein.

Table 7
Estimated statistical moments of P_{cr} of the notched plate.

Statistics	MCS	Neural network	Relative error (%)	Kriging	Relative error (%)	X-SVR	Relative error (%)
Mean (kN)	580.31	580.38	0.0121	580.42	0.0190	580.35	0.007
Standard deviation	1.673	1.679	0.359	1.683	0.598	1.678	0.299
Skewness	0.136	0.141	3.676	0.146	7.353	0.141	3.676
Kurtosis	1.082	1.097	1.386	1.103	1.941	1.092	0.924
Computational cost (h)	229.5	41.6		53.7		44.5	

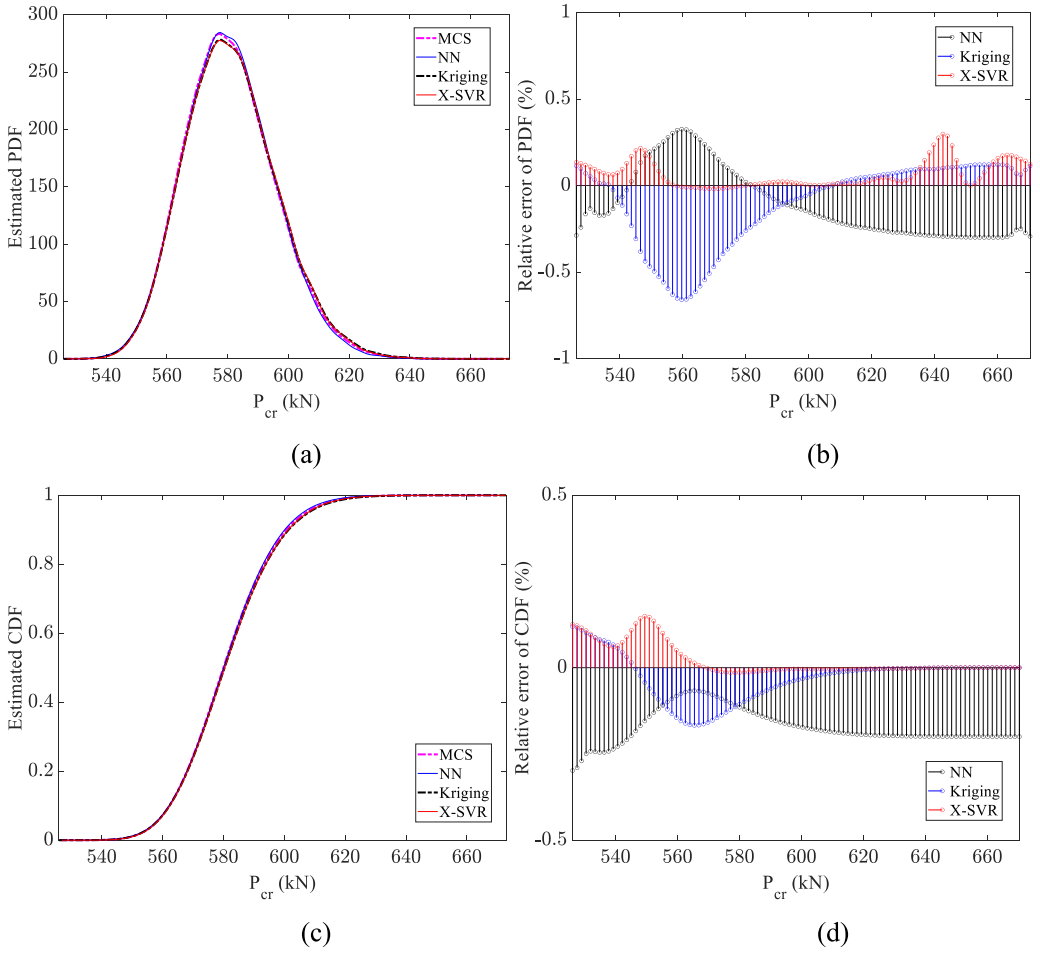

Fig. 33. Predicted (a) PDF, (b) CDF, (c) REs of PDF, and (d) REs of CDF of P_{cr} for three different material models.

6.2.3.3. Notched beam under three-point bending. For the last numerical case, the three-dimensional notched beam under three-point bending is considered with fuzzy random parameters. The concrete beam is made with quasi-brittle properties and relevant experimental test was implemented in Ref. [38,223]. The geometry and boundary conditions of the notched beam are shown in Fig. 34(a), and a line displacement loading of $u = 1$ mm is applied on the middle top of the beam. The FE model of beam is established by Abaqus software and a total of 24 083 node points are used to mesh and refine the potential crack region as shown in Fig. 34(b). Once again, the critical capacity load P_{cr} is recorded within the load–displacement curve.

For the deterministic fracture analysis of notched beam, the determined material properties of beam is set as $E = 20\,\text{GPa}$, $\upsilon = 0.2$, $G_c = 0.113\,\text{N/mm}$ and $l_0 = 2.5\,\text{mm}$, then the phase field simulation result is compared with the experimental records in Ref. [38,223] in Fig. 35(a)–(d). From Fig. 35(c), the load–displacement curve

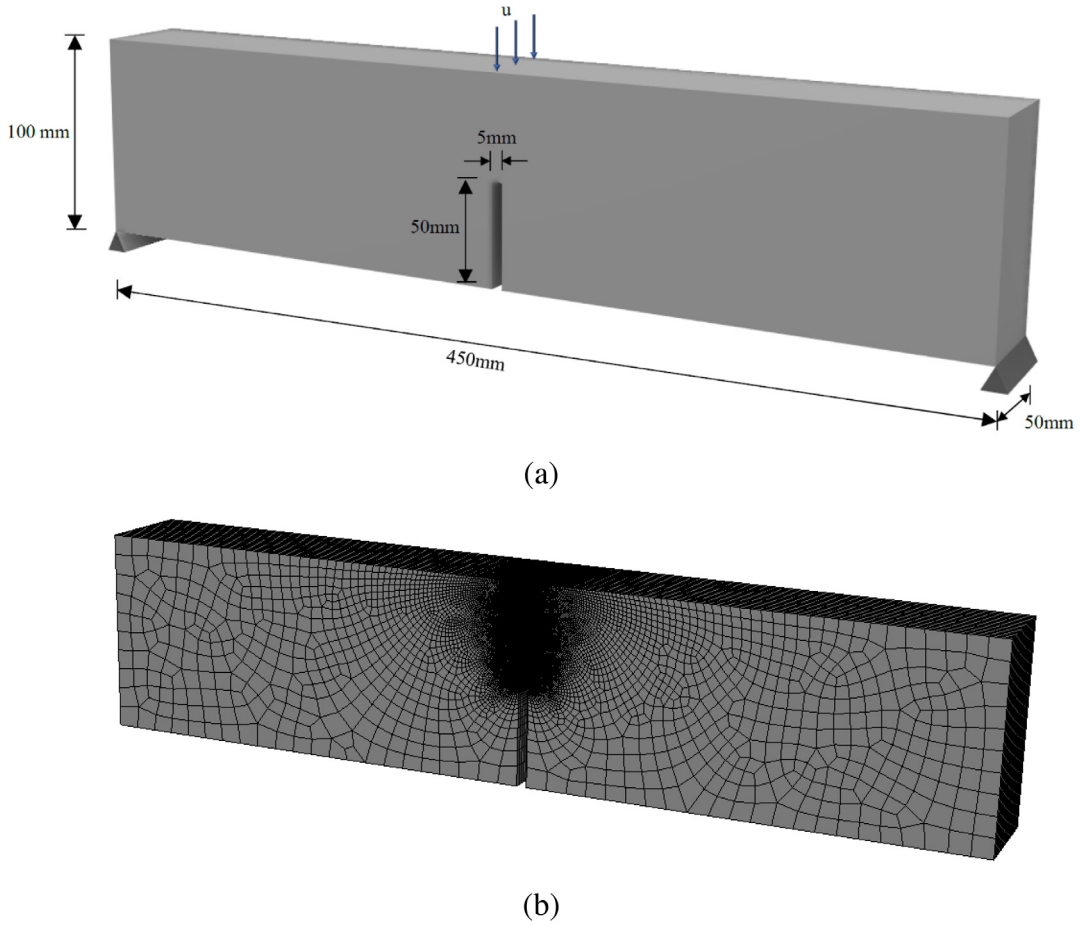

Fig. 34. (a) Experimental example 4: 3D notched beam geometry; (b) Adopted FEM mesh for the notched beam.

calculated by phase field method is compared with the experimental result. Both the critical loading and the deflection at that location corroborate well with two methods, and Fig. 35(d) shows the relative error between the two results. Therefore, the simulation result obtained from phase field method is reliable for making further uncertainty quantification analysis and in this case, a modified X-SVR technique, namely the Ada-X-SVR is used with higher computational performance. Interested readers can find detailed formulations in Ref. [224].

In this case, a variational input dataset including the Young's modulus E, Poisson's ratio υ, fracture toughness G_c, and length scale parameter l_0 are considered with polymorphic uncertainties which consider fuzzy and random uncertainty simultaneously [224], and the fuzzy membership functions of parameters are listed in Table 8. Also the crude MCS method is used as a reference to validate the surrogate model. By collecting P_{cr} in the load–displacement curves, the design of experiment process with R^2 and *RMSE* through the surrogate model under various training sample sizes are implemented in Fig. 36. Observed from the evident trend of accuracy improvement with the training sample size, the sample size is selected as $\mathrm{N}_{train} = 200$ for the structure.

By using the established surrogate model, a further reliability analysis can be presented. In Fig. 37, the predicted PDF and CDF of P_{cr} by the Ada-X-SVR model are almost overlapped with the MCS results, also similar conclusions can be drawn in subplots in Fig. 37. The accuracy of the established surrogate model is once again verified. Moreover, in comparison with the MCS results, the CDFs of P_{cr} at the membership level α of 0 are predicted by the proposed technique. In here, the target level of critical boundary of loading is $\left\{P_{\mathrm{cr}}^{*} \middle| P\left(P_{\mathrm{cr}} \leq P_{\mathrm{cr}}^{*}\right) = 0.6\right\}$. Subsequently, the PDF and CDF of P_{cr}^{*} by both methods are predicted in the subplots of Fig. 38(a). Besides, the relative error of two results at different prediction locations are presented in Fig. 38(b). In Fig. 38(a), the proposed surrogate model is competent to predict the CDFs of P_{cr} at fuzzy level α of 0. The estimation results corroborate

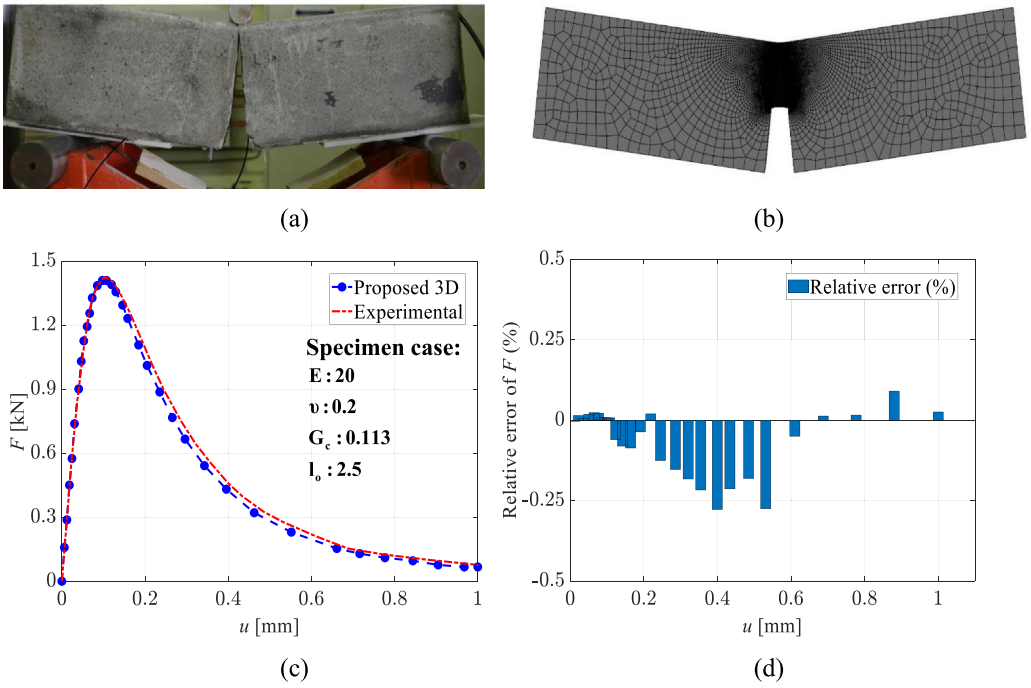

Fig. 35. (a) Experimental, (b) Predicted final deformation of specimen; (c) Predicted and experimental load–displacement curves; (d) The relative error of predicted curve.

Table 8
Polymorphic input data of the notched beam.

Property	Distribution	Parameter	Membership function	
E (GPa)	Logistic	μ_E	Trapezoid	Support of [19.7, 20.3] Core of [19.9, 20.1]
		σ_E	Triangular	Support of [0.07, 0.08] Core of 0.075
ν	Lognormal	μ_ν	Trapezoid	Support of [0.197, 0.203] Core of [0.199, 0.201]
		σ_ν	Triangular	Support of [1.7e−3, 1.9e−3] Core of 1.8e−3
l_0 (mm)	Normal	μ_{l_0}	Gaussian	Mean of 2.5 Std of 3e−3
		σ_{l_0}	Triangular	Support of [8e−3, 9e-3] Core of 8.5e−3
G_c (N/mm)	Lognormal	μ_{G_c}	Triangular	Support of [0.112, 0.114] Core of 0.113
		σ_{G_c}	Triangular	Support of [5e−4, 5.5e−4] Core of 5.25e−4

well with the MCS results but in an efficient manner. Moreover, considering the subplots in Fig. 38(a), the predicted PDF and CDF of P_{cr}^* by the surrogate model are simulated well with the reference. Also, for the relative error in Fig. 38(b), the absolute maximum relative error between the two results are acceptable with satisfied accuracy.

The calculated surrogate model has been proven accurate with various tests. Then, the predicted fuzzy-valued CDF over α and CDFs of lower bound and upper bound for P_{cr} with different assumed membership levels have been shown in Fig. 39(a) and (b).

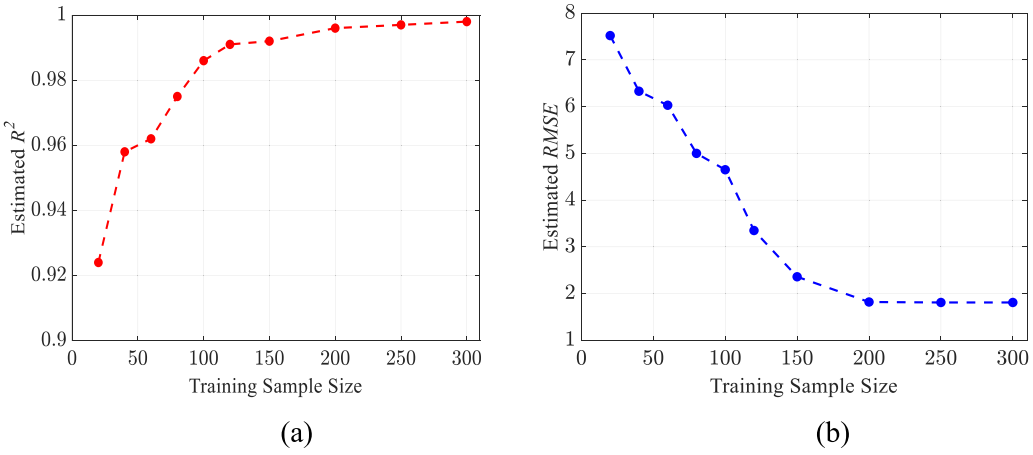

Fig. 36. The estimated (a) R^2 and (b) $RMSE$ of P_{cr} with different training sample size.

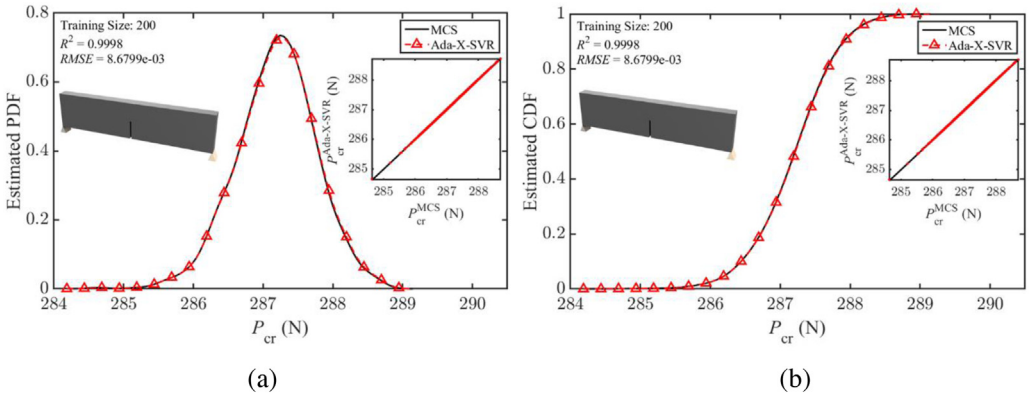

Fig. 37. The estimated (a) PDF and (b) CDF of P_{cr} under the purely stochastic problem [224].

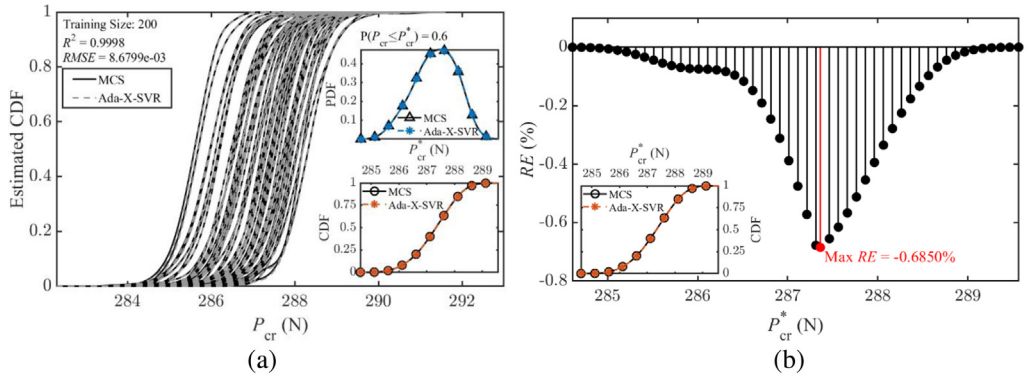

Fig. 38. The estimated (a) CDFs of P_{cr} at α of 0 and (b) RE of CDF of P^*_{cr} [224].

By using the established fuzzy-based surrogate model, a great deal of computational efforts can be saved without running repetitive FE simulations. As shown in Fig. 39(a), the fuzzy-valued CDF of P_{cr} is efficiently estimated through the proposed surrogate model. With the increasement of membership function level α, the distance for the two separate CDF surfaces would gradually narrow just as listed in Fig. 39(b). With no need to running repetitive FE

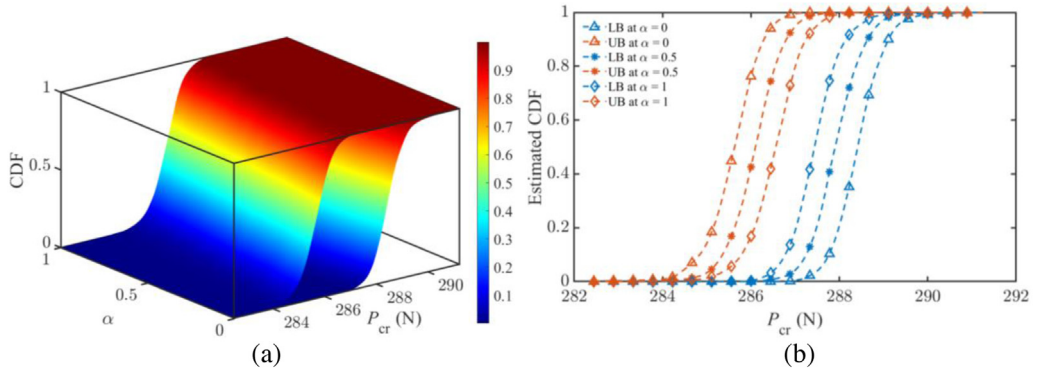

Fig. 39. The estimated (a) fuzzy-valued CDF and (b) CDFs of bounds of P_{cr} at α of 0, 0.5, and 1 [224].

Table 9
New arbitrary inputs of material properties [76].

Material properties	Updated values Case 1	Updated values Case 2	Updated values Case 3
E (GPa)	20.24	19.23	25.14
υ	0.21	0.22	0.33
l_0 (mm)	2.3	2.9	2.6
G_c (N/mm)	0.125	0.143	0.153

simulations, the CDFs at different membership function levels of α are presented to illustrate the fuzzy variations. Consequently, the fuzzy analysis based machine learning aided non-deterministic fracture analysis framework is also demonstrated effective and efficient for this fracture application where variability of inputs and outputs is relatively low.

After establishing the surrogate model, the potential fracture response can be predicted directly from the new input samples without the need of re-running the finite element model. Herein, three random new cases of inputs are generated as listed in Table 9. By implementing the new inputs into the surrogate model, the crack propagation paths can be predicted by X-SVR approach in Figs. 40–42, also the predicted relative errors between the surrogate models and deterministic finite element models are provided [76].

From the predicted crack propagation paths and the relative errors of the estimated phase field values at different nodal locations, the accuracy and stability of the machine learning aided phase field method has been reinforced by several examples. In the real-life engineering applications, the variations of system properties are difficult to control. Consequently, the ability of modern engineering system to quickly respond to the forecasted input information matters significantly, and the machine learning aided non-deterministic fracture analysis framework can be important in predicting future critical fracture-related mechanisms.

7. Remarks and outlook

In this paper, the influence of the randomness/uncertainty involved within the brittle and quasi-brittle fracture responses of different damaged structures are reviewed, which have been investigated by using the traditional probabilistic, non-probabilistic and machine learning algorithms. Various crack simulations methods of embedded, smeared and regularized approaches are adopted and compared with experimental observations, from which the strong and weak points of each method have been illustrated. A deterministic fracture analysis is implemented to consider the performance of different crack propagation techniques, and the corresponding computational efforts required are recorded for the techniques. Then a probabilistic theory-based approach is carried out to quantify the probabilistic description of fracture responses. Subsequently, considering the insufficiency of uncertainty information in some real-life applications, a non-probabilistic theory-based approach is used to provide upper and lower bounds of fracture responses under different scenarios. However, classical uncertainty quantification approaches may be computationally expensive. although there is much recent work to minimize computational efforts. Therefore,

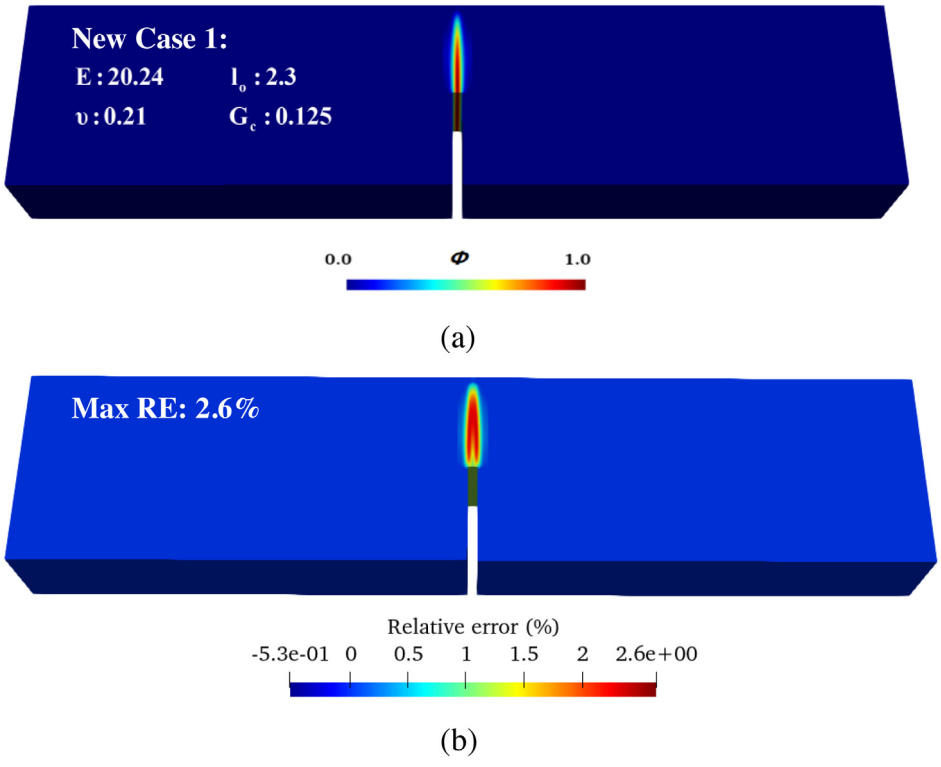

Fig. 40. (a) Predicted crack propagation; (b) Relative error of estimated phase field results at various nodes in Case 1 [76].

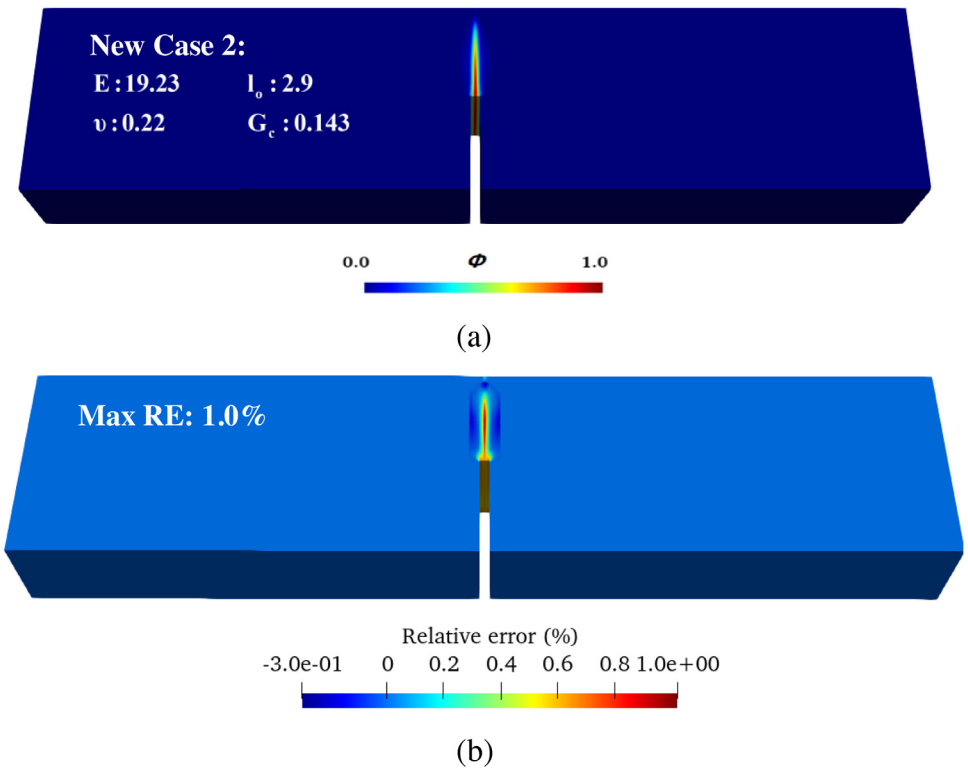

Fig. 41. (a) Predicted crack propagation; (b) Relative error of estimated phase field results at various nodes in Case 2 [76].

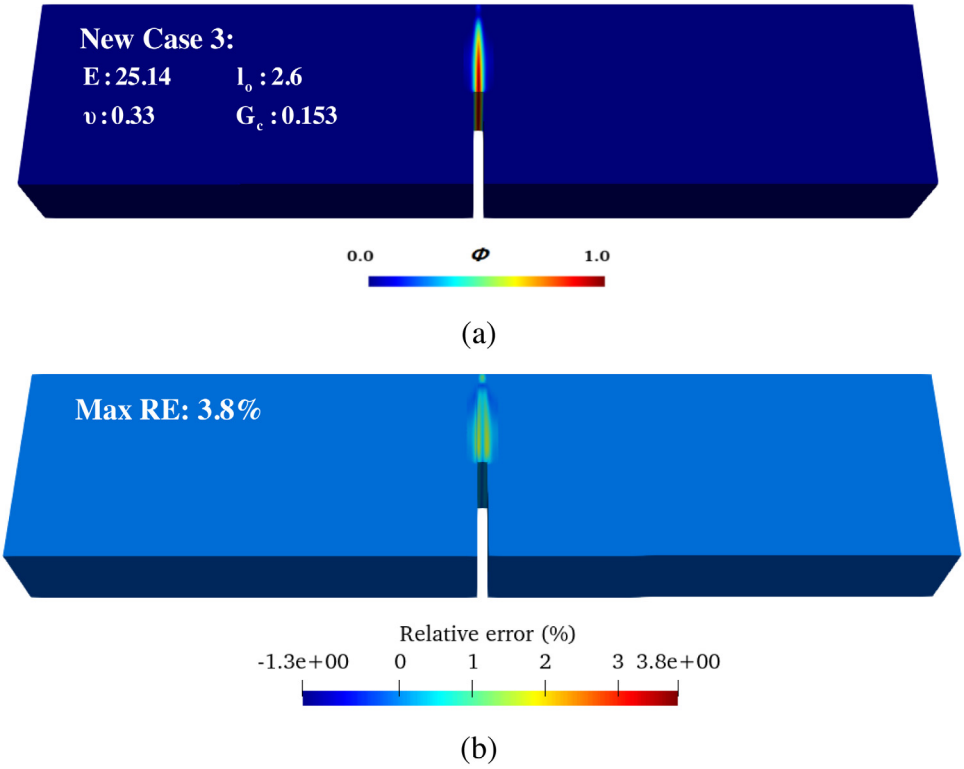

Fig. 42. (a) Predicted crack propagation; (b) Relative error of estimated phase field results at various nodes in Case 3 [76].

a recently developed non-deterministic fracture analysis system with the aid of machine learning algorithms is proposed with potential for a reduction of computational cost. Moreover, the established surrogate model by using the machine learning algorithms could analyse the correlation function between the system input parameters and fracture responses. Thus, potential crack behaviour can be predicted directly from the surrogate model without the need of running repetitive FE models. One probabilistic-based and one fuzzy-based machine learning aided fracture analysis cases are preformed to demonstrate the advantages of the proposed framework.

The extended finite element method (XFEM), the crack band method and the phase-field approach are the three most popular fracture simulation techniques for brittle or quasi-brittle structures. These computational techniques are the typical representatives of three common fracture modelling philosophies: embedded, smeared and regularized. Based on the discussion in previous sections, the appropriate evaluation of each method can be made, that is, the XFEM: crack field simulation and computationally efficient; the crack band model: generality in constitutive behaviour and fast convergence in the FE approximation; the phase field model: variational formulation in the FE setting, dynamic branching and multiple cracks. It should be noted that comparing with other two methods, the XFEM has obvious shortcomings under many conditions. In the future study of fracture mechanics, the phase field model has wide potential and popularity, but the computational efficiency issue needs to be solved more appropriately, especially for the three-dimensional fracture analysis [225,226].

This research is focused on quantifying the input randomness/uncertainty in the complicated fracture analysis of practical engineering structures, as well as the machine learning aided framework for fractural mechanism with a computationally efficient manner. This research lists and evaluates comprehensive literature of crack initiation and propagation models, as well as conventional uncertainty quantification methods with theories of both probability and non-probability, which covers the input parameters with sufficient or insufficient probabilistic descriptions. The corresponding results (probabilistic and non-probabilistic) illustrate that the uncertainties involved in the entire system indeed have a critical influence on the ultimate fracture response of structure. Therefore,

to thoroughly evaluate the safety and serviceability of practical structures under varied working environments, a robust quantification assessment characterizing the uncertainty affecting the crack responses is needed. Considering the rapid system changes in future engineering applications, the assessment efficiency is also an important point. The recently developed machine learning based non-deterministic fracture analysis system, with the capability of acquiring computational efficiency in the high cost and cumbersome process of simulating crack propagation in complicated damaged structures, would be beneficial for other future computationally demanding disciplines of engineering analyses and critical mechanics.

Declaration of competing interest

The authors declare that they have no known competing financial interests or personal relationships that could have appeared to influence the work reported in this paper.

Data availability

No data was used for the research described in the article.

Acknowledgements

The work presented in this paper is supported by the Australian Research Council projects IH200100010, DP210101353, DP230102781 and IH210100048, and the China Scholarship Council (No. 201706120056). The research work has been undertaken with the assistance of resources and services from National Computational Infrastructure (NCI) Australia.

Appendix. Formulations of vectors and matrix defined in the optimization problem

The optimization vectors and matrix of $\mathbf{P}_k$ and $\mathbf{L}_k$ are defined by:

$$\mathbf{P}_k \in \Re^{4j\times 4j} := (\hat{\mathbf{R}}_k + \mathbf{I}_{4j\times 4j})\hat{\mathbf{T}}_k^{-1}(\hat{\mathbf{R}}_k + \mathbf{I}_{4j\times 4j})^T + \hat{\mathbf{H}}_k\hat{\mathbf{e}}_k\hat{\mathbf{e}}_k^T\hat{\mathbf{H}}_k \tag{A.1}$$

$$\mathbf{L}_k \in \Re^{4j} := \gamma_2(\hat{\mathbf{R}}_k + \mathbf{I}_{4j\times 4j})\hat{\mathbf{T}}_k^{-1}\mathbf{u}_k - \lambda\hat{\mathbf{e}}_k - \hat{\mathbf{k}}_k \tag{A.2}$$

where $\hat{\mathbf{T}}_k$, $\hat{\mathbf{H}}_k$, $\hat{\mathbf{R}}_k$, $\mathbf{u}_k^T$, $\hat{\mathbf{e}}_k$, $\hat{\mathbf{k}}_k$ and $\mathbf{v}_k$ involved within the X-SVR optimization expression can be presented by:

$$\hat{\mathbf{T}}_k = \begin{bmatrix} \gamma_1\mathbf{I}_{j\times j} & & & \\ & \gamma_1\mathbf{I}_{j\times j} & & \\ & & p\mathbf{I}_{i\times i} & \\ & & & p\mathbf{I}_{i\times i} \end{bmatrix} \tag{A.3}$$

$$\hat{\mathbf{H}}_k = \begin{bmatrix} \mathbf{0}_{2j\times 2j} & \mathbf{0}_{2j\times i} & \mathbf{0}_{2j\times i} \\ \mathbf{0}_{i\times 2j} & \mathbf{I}_{i\times i} & \mathbf{0}_{i\times i} \\ \mathbf{0}_{i\times 2j} & \mathbf{0}_{i\times i} & -\mathbf{I}_{i\times i} \end{bmatrix} \tag{A.4}$$

$$\hat{\mathbf{R}}_k = \begin{bmatrix} \mathbf{0}_{2j\times j} & \mathbf{0}_{2j\times j} & \mathbf{0}_{2j\times 2i} \\ -\mathbf{x}_{train} & \mathbf{x}_{train} & \mathbf{0}_{i\times 2i} \\ \mathbf{x}_{train} & -\mathbf{x}_{train} & \mathbf{0}_{i\times 2i} \end{bmatrix} \tag{A.5}$$

$$\mathbf{u}_k = \begin{bmatrix} \mathbf{e}_j \\ \mathbf{e}_j \\ \mathbf{0}_{2i} \end{bmatrix},\ \hat{\mathbf{e}}_k = \begin{bmatrix} \mathbf{0}_{2j} \\ \mathbf{e}_i \\ \mathbf{e}_i \end{bmatrix},\ \hat{\mathbf{k}}_k = \begin{bmatrix} \mathbf{0}_{2j} \\ \mathbf{y}_{train} \\ -\mathbf{y}_{train} \end{bmatrix},\ \mathbf{v}_k = \begin{bmatrix} \mathbf{p}_k \\ \mathbf{q}_k \\ \vartheta \\ \hat{\vartheta} \end{bmatrix} \tag{A.6}$$

References

[1] T. Belytschko, T. Black, Elastic crack growth in finite elements with minimal remeshing, Internat. J. Numer. Methods Engrg. 45 (1999) 601–620.
[2] M. Javanbakht, M.S. Ghaedi, Phase field approach for void dynamics with interface stresses at the nanoscale, Internat. J. Engrg. Sci. 154 (2020).
[3] C. Miehe, M. Hofacker, F. Welschinger, A phase field model for rate-independent crack propagation: Robust algorithmic implementation based on operator splits, Comput. Methods Appl. Math. 199 (2010) 2765–2778.
[4] C. Miehe, F. Welschinger, M. Hofacker, Thermodynamically consistent phase-field models of fracture: Variational principles and multi-field FE implementations, Internat. J. Numer. Methods Engrg. 83 (2010) 1273–1311.
[5] M. Paggi, M. Corrado, M.A. Rodriguez, A multi-physics and multi-scale numerical approach to microcracking and power-loss in photovoltaic modules, Compos. Struct. 95 (2013) 630–638.
[6] P.R. Budarapu, R. Gracie, S.P.A. Bordas, T. Rabczuk, An adaptive multiscale method for quasi-static crack growth, Comput. Mech. 53 (2014) 1129–1148.
[7] H. Talebi, M. Silani, S.P.A. Bordas, P. Kerfriden, T. Rabczuk, A computational library for multiscale modeling of material failure, Comput. Mech. 53 (2014) 1047–1071.
[8] T. Belytschko, S. Loehnert, J.H. Song, Multiscale aggregating discontinuities: A method for circumventing loss of material stability, Internat. J. Numer. Methods Engrg. 73 (2008) 869–894.
[9] T. Strouboulis, I. Babuska, K.L. Copps, The design and analysis of the Generalized Finite Element Method, Comput. Methods Appl. Math. 181 (2000) 43–69.
[10] C.A. Duarte, O.N. Hamzeh, T.J. Liszka, W.W. Tworzydlo, A generalized finite element method for the simulation of three-dimensional dynamic crack propagation, Comput. Methods Appl. Math. 190 (2001) 2227–2262.
[11] T. Belytschko, Y.Y. Lu, L. Gu, Element-free Galerkin methods, Internat. J. Numer. Methods Engrg. 37 (1994) 229–256.
[12] W.K. Liu, S.F. Li, T. Belytschko, Moving least-square reproducing kernel methods. 1. Methodology and convergence, Comput. Methods Appl. Math. 143 (1997) 113–154.
[13] T. Belytschko, M. Fleming, Smoothing, enrichment and contact in the element-free Galerkin method, Comput. Struct. 71 (1999) 173–195.
[14] T. Rabczuk, G.S. Zi, A meshfree method based on the local partition of unity for cohesive cracks, Comput. Mech. 39 (2007) 743–760.
[15] E.T. Ooi, M.D. Iqbal, C. Birk, S. Natarajan, E.H. Ooi, C. Song, A polygon scaled boundary finite element formulation for transient coupled thermoelastic fracture problems, Eng. Fract. Mech. 240 (2020).
[16] Z.H. Zhang, C.H. Zhou, A. Saputra, Z.J. Yang, C.M. Song, Nonlocal dynamic damage modelling of quasi-brittle composites using the scaled boundary finite element method, Eng. Fract. Mech. 240 (2020).
[17] M. Shirzehhagh, A. Fakhimi, Insights on crack initiation and propagation in reinforced concrete beams, a bonded-particle approach, Eng. Struct. 244 (2021).
[18] C. Tekoglu, S. Celik, H. Duran, M. Efe, S. Baier-Stegmaier, K.L. Nielsen, The role of intermetallic particles on mode I crack propagation mechanisms in metal plates, Eng. Fract. Mech. 253 (2021).
[19] D.J. Benson, Y. Bazilevs, E. De Luycker, M.C. Hsu, M. Scott, T.J.R. Hughes, T. Belytschko, A generalized finite element formulation for arbitrary basis functions: From isogeometric analysis to XFEM, Internat. J. Numer. Methods Engrg. 83 (2010) 765–785.
[20] N. Nguyen-Thanh, N. Valizadeh, M.N. Nguyen, H. Nguyen-Xuan, X. Zhuang, P. Areias, G. Zi, Y. Bazilevs, L. De Lorenzis, T. Rabczuk, An extended isogeometric thin shell analysis based on Kirchhoff–Love theory, Comput. Methods Appl. Math. 284 (2015) 265–291.
[21] F. Zhou, J.F. Molinari, Dynamic crack propagation with cohesive elements: a methodology to address mesh dependency, Internat. J. Numer. Methods Engrg. 59 (2004) 1–24.
[22] S. Mukhopadhyay, S.R. Hallett, An augmented cohesive element for coarse meshes in delamination analysis of composites, Compos. Struct. 254 (2020).
[23] R.W. Macek, S.A. Silling, Peridynamics via finite element analysis, Finite Elem. Anal. Des. 43 (2007) 1169–1178.
[24] M. Behzadinasab, M. Alaydin, N. Trask, Y. Bazilevs, A general-purpose, inelastic, rotation-free Kirchhoff–Love shell formulation for peridynamics, Comput. Methods Appl. Math. 389 (2022).
[25] J.Y. Wu, T.K. Mandal, V.P. Nguyen, A phase-field regularized cohesive zone model for hydrogen assisted cracking, Comput. Methods Appl. Math. 358 (2020).
[26] J.Y. Wu, Y.L. Huang, V.P. Nguyen, On the BFGS monolithic algorithm for the unified phase field damage theory, Comput. Methods Appl. Math. 360 (2020).
[27] M. Cervera, G.B. Barbat, M. Chiumenti, J.Y. Wu, A comparative review of XFEM, mixed FEM and phase-field models for quasi-brittle cracking, Arch. Comput. Methods Eng. 29 (2022) 1009–1083.
[28] Z.Q. Cheng, J.J. Xiong, W. Tan, Fatigue crack growth and life prediction of 7075-T62 aluminium-alloy thin-sheets with low-velocity impact damage under block spectrum loading, Int. J. Fatigue 155 (2022).
[29] D.L. DuQuesnay, P.R. Underhill, H.J. Britt, Fatigue crack growth from corrosion damage in 7075-t6511 aluminium alloy under aircraft loading, Int. J. Fatigue 25 (2003) 371–377.
[30] E. Poursaeidi, H. Bakhtiari, Fatigue crack growth simulation in a first stage of compressor blade, Eng. Fail. Anal. 45 (2014) 314–325.
[31] S. Sakata, G. Stefanou, S. Araki, Random field modeling of local strength of a randomly arranged unidirectional fiber-reinforced composite material under transverse tensile loading, Mater. Today Commun. 33 (2022).
[32] J. Wu, C. McAuliffe, H. Waisman, G. Deodatis, Stochastic analysis of polymer composites rupture at large deformations modeled by a phase field method, Comput. Methods Appl. Math. 312 (2016) 596–634.

[33] W.T. He, J.X. Liu, D. Xie, Probabilistic life assessment on fatigue crack growth in mixed-mode by coupling of kriging model and finite element analysis, Eng. Fract. Mech. 139 (2015) 56–77.
[34] G.H. Besterfield, W.K. Liu, M.A. Lawrence, T. Belytschko, Fatigue crack-growth reliability by probabilistic finite-elements, Comput. Methods Appl. Math. 86 (1991) 297–320.
[35] J.H. Kim, C.D. Thanh, G. Zi, W.W. Lee, J.S. Kong, Probabilistic fatigue integrity assessment in multiple crack growth analysis associated with equivalent initial flaw and material variability, Eng. Fract. Mech. 156 (2016) 182–196.
[36] P.E. Leser, J.D. Hochhalter, J.E. Warner, J.A. Newman, W.P. Leser, P.A. Wawrzynek, F.G. Yuan, Probabilistic fatigue damage prognosis using surrogate models trained via three-dimensional finite element analysis, Struct. Health Monitor. Int. J. 16 (2017) 291–308.
[37] G. Stefanou, D. Savvas, M. Papadrakakis, Stochastic finite element analysis of composite structures based on material microstructure, Compos. Struct. 132 (2015) 384–392.
[38] R. De Borst, Some recent developments in computational modelling of concrete fracture, Int. J. Fract. 86 (1997) 5–36.
[39] M. Jirasek, T. Zimmermann, Analysis of rotating crack model, ASCE J. Eng. Mech. 124 (1998) 842–851.
[40] L. Chen, T. Rabczuk, S.P.A. Bordas, G.R. Liu, K.Y. Zeng, P. Kerfriden, Extended finite element method with edge-based strain smoothing (ESm-XFEM) for linear elastic crack growth, Comput. Methods Appl. Math. 209 (2012) 250–265.
[41] N. Sukumar, J.E. Dolbow, N. Moes, Extended finite element method in computational fracture mechanics: a retrospective examination, Int. J. Fract. 196 (2015) 189–206.
[42] E. Castillo, A.J. O'Connor, M. Nogal, A. Calvino, On the physical and probabilistic consistency of some engineering random models, Struct. Saf. 51 (2014) 1–12.
[43] M. Kaminski, B. Lauke, Uncertainty in effective elastic properties of particle filled polymers by the Monte-Carlo simulation, Compos. Struct. 123 (2015) 374–382.
[44] M. Tremayne, B.M. Kariuki, K.D.M. Harris, The development of Monte Carlo methods for crystal structure solution from powder diffraction data: Simultaneous translation and rotation of a structural fragment within the unit cell, J. Appl. Crystallogr. 29 (1996) 211–214.
[45] H.C. Noh, T. Park, Monte Carlo simulation-compatible stochastic field for application to expansion-based stochastic finite element method, Comput. Struct. 84 (2006) 2363–2372.
[46] J.E. Warner, M. Grigoriu, W. Aquino, Stochastic reduced order models for random vectors: Application to random eigenvalue problems, Probab. Eng. Mech. 31 (2013) 1–11.
[47] S. Adhikari, A reduced spectral function approach for the stochastic finite element analysis, Comput. Methods Appl. Math. 200 (2011) 1804–1821.
[48] E. Oja, J. Karhunen, On stochastic-approximation of the eigenvectors and eigenvalues of the expectation of a random matrix, J. Math. Anal. Appl. 106 (1985) 69–84.
[49] C.V. Verhoosel, M.A. Gutierrez, S.J. Hulshoff, Iterative solution of the random eigenvalue problem with application to spectral stochastic finite element systems, Internat. J. Numer. Methods Engrg. 68 (2006) 401–424.
[50] R. Ghanem, D. Ghosh, Efficient characterization of the random eigenvalue problem in a polynomial chaos decomposition, Internat. J. Numer. Methods Engrg. 72 (2007) 486–504.
[51] T.M. Al-shami, (2, 1)-Fuzzy sets: properties, weighted aggregated operators and their applications to multi-criteria decision-making methods, Complex Intell. Syst. (2022).
[52] L. Farkas, D. Moens, D. Vandepitte, W. Desmet, Fuzzy finite element analysis based on reanalysis technique, Struct. Saf. 32 (2010) 442–448.
[53] D. Wu, W. Gao, C. Wang, S. Tangaramvong, F. Tin-Loi, Robust fuzzy structural safety assessment using mathematical programming approach, Fuzzy Sets and Systems 293 (2016) 30–49.
[54] G.J. Li, Z.Z. Lu, J. Xu, A fuzzy reliability approach for structures based on the probability perspective, Struct. Saf. 54 (2015) 10–18.
[55] S. Adhikari, H.H. Khodaparast, A spectral approach for fuzzy uncertainty propagation in finite element analysis, Fuzzy Sets and Systems 243 (2014) 1–24.
[56] C. Jiang, X. Han, G.Y. Lu, J. Liu, Z. Zhang, Y.C. Bai, Correlation analysis of non-probabilistic convex model and corresponding structural reliability technique, Comput. Methods Appl. Math. 200 (2011) 2528–2546.
[57] C. Jiang, Q.F. Zhang, X. Han, J. Liu, D.A. Hu, Multidimensional parallelepiped model-a new type of non-probabilistic convex model for structural uncertainty analysis, Internat. J. Numer. Methods Engrg. 103 (2015) 31–59.
[58] H. Zhang, H.Z. Dai, M. Beer, W. Wang, Structural reliability analysis on the basis of small samples: An interval quasi-Monte Carlo method, Mech. Syst. Signal Process. 37 (2013) 137–151.
[59] S.H. Chen, H.D. Lian, X.W. Yang, Interval eigenvalue analysis for structures with interval parameters, Finite Elem. Anal. Des. 39 (2003) 419–431.
[60] Z.P. Qiu, X.J. Wang, Solution theorems for the standard eigenvalue problem of structures with uncertain-but-bounded parameters, J. Sound Vib. 282 (2005) 381–399.
[61] W. Gao, Interval natural frequency and mode shape analysis for truss structures with interval parameters, Finite Elem. Anal. Des. 42 (2006) 471–477.
[62] H.N. Leng, Z.Q. He, Q. Yuan, Computing bounds to real eigenvalues of real-interval matrices, Internat. J. Numer. Methods Engrg. 74 (2008) 523–530.
[63] Y. Feng, Q.H. Wang, X.J. Chen, D. Wu, W. Gao, Virtual modelling technique for geometric-material nonlinear dynamics of structures, Struct. Saf. 100 (2023).
[64] Y. Feng, Q.H. Wang, Y.G. Yu, T.Y. Zhang, D. Wu, X.J. Chen, Z. Luo, W. Gao, Experimental-numerical-virtual (ENV) modelling technique for composite structure against low velocity impacts, Eng. Struct. 278 (2023).

[65] J.N. Fuhg, C. Bohm, N. Bouklas, A. Fau, P. Wriggers, M. Marino, Model-data-driven constitutive responses: Application to a multiscale computational framework, Internat. J. Engrg. Sci. 167 (2021).
[66] S.S. Ghanbari, A.H. Mahmoudi, An improvement in data interpretation to estimate residual stresses and mechanical properties using instrumented indentation: A comparison between machine learning and Kriging model, Eng. Appl. Artif. Intell. 114 (2022).
[67] S. Manzhos, M. Ihara, Optimization of hyperparameters of Gaussian process regression with the help of a low-order high-dimensional model representation: application to a potential energy surface, J. Math. Chem. (2022).
[68] F. Aldakheel, R. Satari, P. Wriggers, Feed-forward neural networks for failure mechanics problems, Appl. Sci. Basel 11 (2021).
[69] B.P. van de Weg, L. Greve, M. Andres, T.K. Eller, B. Rosic, Neural network-based surrogate model for a bifurcating structural fracture response, Eng. Fract. Mech. 241 (2021).
[70] M. Kent, N.K. Huynh, S. Schiavon, S. Selkowitz, Using support vector machine to detect desk illuminance sensor blockage for closed-loop daylight harvesting, Energy Build. 274 (2022).
[71] L.X. Li, Q. Wang, C.L. Ke, Local support vector machine based dimension reduction, Stat. Anal. Data Min. 15 (2022) 722–735.
[72] A. Fuchs, Y. Heider, K. Wang, W.C. Sun, M. Kaliske, DNN2: A hyper-parameter reinforcement learning game for self-design of neural network based elasto-plastic constitutive descriptions, Comput. Struct. 249 (2021).
[73] S.E. Fang, S. Chen, Y.Q. Lin, Z.L. Dong, Probabilistic damage identification incorporating approximate Bayesian computation with stochastic response surface, Mech. Syst. Signal Process. 128 (2019) 229–243.
[74] K. Kasama, Z. Furukawa, L.H. Hu, Practical reliability analysis for earthquake-induced 3D landslide using stochastic response surface method, Comput. Geotech. 137 (2021).
[75] Y. Feng, Q.H. Wang, D. Wu, W. Gao, F. Tin-Loi, Stochastic nonlocal damage analysis by a machine learning approach, Comput. Methods Appl. Math. 372 (2020).
[76] Y. Feng, Q.H. Wang, D. Wu, Z. Luo, X.J. Chen, T.Y. Zhang, W. Gao, Machine learning aided phase field method for fracture mechanics, Internat. J. Engrg. Sci. 169 (2021).
[77] G.Y. Fu, G.W. Ma, X.L. Qu, D. Huang, Stochastic analysis of progressive failure of fractured rock masses containing non-persistent joint sets using key block analysis, Tunn. Undergr. Space Technol. 51 (2016) 258–269.
[78] K.M. Hamdia, M. Silani, X.Y. Zhuang, P.F. He, T. Rabczuk, Stochastic analysis of the fracture toughness of polymeric nanoparticle composites using polynomial chaos expansions, Int. J. Fract. 206 (2017) 215–227.
[79] K. Khatri, A. Lal, Stochastic XFEM based fracture behavior and crack growth analysis of a plate with a hole emanating cracks under biaxial loading, Theor. Appl. Fract. Mech. 96 (2018) 1–22.
[80] M. Ortiz, Y. Leroy, A. Needleman, A finite-element method for localized failure analysis, Comput. Methods Appl. Math. 61 (1987) 189–214.
[81] J. Oliver, A.E. Huespe, M.D.G. Pulido, E. Chaves, From continuum mechanics to fracture mechanics: the strong discontinuity approach, Eng. Fract. Mech. 69 (2002) 113–136.
[82] P.D. Hilton, L.N. Gifford, Computational fracture-mechanics - nonlinear and 3-D problems, Trans. ASME, J. Press. Vessel Technol. 106 (1984) 302–303.
[83] H. Liebowitz, J.S. Sandhu, J.D. Lee, F.C.M. Menandro, Computational fracture-mechanics - research and application, Eng. Fract. Mech. 50 (1995) 653–670.
[84] J.B. Min, J.M. Bass, L.W. Spradley, Adaptive finite-element methods for 2-dimensional problems in computational fracture-mechanics, Comput. Struct. 50 (1994) 433–445.
[85] T. Nishioka, The state-of-the-art in computational dynamic fracture-mechanics, JSME Int. J. A 37 (1994) 313–333.
[86] P.E. Odonoghue, M.F. Kanninen, S.T. Green, J.W. Cardinal, C.P. Leung, R.M. Curr, Fracture-mechanics computational analysis of crack-propagation in pressurized pipelines using a coupled fluid structure model, Numer. Methods Eng. Theory Appl. 1 (1990) 28–37.
[87] N. Moes, J. Dolbow, T. Belytschko, A finite element method for crack growth without remeshing, Internat. J. Numer. Methods Engrg. 46 (1999) 131–150.
[88] J.M. Melenk, I. Babuska, The partition of unity finite element method: Basic theory and applications, Comput. Methods Appl. Math. 139 (1996) 289–314.
[89] I. Babuska, J.M. Melenk, The partition of unity method, Internat. J. Numer. Methods Engrg. 40 (1997) 727–758.
[90] M.S. Shephard, N.A.B. Yehia, G.S. Burd, T.J. Weidner, Automatic crack-propagation tracking, Comput. Struct. 20 (1985) 211–223.
[91] P.A. Wawrzynek, A.R. Ingraffea, Interactive finite-element analysis of fracture processes - an integrated approach, Theor. Appl. Fract. Mech. 8 (1987) 137–150.
[92] G.T. Camacho, M. Ortiz, Computational modelling of impact damage in brittle materials, Int. J. Solids Struct. 33 (1996) 2899–2938.
[93] P.D. Zavattieri, Modeling of crack propagation in thin-walled structures using a cohesive model for shell elements, Trans. ASME, J. Appl. Mech. 73 (2006) 948–958.
[94] M.G.A. Tijssens, B.L.J. Sluys, E. van der Giessen, Numerical simulation of quasi-brittle fracture using damaging cohesive surfaces, Eur. J. Mech. A Solids 19 (2000) 761–779.
[95] J.J.S. Biswakarma, D.A. Cruz, E.D. Bain, J.M. Dennis, J.W. Andzelm, S.R. Lustig, Modeling brittle fractures in epoxy nanocomposites using extended finite element and cohesive zone surface methods, Polymers 13 (2021).
[96] A. Ibrahimbegovic, S. Melnyk, Embedded discontinuity finite element method for modeling of localized failure in heterogeneous materials with structured mesh: an alternative to extended finite element method, Comput. Mech. 40 (2007) 149–155.
[97] C. Lo, C.M. Hsieh, D.L. Young, An embedding finite element method for viscous incompressible flows with complex immersed boundaries on Cartesian grids, Eng. Comput. 31 (2014) 656–680.
[98] H. Rajiyah, S.N. Atluri, Analysis of embedded and surface elliptic flaws in transversely isotropic bodies by the finite-element alternating method, Trans. ASME, J. Appl. Mech. 58 (1991) 435–443.

[99] E. Benvenuti, A regularized XFEM framework for embedded cohesive interfaces, Comput. Methods Appl. Math. 197 (2008) 4367–4378.
[100] S.P.A. Bordas, T. Rabczuk, H. Nguyen-Xuan, V.P. Nguyen, S. Natarajan, T. Bog, M.Q. Do, V.H. Nguyen, Strain smoothing in FEM and XFEM, Comput. Struct. 88 (2010) 1419–1443.
[101] E. Bechet, H. Minnebol, N. Moes, B. Burgardt, Improved implementation and robustness study of the X-FEM for stress analysis around cracks, Internat. J. Numer. Methods Engrg. 64 (2005) 1033–1056.
[102] D.J. Holdych, D.R. Noble, R.B. Secor, Quadrature rules for triangular and tetrahedral elements with generalized functions, Internat. J. Numer. Methods Engrg. 73 (2008) 1310–1327.
[103] J.Y. Wu, F.B. Li, An improved stable XFEM (Is-XFEM) with a novel enrichment function for the computational modeling of cohesive cracks, Comput. Methods Appl. Math. 295 (2015) 77–107.
[104] J.Y. Wu, F.B. Li, S.L. Xu, Extended embedded finite elements with continuous displacement jumps for the modeling of localized failure in solids, Comput. Methods Appl. Math. 285 (2015) 346–378.
[105] A.S. Vagbharathi, S. Gopalakrishnan, An extended finite-element model coupled with level set method for analysis of growth of corrosion pits in metallic structures, Proc. R. Soc. Lond. Ser. A Math. Phys. Eng. Sci. 470 (2014).
[106] G. Jovicic, M. Zivkovic, N. Jovicic, Numerical simulation of crack modeling using extended finite element method, Strojniski Vestnik-J. Mech. Eng. 55 (2009) 549–554.
[107] G. Meschke, P. Dumstorff, W. Fleming, Variational extended finite element model for cohesive cracks: Influence of integration and interface law, in: Iutam Symposium on Discretization Methods for Evolving Discontinuities, vol. 5, 2007, p. 283.
[108] N. Sukumar, N. Moes, B. Moran, T. Belytschko, Extended finite element method for three-dimensional crack modelling, Internat. J. Numer. Methods Engrg. 48 (2000) 1549–1570.
[109] Y.R. Rashid, Ultimate strength analysis of prestressed concrete pressure vessels, Nucl. Eng. Des. 7 (1968) 334.
[110] Z.P. Bazant, F.B. Lin, Nonlocal smeared cracking model for concrete fracture, ASCE J. Struct. Eng. 114 (1988) 2493–2510.
[111] R. Deborst, On the numerical instability of the smeared-crack approach in the non-linear modeling of concrete structures - discussion, Commun. Appl. Numer. Methods 5 (1989) 489–493.
[112] R.H. Graves, K.N. Derucher, Interface smeared crack model analysis of concrete dams in earthquakes, ASCE J. Eng. Mech. 113 (1987) 1678–1693.
[113] M. Cervera, M. Chiumenti, R. Codina, Mesh objective modeling of cracks using continuous linear strain and displacement interpolations, Internat. J. Numer. Methods Engrg. 87 (2011) 962–987.
[114] J.T. Wang, E.J. Pineda, V. Ranatunga, S.S. Smeltzer, 3D progressive damage modeling for laminated composite based on crack band theory and continuum damage mechanics, in: Proceedings of the American Society for Composites: Thirtieth Technical Conference, 2015, pp. 1750–1766.
[115] M. Alijani-Ardeshir, B.N. Neya, M. Ahmadi, Comparative study of various smeared crack models for concrete dams, Gradevinar 71 (2019) 305–318.
[116] D.J. Burnett, H.L. Schreyer, A mesh objective method for modeling crack propagation using the smeared crack approach, Internat. J. Numer. Methods Engrg. 117 (2019) 574–603.
[117] W. Xu, A.M. Waas, Modeling damage growth using the crack band model; effect of different strain measures, Eng. Fract. Mech. 152 (2016) 126–138.
[118] A.T. Dincel, S.D. Akbarov, Mathematical modelling and 3D FEM analysis of the influence of initial stresses on the ERR in a band crack's front in the rectangular orthotropic thick plate, CMC Comput. Mater. Continua 53 (2017) 249–270.
[119] S. Taira, K. Tanaka, Y. Nakai, Model of crack-tip slip band blocked by grain-boundary, Mech. Res. Commun. 5 (1978) 375–381.
[120] G. Pijaudiercabot, A. Huerta, L. Bode, Nonlocal continuum damage and adapted solution strategies in computational failure mechanics, New Adv. Comput. Struct. Mech. 32 (1992) 81–95.
[121] T. Svedberg, K. Runesson, An algorithm for gradient-regularized plasticity coupled to damage based on a dual mixed FE-formulation, Comput. Methods Appl. Math. 161 (1998) 49–65.
[122] Z.P. Bazant, M. Jirasek, Nonlocal integral formulations of plasticity and damage: Survey of progress, J. Eng. Mech. 128 (2002) 1119–1149.
[123] P.J. Bouchard, M.R. Goldthorpe, P. Prottey, J-integral and local damage fracture analyses for a pump casing containing large weld repairs, Int. J. Press. Vessels Pip. 78 (2001) 295–305.
[124] A. Simone, H. Askes, L.J. Sluys, Incorrect initiation and propagation of failure in non-local and gradient-enhanced media, Int. J. Solids Struct. 41 (2004) 351–363.
[125] M.G.D. Geers, R. de Borst, W.A.M. Brekelmans, R.H.J. Peerlings, Strain-based transient-gradient damage model for failure analyses, Comput. Methods Appl. Math. 160 (1998) 133–153.
[126] R.H.J. Peerlings, R. deBorst, W.A.M. Brekelmans, J.H.P. deVree, Gradient enhanced damage for quasi-brittle materials, Internat. J. Numer. Methods Engrg. 39 (1996) 3391–3403.
[127] Morro A., A phase-field approach to continuum damage mechanics, Materials 15 (2022).
[128] C. Kuhn, A. Schluter, R. Muller, On degradation functions in phase field fracture models, Comput. Mater. Sci. 108 (2015) 374–384.
[129] H. Amor, J.J. Marigo, C. Maurini, Regularized formulation of the variational brittle fracture with unilateral contact: Numerical experiments, J. Mech. Phys. Solids 57 (2009) 1209–1229.
[130] G.A. Francfort, J.J. Marigo, Revisiting brittle fracture as an energy minimization problem, J. Mech. Phys. Solids 46 (1998) 1319–1342.
[131] B. Bourdin, G.A. Francfort, J.J. Marigo, Numerical experiments in revisited brittle fracture, J. Mech. Phys. Solids 48 (2000) 797–826.
[132] M. Hofacker, C. Miehe, A phase field model of dynamic fracture: Robust field updates for the analysis of complex crack patterns, Internat. J. Numer. Methods Engrg. 93 (2013) 276–301.
[133] Y. Heider, A review on phase-field modeling of hydraulic fracturing, Eng. Fract. Mech. 253 (2021).

[134] I.S. Aranson, V.A. Kalatsky, V.M. Vinokur, Continuum field description of crack propagation, Phys. Rev. Lett. 85 (2000) 118–121.
[135] A. Karma, D.A. Kessler, H. Levine, Phase-field model of mode III dynamic fracture, Phys. Rev. Lett. 87 (2001).
[136] D.P. Landau, K. Binder, A Guide to Monte Carlo Simulations in Statistical Physics, fifth ed., Cambridge University Press, Cambridge, United Kingdom ; New York, NY, 2020.
[137] S. Santra, S. Mandal, S. Chakraborty, Phase-field modeling of multicomponent and multiphase flows in microfluidic systems: a review, Internat. J. Numer. Methods Heat Fluid Flow 31 (2021) 3089–3131.
[138] P. Diehl, R. Lipton, T. Wick, M. Tyagi, A comparative review of peridynamics and phase-field models for engineering fracture mechanics, Comput. Mech. 69 (2022) 1259–1293.
[139] M. Ambati, T. Gerasimov, L. De Lorenzis, A review on phase-field models of brittle fracture and a new fast hybrid formulation, Comput. Mech. 55 (2015) 383–405.
[140] J. Li, J.B. Chen, W.L. Sun, Y.B. Peng, Advances of the probability density evolution method for nonlinear stochastic systems, Probab. Eng. Mech. 28 (2012) 132–142.
[141] Y. Feng, W. Gao, D. Wu, F. Tin-Loi, Machine learning aided stochastic elastoplastic analysis, Comput. Methods Appl. Math. 357 (2019).
[142] K. Sett, B. Jeremic, M.L. Kavvas, Probabilistic elasto-plasticity: solution and verification in 1D, Acta Geotech. 2 (2007) 211–220.
[143] K.W. Liao, N.I.D. Biton, A heuristic moment-based framework for optimization design under uncertainty, Eng. Comput. 36 (2020) 1229–1242.
[144] G. Stefanou, M. Fragiadakis, Nonlinear dynamic analysis of frames with stochastic non-Gaussian material properties, Eng. Struct. 31 (2009) 1841–1850.
[145] H. Zhang, Durability reliability analysis for corroding concrete structures under uncertainty, Mech. Syst. Signal Process. 101 (2018) 26–37.
[146] J.B. Chen, J. Li, The extreme value distribution and dynamic reliability analysis of nonlinear structures with uncertain parameters, Struct. Saf. 29 (2007) 77–93.
[147] J.C. Helton, J.D. Johnson, W.L. Oberkampf, C.B. Storlie, A sampling-based computational strategy for the representation of epistemic uncertainty in model predictions with evidence theory, Comput. Methods Appl. Math. 196 (2007) 3980–3998.
[148] M.G. Stewart, J. Li, Risk-based assessment of blast-resistant design of ultra-high performance concrete columns, Struct. Saf. 88 (2021).
[149] M.G. Stewart, Simplified reliability-based load design factors for explosive blast loading, weapons effects, and its application to collateral damage estimation, J. Def. Model. Simul.-Ap 19 (2022) 385–401.
[150] M.G. Stewart, Spatial variability of pitting corrosion and its influence on structural fragility and reliability of RC beams in flexure, Struct. Saf. 26 (2004) 453–470.
[151] H.A. Moghaddam, P. Mertiny, Stochastic finite element analysis framework for modelling electrical properties of particle-modified polymer composites, Nanomaterials 10 (2020).
[152] M. Lacour, J. Macedo, N.A. Abrahamson, Stochastic finite element method for non-linear material models, Comput. Geotech. 125 (2020).
[153] M. Lacour, G. Bal, N. Abrahamson, Dynamic stochastic finite element method using time-dependent generalized polynomial chaos, Int. J. Numer. Anal. Methods Geomech. 45 (2021) 293–306.
[154] D.E.M. Bouhjiti, J. Baroth, F. Dufour, M. Briffaut, B. Masson, Probabilistic analysis of concrete cracking using stochastic finite element methods: application to nuclear containment buildings at early age, Mater. Struct. 53 (2020).
[155] F.J. Marin, J. Martinez-Frutos, F. Periago, A polynomial chaos-based approach to risk-averse piezoelectric control of random vibrations of beams, Internat. J. Numer. Methods Engrg. 115 (2018) 738–755.
[156] J.D. Jakeman, F. Franzelin, A. Narayan, M. Eldred, D. Plfuger, Polynomial chaos expansions for dependent random variables, Comput. Methods Appl. Math. 351 (2019) 643–666.
[157] A.E. Litvak, A. Lytova, K. Tikhomirov, N. Tomczak-Jaegermann, P. Youssef, Structure of eigenvectors of random regular digraphs, Trans. Amer. Math. Soc. 371 (2019) 8097–8172.
[158] C. Bordenave, A. Guionnet, Localization and delocalization of eigenvectors for heavy-tailed random matrices, Probab. Theory Related Fields 157 (2013) 885–953.
[159] H. Qin, M.G. Stewart, Casualty risks induced by primary fragmentation hazards from high-explosive munitions, Reliab. Eng. Syst. Safe 215 (2021).
[160] M.G. Stewart, A. Al-Harthy, Pitting corrosion and structural reliability of corroding RC structures: Experimental data and probabilistic analysis, Reliab. Eng. Syst. Safe 93 (2008) 373–382.
[161] M. Papadrakakis, G. Stefanou, Multiscale Modeling and Uncertainty Quantification of Materials and Structures : Proceedings of the IUTAM Symposium Held At Santorini, Greece, September 9–11, 2013, Springer International Publishing : Imprint: Springer, Cham, 2014, 1 online resource (IX, 306 pages 157 illustrations, 364 illustrations in color.
[162] R. Cools, D. Nuyens, Monte carlo and quasi-monte carlo methods : mcqmc, leuven, belgium, 2014, Springer Proceedings in Mathematics & Statistics, Springer International Publishing : Imprint: Springer, Cham, 2016, 1 online resource (XVIII, 622 pages 116 illustrations, 657 illustrations in color.
[163] R. Bhardwaj, P. Manchanda, A.H. Siddiqi, Mathematical models, methods and applications, in: Industrial and Applied Mathematics, Springer Singapore : Imprint: Springer, Singapore, 2015, 1 online resource (XIX, 298 pages 103 illustrations, 260 illustrations in color.
[164] A. Hussein, M. El-Tawil, W. El-Tahan, A.A. Mahmoud, Solution of randomly excited stochastic differential equations with stochastic operator using spectral stochastic finite element method (SSFEM), Struct. Eng. Mech. 28 (2008) 129–152.

[165] J. Baroth, L. Bode, P. Bressolette, M. Fogli, Numerical convergence of a spectral stochastic finite element method (SSFEM) in lognormal context, Appl. Stat. Probab. Civ. Eng. 1 and 2 (2003) 217–224.
[166] G. Stefanou, The stochastic finite element method: Past, present and future, Comput. Methods Appl. Math. 198 (2009) 1031–1051.
[167] F. Uribe, I. Papaioannou, W. Betz, D. Straub, Bayesian inference of random fields represented with the Karhunen–Loeve expansion, Comput. Methods Appl. Math. 358 (2020).
[168] G. Stefanou, M. Papadrakakis, Assessment of spectral representation and Karhunen–Loeve expansion methods for the simulation of Gaussian stochastic fields, Comput. Methods Appl. Math. 196 (2007) 2465–2477.
[169] Zemanek P., Eigenfunctions expansion for discrete symplectic systems with general linear dependence on spectral parameter, J. Math. Anal. Appl. 499 (2021).
[170] S.E. Pryse, S. Adhikari, Stochastic finite element response analysis using random eigenfunction expansion, Comput. Struct. 192 (2017) 1–15.
[171] S. Shahane, E. Guleryuz, D.W. Abueidda, A.L. Lee, J. Liu, X. Yu, R. Chiu, S. Koric, N.R. Aluru, P.M. Ferreira, Surrogate neural network model for sensitivity analysis and uncertainty quantification of the mechanical behavior in the optical lens-barrel assembly, Comput. Struct. 270 (2022).
[172] D.A. Cole, R.B. Gramacy, M. Ludkovski, Large-scale local surrogate modeling of stochastic simulation experiments, Comput. Statist. Data Anal. 174 (2022).
[173] F. Masood, U. Amin, M.A. Fiaz, M.A. Ashraf, On relating the perturbation theory and random cylinder generation to study scattered field, Phys. Commun. 39 (2020).
[174] A. Blumenthal, J.X. Xue, Y. Yang, Lyapunov exponents for random perturbations of coupled standard maps, Comm. Math. Phys. 389 (2022) 121–151.
[175] R.E. Melchers, A.T. Beck, Structural Reliability Analysis and Prediction, third ed., Wiley, Hoboken, NJ, 2018.
[176] C. Wang, W. Gao, C.M. Song, N. Zhang, Stochastic interval analysis of natural frequency and mode shape of structures with uncertainties, J. Sound Vib. 333 (2014) 2483–2503.
[177] C. Jiang, W.X. Li, X. Han, L.X. Liu, P.H. Le, Structural reliability analysis based on random distributions with interval parameters, Comput. Struct. 89 (2011) 2292–2302.
[178] B.Z. Xia, H. Lu, D.J. Yu, C. Jiang, Reliability-based design optimization of structural systems under hybrid probabilistic and interval model, Comput. Struct. 160 (2015) 126–134.
[179] J.W. Feng, D. Wu, W. Gao, G.Y. Li, Hybrid uncertain natural frequency analysis for structures with random and interval fields, Comput. Methods Appl. Math. 328 (2018) 365–389.
[180] A. Egger, U. Pillai, K. Agathos, E. Kakouris, E. Chatzi, I.A. Aschroft, S.P. Triantafyllou, Discrete and phase field methods for linear elastic fracture mechanics: A comparative study and state-of-the-art review, Appl. Sci.-Basel 9 (2019).
[181] H.D. Huynh, M.N. Nguyen, G. Cusatis, S. Tanaka, T.Q. Bui, A polygonal XFEM with new numerical integration for linear elastic fracture mechanics, Eng. Fract. Mech. 213 (2019) 241–263.
[182] H. Dirik, T. Yalcinkaya, Crack path and life prediction under mixed mode cyclic variable amplitude loading through XFEM, Int. J. Fatigue 114 (2018) 34–50.
[183] W.T. Ma, G.J. Liu, W.S. Wang, A coupled extended meshfree-smoothed meshfree method for crack growth simulation, Theor. Appl. Fract. Mech. 107 (2020).
[184] T.N. Bittencourt, P.A. Wawrzynek, A.R. Ingraffea, J.L. Sousa, Quasi-automatic simulation of crack propagation for 2D LEFM problems, Eng. Fract. Mech. 55 (1996) 321–334.
[185] X.F. Wang, Z.J. Yang, A.P. Jivkov, Monte Carlo simulations of mesoscale fracture of concrete with random aggregates and pores: a size effect study, Constr. Build. Mater. 80 (2015) 262–272.
[186] Y.J. Huang, D.M. Yan, Z.J. Yang, G.H. Liu, 2D and 3D homogenization and fracture analysis of concrete based on in-situ X-ray computed tomography images and Monte Carlo simulations, Eng. Fract. Mech. 163 (2016) 37–54.
[187] L.E. Garciano, I. Yoshida, Reliability analysis of a brittle fracture due to crack instability using sequential Monte Carlo simulation, Appl. Stat. Probab. Civ. Eng. (2011) 2949–2956.
[188] M.S. Chowdhury, C.M. Song, W. Gao, Probabilistic fracture mechanics by using Monte Carlo simulation and the scaled boundary finite element method, Eng. Fract. Mech. 78 (2011) 2369–2389.
[189] M. Georgioudakis, G. Stefanou, M. Papadrakakis, Stochastic failure analysis of structures with softening materials, Eng. Struct. 61 (2014) 13–21.
[190] I. Papaioannou, D. Straub, Combination line sampling for structural reliability analysis, Struct. Saf. 88 (2021).
[191] A. Tabandeh, G.F. Jia, P. Gardoni, A review and assessment of importance sampling methods for reliability analysis, Struct. Saf. 97 (2022).
[192] W.T. Riddell, Probabilistic growth of complex fatigue crack shapes: Toward risk based inspection intervals for railroad tank cars, J. Mech. Des. 123 (2001) 622–629.
[193] H. Kagawa, A. Morita, T. Matsuda, S. Kubo, Fatigue crack propagation behavior in four-points bending specimens with multiple parallel edge notches at regular intervals, Eng. Fract. Mech. 75 (2008) 4594–4609.
[194] Q. Dai, C.Y. Zhou, J. Peng, X.W. Chen, X.H. He, Non-probabilistic defect assessment for structures with cracks based on interval model, Nucl. Eng. Des. 262 (2013) 235–245.
[195] M.S. Chowdhury, C.M. Song, W. Gao, C. Wang, Reliability analysis of homogeneous and bimaterial cracked structures by the scaled boundary finite element method and a hybrid random-interval model, Struct. Saf. 59 (2016) 53–66.
[196] C. Jiang, X.Y. Long, X. Han, Y.R. Tao, J. Liu, Probability-interval hybrid reliability analysis for cracked structures existing epistemic uncertainty, Eng. Fract. Mech. 112 (2013) 148–164.

[197] Y.G. Yu, W. Gao, A. Castel, A.R. Liu, Y. Feng, X.J. Chen, A. Mukherjee, Modelling steel corrosion under concrete non-uniformity and structural defects, Cem. Concr. Res. 135 (2020).
[198] Y.G. Yu, W. Gao, Y. Feng, A. Castel, X.J. Chen, A.R. Liu, On the competitive antagonism effect in combined chloride-sulfate attack: A numerical exploration, Cem. Concr. Res. 144 (2021).
[199] Y.J. Huang, H. Zhang, B.B. Li, Z.J. Yang, J.Y. Wu, P.J. Withers, Generation of high-fidelity random fields from micro CT images and phase field-based mesoscale fracture modelling of concrete, Eng. Fract. Mech. 249 (2021).
[200] J. Elias, M. Vorechovsky, Stochastic fracture simulations of concrete beams with shallow notches, Key Eng. Mater. 592–593 (2014) 229–232.
[201] J. Elias, M. Vorechovsky, Fracture in random quasibrittle media: I. Discrete mesoscale simulations of load capacity and fracture process zone, Eng. Fract. Mech. 235 (2020).
[202] T. Heister, M.F. Wheeler, T. Wick, A primal–dual active set method and predictor–corrector mesh adaptivity for computing fracture propagation using a phase-field approach, Comput. Methods Appl. Math. 290 (2015) 466–495.
[203] Hirshikesh C. Jansari, K. Kannan, R.K. Annabattula, S. Natarajan, Adaptive phase field method for quasi-static brittle fracture using a recovery based error indicator and quadtree decomposition, Eng. Fract. Mech. 220 (2019).
[204] D.J.J. Toal, N.W. Bressloff, A.J. Keane, C.M.E. Holden, The development of a hybridized particle swarm for kriging hyperparameter tuning, Eng. Optim. 43 (2011) 675–699.
[205] M.A. Bouhlel, N. Bartoli, A. Otsmane, J. Morlier, An improved approach for estimating the hyperparameters of the kriging model for high-dimensional problems through the partial least squares method, Math. Probl. Eng. 2016 (2016).
[206] J.J. Warnes, A sensitivity analysis for universal kriging, Math. Geol. 18 (1986) 653–676.
[207] R.A. Olea, Optimal contour mapping using universal kriging - reply, J. Geophys. Res. 80 (1975) 835–836.
[208] M. Dunbar, J.M. Murray, L.A. Cysique, B.J. Brew, V. Jeyakumar, Simultaneous classification and feature selection via convex quadratic programming with application to HIV-associated neurocognitive disorder assessment, European J. Oper. Res. 206 (2010) 470–478.
[209] L. Wang, J. Zhu, H. Zou, The doubly regularized support vector machine, Statist. Sinica 16 (2006) 589–615.
[210] A.J. Smola, B. Scholkopf, A tutorial on support vector regression, Stat. Comput. 14 (2004) 199–222.
[211] V. Vapnik, R. Izmailov, Rethinking statistical learning theory: learning using statistical invariants, Mach. Learn. 108 (2019) 381–423.
[212] J.W. Feng, L. Liu, D. Wu, G.Y. Li, M. Beer, W. Gao, Dynamic reliability analysis using the extended support vector regression (X-SVR), Mech. Syst. Signal Process. 126 (2019) 368–391.
[213] Y. Feng, D. Wu, L. Liu, W. Gao, F. Tin-Loi, Safety assessment for functionally graded structures with material nonlinearity, Struct Saf. 86 (2020).
[214] S. Joe, F.Y. Kuo, Constructing Sobol' sequences with better two-dimensional projections, SIAM J. Sci. Comput. 30 (2008) 2635–2654.
[215] T. Homma, A. Saltelli, Use of Sobol's quasirandom sequence generator for integration of modified uncertainty importance measure, J. Nucl. Sci. Technol. 32 (1995) 1164–1173.
[216] Q.H. Wang, Y. Feng, D. Wu, C.W. Yang, Y.G. Yu, G.Y. Li, M. Beer, W. Gao, Polyphase uncertainty analysis through virtual modelling technique, Mech. Syst. Signal Process. 162 (2022).
[217] M. Neuner, S. Smaniotto, G. Hofstetter, A modified wedge splitting test for susceptible quasi-brittle materials, Constr. Build. Mater. 326 (2022).
[218] E. Bruhwiler, F.H. Wittmann, The wedge splitting test, a new method of performing stable fracture-mechanics tests, Eng. Fract. Mech. 35 (1990) 117–125.
[219] J.Y. Wu, J.F. Qiu, V.P. Nguyen, T.K. Mandal, L.J. Zhuang, Computational modeling of localized failure in solids: XFEM vs PF-CZM, Comput. Methods Appl. Math. 345 (2019) 618–643.
[220] T. Ni, M. Zaccariotto, Q.Z. Zhu, U. Galvanetto, Coupling of FEM and ordinary state-based peridynamics for brittle failure analysis in 3D, Mech. Adv. Mater. Struct. 28 (2021) 875–890.
[221] X.Y. Long, C. Jiang, K. Liu, X. Han, W. Gao, B.C. Li, An interval analysis method for fatigue crack growth life prediction with uncertainty, Comput. Struct. 210 (2018) 1–11.
[222] C.X. Chen, S.J.L. Wong, S. Raghavan, H. Li, Design of experiments informed deep learning for modeling of directed energy deposition process with a small-size experimental dataset, Mater. Des. 222 (2022).
[223] DeBorst R., Computational modelling of concrete fracture, Adv. Fract. Res. 1–6 (1997) 1767–1778.
[224] Q.H. Wang, Y. Feng, D. Wu, G.Y. Li, Z.Y. Liu, W. Gao, Polymorphic uncertainty quantification for engineering structures via a hyperplane modelling technique, Comput. Methods Appl. Math. 398 (2022).
[225] Y. Tian, Q. Li, Y. Feng, Y. Yu, D. Wu, X. Chen, W. Gao, Nonlinear dynamic analysis of the functionally graded graphene platelets reinforced porous plate under moving mass, Thin Wall Struct. 183 (2023).
[226] Y. Liu, Y. Feng, D. Wu, X. Chen, W. Gao, Virtual modelling integrated phase field method for dynamic fracture analysis, Int. J. Mech. Sci. 252 (2023).